Planetary Radio Interferometry and Doppler Experiment (PRIDE) for radio occultation studies

A Venus Express test case

Bocanegra Bahamon, Tatiana

DOI
10.4233/uuid:738b9b01-d130-4ae4-bc51-c989824a8760

Publication date
2019

Document Version
Final published version

Citation (APA)
Bocanegra Bahamon, T. (2019). *Planetary Radio Interferometry and Doppler Experiment (PRIDE) for radio occultation studies: A Venus Express test case*. [Dissertation (TU Delft), Delft University of Technology]. https://doi.org/10.4233/uuid:738b9b01-d130-4ae4-bc51-c989824a8760

Planetary Radio Interferometry and Doppler Experiment (PRIDE) for radio occultation studies

A Venus Express test case

Planetary Radio Interferometry and Doppler Experiment (PRIDE) for radio occultation studies

A Venus Express test case

Proefschrift

ter verkrijging van de graad van doctor
aan de Technische Universiteit Delft,
op gezag van de Rector Magnificus Prof.Dr.Ir. T.H.J.J. van der Hagen,
voorzitter van het College voor Promoties,
in het openbaar te verdedigen op

dinsdag 19 maart 2019 om 10:00 uur

door

Tatiana Marcela BOCANEGRA BAHAMÓN

Ingenieur Luchtvaart en Ruimtevaart,
Technische Universiteit Delft, Nederland,
geboren te Bogotá, Colombia

This dissertation has been approved by the:

promotor: Prof.Dr. L.L.A. Vermeersen
promotor: Prof.Dr. L.I. Gurvits

Composition of the doctoral committee:

Rector Magnificus	chairperson
Prof.Dr. L.L.A. Vermeersen	Technische Universiteit Delft
Prof.Dr. L.I. Gurvits	Joint Institute for VLBI ERIC (JIVE) and Technische Universiteit Delft
Independent members:	
Prof.Dr. C. Jackson	ASTRON
Prof.Dr. V. Dehant	Royal Observatory of Belgium
Prof.Dr.-Ing.Habil. R. Klees	Technische Universiteit Delft
Dr. D.V. Titov	ESA-ESTEC
Dr.Ir. D. Dirkx	Technische Universiteit Delft
Prof.Dr.Ir. P.N.A.M. Visser	Technische Universiteit Delft (reserve member)

The work presented in this dissertation was performed with support from the NWO (GBE) project 614.011.501 on Dutch-Chinese cooperation in Very Long Baseline Interferometry, implemented by the Joint Institute for VLBI European Research Infrastructure Consortium and Shanghai Astronomical Observatory of the Chinese Academy of Sciences.

Keywords: Doppler and VLBI spacecraft tracking, planetary missions, radio science applications, radio occultation, planetary atmospheres.

Printed by: Ridderprint.

Front & Back: Schematic representation of a radio occultation experiment with Venus Express orbiter conducted with radio telescopes on Earth. Image copyright: ESA (Venus Express), JAXA/ISAS/DARTS/Damia Bouic (Venus) and Harm-Jan Stiepel/ASTRON (Westerbork).

ISBN 978-94-6375-341-8

An electronic version of this dissertation is available at
http://repository.tudelft.nl/

Contents

Preface

The thesis that you are about to read deals with the implementation of a technique to study atmospheres of planets or moons in the Solar System. We use radio telescopes on Earth to track spacecraft that are orbiting planets, and use the signal the spacecraft emits, as it crosses the planet's atmosphere, to investigate its physical characteristics. Amazing, isn't it? Often, we get lost in our daily routines and we lose sight of the overall picture. We forget how truly astounding the experiments we are able to undertake are, using the universe as our lab. I feel very privileged to have been able to do this as part of the work that led to this dissertation.

Looking back to my personal journey and to how it all started, I think of Ellie. Yes, I'm a kid of the 90s (85 rounds off to 90) influenced by American pop culture, and yes, I'm one of those who became obsessed with space because of the movie Contact. That, the series from the Earth to the Moon and a visit to the Kennedy Space Center sparked my interest. All of this was years before my first physics class, but already then it was clear to me that I wanted to pursue a career in space exploration. There are many wonderful people that helped me along in the process of moving from dreaming about space to being able to perform experiments with planetary spacecraft. First and foremost, I would like to thank my mentor and PhD supervisor Leonid Gurvits, the person who introduced me to this amazing field and the person who has constantly given me the opportunity, from my bachelor's through to my PhD, to join multiple projects and broaden my research experience. Thank you very much for your guidance and support. I would also like to thank Bert Vermeersen, my master's thesis supervisor and PhD promotor, for giving me the freedom and support to find a research topic to my interest, and for providing guidance throughout this process.

Over these years it has been a pleasure to be able to work in different environments, various countries, and among very intelligent and inspiring people. To my colleagues and friends from the group of Astrodynamics and Space Missions in the faculty of Aerospace Engineering at TUDelft, Boudewijn, Ejo (also my bachelor's supervisor), Erwin, Ron, Marc, José, Eelco, Wim, Daphne, Kevin, Imke, Wouter, Loïc, Vidhya, Stephanie, Elisabetta, many thanks for the lively and stimulating working

atmosphere. Special thanks to Relly for all the support and for ensuring everything runs smoothly in our department. To Pieter, for his support and very valuable input when reviewing my thesis. To Dominic, my friend, colleague and collaborator, I've always valued your opinion about my work very much, I have learnt a great deal from you. To Joao, for all the good advice and saving my thesis with Zambujeira. To my fellow PhD colleagues and friends, Bart, Hermes, Kartik, Guido, Mao, Black, Bas, Haiyang, Teresa, Günther, Jacco, Svenja, Tim, Gourav, Yuxin, for all the fun times inside and outside work. Certainly, we have a wide spectrum of unique and extraordinary characters among us. To Jinglang, my office-mate and dear friend, for all the great times we had together. To my second home institute JIVE and all the colleagues I had the pleasure to spend time with over the past years. Special thanks to Giuseppe, Guifré, Dima, Sergei and Dora, the Space Science and Innovative Applications Group at JIVE, for giving me a fascinating first-hand experience with all the tracking experiments we conducted, all the knowledge you passed on to me and for your invaluable friendship. To the JIVE support scientists, Benito, Katharina, Jay and Ross for their friendship and for being supportive in a much broader sense. To Huib and Paco for always welcoming me to the institute, and to Yvonne for being always ready to help. I would also like to thank my colleagues at Shanghai Astronomical Observatory for the great collaborations we have had between our institutes over the past years. Special thanks to Prof. Hong Xiaoyu, Ma Maoli and Wu Fang for welcoming me to their institute every year during my PhD. To the EVN community and the telescopes' operators for allowing us to conduct these 'out of the ordinary' experiments. To Prof.Dr. Carole Jackson, Prof.Dr. Veronique Dehant, Dr. Dmitri Titov and Prof.Dr.-Ing.Habil. Roland Klees for accepting the invitation to take part in the doctoral committee of my PhD defense.

To the people who have had in one way or another a great influence in my life. To my childhood friends Claudia, Paula R., Juliana, Maria, Paula M., Mariana and María José. To Guille and Nicolás. To Matías, Bola, Rigo and the very intense semester capando clase en el Bicafé. To my LR friends Bart, Alex, Jonas, Greg, Lore and Cassandra. To my housemates in DS4 and to the Bagijners. To Ana and Angela. To Gaëllita, Lina and Ana. To my latest discoveries, Marloes and Kat, to Lexie and the imaginary bricks. To my Colombian-Delfians Andrés, Simon, Nuci, Santiago, Alejandra, Damián, Christian, Carolina, Nataly, Miguel and Mari. To my Spanish-Delfians. To Fle and Miren. To 'mijn kinderen' Alejo, Mike, Tom, Maarten, Peter, Miquel and Roderick, for absolutely everything they have done for me, especially these last difficult years. To Els and John, for all the support and for welcoming me into their home and family. To Dirk, for all the years of unconditional support and love. I wouldn't have been able to finish this thesis without you.

To my family, ¡qué gran familia la que tenemos!. To my grandparents Roberto, Inés, Gonzalo and Elsa, my aunts and uncles, and all my cousins, for all the family trips, reunions and parties. Being able to grow in such a vibrant and loving environment has definitely had a very positive impact in my life. Special thanks to uncle Piti and tía Pocho for all those amazing vacations in Ibagué. To el Pollo, my twin and soulmate, for our uncanny long distance connection. To my quasi-siblings Daniel, Carolina, Julián, Mark and Michael, for all the experiences we've shared and for taking care of my parents. To Camilo and Lena, for their amazing friendship. To Esteban and Martín, for all the happiness they bring into my life. To Angela and Diego, for

being truly excellent people, for inspiring me and for always having my back. A Luchito y Nechi, por su inmensa dedicación como padres, por la gran confianza y el gran amor que siempre me han dado. Todo se los debo a ustedes.

Tatiana Marcela BOCANEGRA BAHAMÓN
Amsterdam, February 2019

Summary

Electromagnetic emission is an indispensable means of communication with interplanetary spacecraft in their journeys through the Solar System. The transmission and reception of radio signals to and from interplanetary spacecraft have three main functions. The first is the generation of radiometric data (*e.g.*, Doppler, ranging and interferometric data) to enable the precise determination of the spacecraft's state vector (*i.e.*, position and velocity) along its trajectory. The second is for telecommunication purposes, sending commands to the spacecraft on the uplink and transmitting telemetry (*i.e.* engineering and science data produced by the instruments onboard the spacecraft) on the downlink. The third function is to conduct scientific research by analyzing the different effects that the presence of the planetary bodies and interplanetary medium has on the spacecraft signal, as it propagates back to the Earth. This functionality is usually referred to as the mission's radio science experiment.

The two first functions are vital for the mission, while the third is not necessarily. For this reason, the former two are the main priorities of the deep space networks: to support navigation and to control and monitor the status of the spacecraft [13]. The third function is generally implemented using the deep space network facilities as an Earth-based segment of radio science instrumentation. In this thesis, an additional option to using the deep space networks for this function - radio science experiments - is presented: the Planetary Radio Interferometry and Doppler Experiment (PRIDE), focusing primarily on one application, radio occultation studies.

The PRIDE technique is an experimental setup that makes use of the onboard spacecraft transmitter or transponder and Earth-based radio telescope networks, in order to provide (1) radial velocity and (2) angular position measurements, to support radio science experiments [3–5, 12]. This is done by performing precise Doppler tracking of the spacecraft carrier signal with multiple radio telescopes on Earth. A wideband spectral analysis is conducted to extract the topocentric Doppler shift of the carrier signal, due to the relative motion of the transmitter and receiver, at each station. Subsequently, these signals are cross-correlated using the near-field Very Long Baseline Interferometry (VLBI) technique in phase-referencing mode. This modifica-

tion of the traditional VLBI technique requires a special near-field VLBI delay model. The objective of the near-field VLBI model is to calculate the a priori difference in the arrival time of the curved wave front of the signal, at every two stations of the observing array, in order to achieve a coherent response (the so-called 'interferometric fringes') by cross-correlating the signals. This is actually the fundamental principle behind radio interferometry [16], but taking into account that the source of the radio signal (*i.e.* the spacecraft) is at a finite distance from the receivers. In the case of VLBI, the telescopes are located at very long distances from each other, and therefore, independent timing (local oscillators) and signal recording systems are required. With the information from the near-field modeled delays and the phase and frequency of the resulting interference fringe pattern, the angular position of the radio source can be determined. The latter is achieved in the so-called phase-referencing mode [1, 16]. In this mode, other radio sources that are angularly close-by to the target source ($\lesssim 2$ deg) are used to calibrate the phase of the spacecraft signal. The calibrator sources are typically chosen to be natural radio sources located at billions of light-years away from the Earth whose absolute celestial positions are known very accurately (at the level of tens of μas). This summarizes briefly the methodology used by PRIDE to derive the angular position and radial velocity of the target spacecraft, the latter resulting as a by-product of the VLBI technology.

In order to benchmark the technique with respect to the use of the traditional deep space networks for radio science investigations, a noise budget of the Doppler detections obtained with the PRIDE is presented in this thesis [3]. As a test case, a tracking experiment of the European Space Agency (ESA) Mars Express (MEX) was used, during which the spacecraft performed a Phobos' fly-by in December 2013. In this experiment, 31 VLBI radio telescopes around the world participated for a total of 26 hours of continued tracking of MEX. In order to determine the quality of the PRIDE Doppler detections, the random errors introduced by the instrumentation and by the propagation of the signal through the interplanetary media were analyzed. This analysis quantified the contribution of the different noise sources to the total Doppler residuals. This information was used to provide a noise budget of the observations. It was demonstrated that the residual frequencies obtained with PRIDE Doppler detections are at the same noise levels as those of standard Doppler detections obtained with NASA's and ESA's deep space network antennas ($\sim$2 mHz, which is equivalent to a linear measure of $\sim 35\mu$m/s for three-way Doppler at X-band).

Having validated the methodology used in PRIDE, its applicability and performance for conducting planetary atmospheric studies was investigated by means of radio occultation experiments [2]. When a spacecraft is orbiting a planet the signal of the spacecraft can get occulted by the celestial body as seen from the ground stations on Earth. If the planet has an atmosphere, before the signal gets completely occulted it will get refracted through the planet's atmosphere, and the resulting frequency changes in the carrier signal will be detected by the receiving ground stations. By performing spectral analysis of the received signal and with precise information of the position and velocity of the spacecraft, the physical properties of the section of the atmosphere which the spacecraft signal has sounded can be derived [*e.g.* 6, 8–11, 14, 17].

In the work at hand, this particular application of PRIDE has been assessed by observing ESA's Venus Express (VEX) during multiple Venus occultation events [2].

From these observing sessions density, temperature and pressure profiles of the neutral atmosphere of Venus have been derived. With this VEX test case, it has been demonstrated that the PRIDE setup and processing pipeline is very well suited for radio occultation experiments of planetary bodies. The noise budget of the observations obtained with the VLBI stations indicated that the uncertainties in the Doppler detections are in the same order of magnitude as those obtained with NASA's Deep Space Network (DSN) and ESA's ESA Tracking Network (Estrack). For instance, uncertainties in the order of 2 mHz in the Doppler residuals result in uncertainties of $\sim$0.01 K in the temperature profiles of Venus' neutral atmosphere. These results correspond to those reported in previous Venus radio occultation experiments involving DSN stations (*e.g.*, Tellmann et al. [15]). We have also demonstrated that with PRIDE, making use of open-loop Doppler data, VLBI stations were able to sound deeper layers of Venus' thick atmosphere when compared to the closed-loop Doppler data provided by Estrack's New Norcia. With the wideband spectral analysis of PRIDE, we showed that even with small dish antennas, such as the 12-m AuScope's Katherine (Australia Northern Territory), the spacecraft signal can be detected below Venus' clouds layer.

Radio occultation experiments carried out with PRIDE can exploit the advantage of having access to large radio telescopes from the global VLBI networks, such as the 65-m Tianma (China), 100-m Effelsberg (Germany) or the 305-m Arecibo (Puerto Rico). Additionally, due to the wide coverage of the networks, the setup can be optimized to ensure high signal-to-noise (SNR) detections. Since their conception, the hardware and data acquisition software of the DSN and VLBI networks have been developed in close collaboration, and hence their performance is expected to be similar. However, there is a larger number of VLBI radio telescopes than deep space antennas distributed around the world. This allows us to choose those telescopes for which the observing conditions are the best (*i.e.*, highest elevation), while the deep space facilities are limited in this type of operational optimization. The combination of high sensitivity telescopes and wide coverage offers a great opportunity, especially when conducting radio occultation experiments of planets or moons with thick atmospheres, characterized by low SNR signal detections.

Based on the results presented in this thesis, it was demonstrated that the spectral analysis used in PRIDE allows the derivation of Doppler observables with very high spectral resolution. Additionally, it provides precise Doppler phase corrections essential to the correct correlation of the spacecraft signal, enabling the precise derivation of angular position corrections to the a priori spacecraft orbit. By demonstrating the performance of PRIDE and providing a noise budget to its Doppler detections, it is shown that the PRIDE technique qualifies as a fully operational radio science instrument. In particular, with the VEX radio occultation test case, it was demonstrated that the PRIDE methodology is suitable for experiments that require a careful detection of highly dynamic signals. It can be concluded that PRIDE, using a wide range of radio telescopes around the world, presents an alternative to using the customary deep space networks for radio science investigations. In particular, when the requests to support multiple deep space missions have conflicting schedules for the nominal agencies' tracking assets, or complementing each other, by enhancing the science return of tracking passes that are not nominally designed for radio science experiments.

PRIDE is one of the eleven experiments selected by ESA for its L-class JUpiter ICy moons Explorer mission (JUICE) mission, to be launched in 2022 [7]. The work presented in this thesis will be used to plan and optimize the setup of PRIDE to conduct radio occultation experiments to study Jupiter's atmosphere. Additionally, PRIDE is involved in the ESA EnVision M5 design study for an orbiter mission to Venus [18]. The main objective of PRIDE will be to conduct the radio occultation experiments to sound Venus' neutral atmosphere and ionosphere. In its current status the PRIDE technique, through the data processing and analysis methodology developed for this thesis, is in the capacity of conducting radio occultation experiments with virtually any planetary spacecraft.

The personal contribution of the defendant is:

- Development of a detailed noise model for the PRIDE open-loop Doppler observables.
- Tests and improvements to the existing wideband spectral analysis methodology of PRIDE experiments for observations with low Signal-to-Noise Ratio (SNR) detections and high signal dynamics, as it is typically the case of the radio occultation observation.
- Development of an ad-hoc software to process radio occultation observations obtained with radio telescopes with VLBI data acquisition systems, using as input the signal detections at the multiple VLBI stations to derive frequency residuals. This is performed by deriving open-loop Doppler observables from the received signals, and differencing them by a Doppler prediction calculated from the a priori orbit estimates. Subsequently, from geometric optics the ray path parameters of the propagation of the signal are derived from the Doppler residuals. The link between the ray path parameters and the physical properties of the section of the atmosphere being sounded is carried out implementing the so-called inverse model, using an Abel inverse transform. The software has been validated with NASA's Magellan data and ESA's VEX data. For this reason, the software can process radio occultation observation of different data formats. In its current status, the software is able to process radio occultation observations, assuming for the data reduction a spherically symmetric atmosphere and a constant composition of the neutral atmosphere.
- Development of an error propagation module that finds the noise of the Doppler residuals, derived from the input of the Doppler detections and Doppler predictions. Subsequently, it propagates these frequency residual uncertainties through the multiple steps of the data processing pipeline, to derive the uncertainties corresponding to the resulting refractivity, density, temperature and pressure profiles.

The novel results presented in this thesis are:

- Characterization of the performance of PRIDE providing an error budget of the open-loop Doppler observables. The uncertainties obtained with our measurements were compared with those obtained with ESA's Estrack New Norcia station and DSN's Robledo and Goldstone, during the same observing session of ESA's MEX spacecraft, showing consistent results.

- The results of the first radio occultation experiments conducted with PRIDE, using a test case ESA's VEX spacecraft. With these experiments the potential of the PRIDE technique for atmospheric studies via radio occultation observations was proven. The derived atmospheric profiles and their corresponding error propagation analysis showed the high level of consistency with the results of previous Venus' radio occultation experiments.

All results are published in refereed journals and presented in several international conferences with the leading participation of the defendant.

References

[1] Beasley, A. & Conway, J. 1995, in Very Long Baseline Interferometry and the VLBA, Vol. 82, 327

[2] Bocanegra-Bahamon, T., Molera-Calvès, G., Gurvits, L., et al. 2018, Accepted to Astronomy and Astrophysics

[3] Bocanegra-Bahamón, T., Molera-Calvés, G., Gurvits, L., et al. 2018, Astronomy & Astrophysics, 609, A59

[4] Duev, D. A., Calvés, G. M., Pogrebenko, S. V., et al. 2012, Astronomy & Astrophysics, 541, A43

[5] Duev, D. A., Pogrebenko, S. V., Cimò, G., et al. 2016, Astronomy & Astrophysics, 593, A34

[6] Eshleman, VR and Tyler, GL and Anderson, JD and Fjeldbo, G and Levy, GS and Wood, GE and Croft, TA. 1977, Space Science Reviews, 21, 207

[7] Grasset, O., Dougherty, M., Coustenis, A., et al. 2013, Planetary and Space Science, 78, 1

[8] Häusler, B., Pätzold, M., Tyler, G., et al. 2007, ESA SP, 1295, 1

[9] Howard, H., Eshleman, V., Hinson, D., et al. 1992, in The Galileo Mission (Springer), 565–590

[10] Kliore, AJ and Anderson, JD and Armstrong, JW and Asmar, SW and Hamilton, CL and Rappaport, NJ and Wahlquist, HD and Ambrosini, R and Flasar, FM and French, RG and others. 2004, in The Cassini-Huygens Mission (Springer), 1–70

[11] Michael Jr, WH and Tolson, RH and Brenkle, JP and Cain, DL and Fjeldbo, G and Stelzried, CT and Grossi, MD and Shapiro, II and Tyler, GL. 1977, Journal of Geophysical Research, 82, 4293

[12] Molera-Calvés, G., Pogrebenko, S., Cimò, G., et al. 2014, Astronomy & Astrophysics, 564, A4

[13] Mudgway, D. J. & Launius, R. 2001, Uplink-Downlink: A History of the Deep Space Network, 1957-1997

[14] Pätzold, M., Neubauer, F., Carone, L., et al. 2004, in Mars Express: The Scientific Payload, Vol. 1240, 141–163

[15] Tellmann, S., Pätzold, M., Häusler, B., Bird, M. K., & Tyler, G. L. 2009, Journal of Geophysical Research: Planets, 114

[16] Thompson, A. R., Moran, J. M., & Swenson Jr, G. W. 2008, Interferometry and synthesis in radio astronomy (John Wiley & Sons)

[17] Tommei, Giacomo and Dimare, Linda and Serra, Daniele and Milani, Andrea. 2014, Monthly Notices of the Royal Astronomical Society, 446, 3089

[18] Widemann, T., Wilson, C., Ghail, R., et al. 2018, in 42nd COSPAR Scientific Assembly, Vol. 42

Samenvatting

Elektromagnetische straling is een onmisbaar communicatiemedium voor interplanetaire ruimtevaartuigen tijdens hun reis door het Zonnestelsel. Het uitzenden en ontvangen van radiosignalen van en naar interplanetaire ruimtevaartuigen dient drie hoofdfuncties. De eerste is het genereren van radiometrische gegevens (bijvoorbeeld Doppler metingen, afstandsbepaling en interferometrische gegevens) om de voertuigtoestand (dat wil zeggen de positie en snelheid) in zijn baan precies te kunnen bepalen. De tweede is telecommunicatie, oftewel het omhoog sturen van commando's naar het ruimtevaartuig en het omlaag sturen van telemetrie (dat wil zeggen technische en wetenschappelijke gegevens van de instrumenten aan boord). De derde functie is wetenschappelijk onderzoek aan de hand van de verscheidene effecten die de aanwezigheid van hemellichamen en interplanetair medium hebben op het signaal op zijn reis terug naar aarde. Deze toepassing wordt vaak het radiowetenschappelijk experiment van de missie genoemd.

Terwijl de eerste twee functies essentieel zijn voor het welslagen van de missie, is de laatste dat niet noodzakelijkerwijs. Daarom zijn de eerste twee de voornaamste prioriteit van de *deep space networks*: het ondersteunen van navigatie en het besturen en monitoren van de status van ruimtevaartuigen [13]. De derde functie wordt over het algemeen geïmplementeerd door de *deep space network*-faciliteiten in te zetten als grondsegment van radio-wetenschappelijke instrumenten. In dit proefschrift wordt een alternatieve optie voor het gebruik van de *deep space networks* gepresenteerd binnen het domein van radio-wetenschappelijke experimenten: het *Planetary Radio Interferometry and Doppler Experiment* (PRIDE), met radio-occultatieonderzoek als voornaamste toepassing.

De PRIDE techniek is een experimentele opstelling die gebruik maakt van de radiozender aan boord van het ruimtevaartuig en radiotelescoopnetwerken op Aarde, om (1) radiale snelheid en (2) hoekpositie te meten, ter ondersteuning van radiowetenschappelijke experimenten [3–5, 12]. Dit wordt bereikt door met meerdere radiotelescopen op Aarde de Dopplerverschuiving van de draaggolf van het ruimtevaartuig precies te volgen. Een breedband spectraalanalyse wordt toegepast om de topocentrische Doppler-verschuiving van de draaggolf te bepalen, die veroorzaakt

wordt door de relatieve snelheid van de radiozender ten opzichte van de ontvangers van de grondstations. Vervolgens worden deze signalen met elkaar gecorreleerd met behulp van de *near-field Very Long Baseline Interferometry* (VLBI) techniek in fasereferentiemodus. Deze aangepaste versie van de traditionele VLBI techniek vereist een speciaal *near-field* VLBI vertragingsmodel. Het *near-field* VLBI model is bedoeld voor het berekenen van het a priori verschil in aankomsttijd van het gebogen golffront van het signaal bij elk ontvangerpaar, om zodoende een coherent signaal (de zogenaamde 'interferometrische *fringes*') te verkrijgen door de signalen met elkaar te vergelijken. Dit is in feite ook het fundamentele principe van radiointerferometrie [16], met uitzondering van het uitgangspunt dat de bron van het radiosignaal (dat wil zeggen, het ruimtevaartuig) zich op een eindige afstand bevindt van de ontvangers. In het geval van VLBI bevinden de ontvangers zich op grote afstand van elkaar, waardoor onafhankelijke tijdsbepalings- en signaalverwerkingssystemen vereist zijn. Op basis van de informatie van de gemodelleerde *near-field* vertragingen en de fase en frequentie van het resulterende *fringe*-patroon kan de hoekpositie van de radio bron worden bepaald. Dit laatste wordt bewerkstelligd in de zogenaamde fasereferentiemodus [1, 16]. In deze modus worden andere radiosignalen die dichtbij de doelbron staan ($\lesssim$2 deg) gebruikt om de fase van het signaal van het ruimtevaartuig te kalibreren. Natuurlijk radiobronnen die op miljarden lichtjaren afstand staan, en waarvan de positie zeer precies bekend is (tot op tientallen μas), worden over het algemeen gekozen als kalibratiebron. Het bovenstaande vat de PRIDE methodiek, waarmee de hoekpositie en radiale snelheid van het doelvaartuig worden bepaald, kort samen. De radiale snelheid is een bijproduct van de VLBI technologie.

Om de techniek te vergelijken met het traditionele gebruik van *deep space networks* voor radio-wetenschappelijk onderzoek, wordt in dit proefschrift een ruisbudget gepresenteerd van de Dopplerdetecties die met PRIDE verkregen zijn [3]. Als proef werd een volgexperiment gebruikt van de Europese Ruimtevaartorganisatie (ESA) Mars Express (MEX), waarbij het ruimtevaartuig een *fly-by* maakte langs Phobos in december 2013. In dit experiment namen 31 VLBI radiotelescopen gedurende in totaal 26 uur deel aan het volgen van MEX. Om de kwaliteit van de PRIDE Dopplerdetecties te bepalen, werden de stochastische fouten geanalyseerd die geïntroduceerd worden door de instrumenten en door de propagatie van het signaal in de interplanetaire media. Met deze analyse kon het aandeel van de verschillende ruisbronnen in het totale Dopplerresidu worden gekwantificeerd. Deze informatie werd vervolgens gebruikt om een ruisbudget van de observaties op te maken. Daarmee werd aangetoond dat de frequenties in het residu verkregen met PRIDE Dopplerdetecties van vergelijkbaar ruisniveau zijn als die van standaard Dopplerdetectie met NASA's en ESA's *deep space network* antennes ($\sim$2 mHz, het equivalent van $\sim 35\mu$m/s lineair voor drieweg Doppler in X-band).

Na de validatie van de PRIDE methodologie werden zijn toepasbaarheid en prestaties voor planetair atmosferisch onderzoek bestudeerd aan de hand van radio-occultatie-experimenten [2]. Wanneer een ruimtevaartuig zich in een baan om een planeet bevindt, kan het signaal van het vaartuig, vanaf de aarde gezien, bedekt worden door het hemellichaam. Als de planeet een atmosfeer heeft, zal het signaal vlak voor het volledig bedekt wordt, gebroken worden in die atmosfeer, en de resulterende frequentieveranderingen in de draaggolf zullen worden gedetecteerd door de ontvangende grondstations. Door een spectraalanalyse uit te voeren op het

ontvangen signaal en met precieze informatie over de positie en snelheid van het ruimtevaartuig, kunnen de fysische eigenschappen worden afgeleid van het deel van de atmosfeer dat door het signaal is gemonsterd [bijvoorbeeld 6, 8–11, 14, 17].

In dit werk is deze specifieke toepassing van PRIDE beoordeeld door ESA's Venus Express (VEX) te observeren tijdens meerdere occultaties door Venus [2]. Uit deze observaties zijn de dichtheid, temperatuur en luchtdrukprofielen afgeleid van de neutrale atmosfeer van Venus. Met deze proef met VEX is aangetoond dat de PRIDE set-up en verwerkingsprocedure zeer goed toegerust is voor radio-occultatieonderzoek naar planetaire lichamen. Het ruisbudget van de metingen van de VLBI stations toont aan dat de onzekerheid van dezelfde orde grootte is als metingen van NASA's Deep Space Network (DSN) en ESA's ESA Tracking Network (Estrack). Ter illustratie, een onzekerheid in de orde grootte van 2 mHz in het Dopplerresidu resulteert in een onzekerheid van $\sim$0.01 K in het temperatuurprofiel van de neutrale atmosfeer van Venus. Deze resultaten komen overeen met de onzekerheden die gerapporteerd worden in voorgaande radio-occultatie-experimenten, waarbij DSN stations werden gebruikt (bijvoorbeeld Tellmann et al. [15]). Bovendien hebben we aangetoond dat met PRIDE, gebruik makend van de *open-loop* Dopplermetingen, de VLBI stations in staat waren diepere lagen van de dichte atmosfeer van Venus te bemonsteren dan de *closed-loop* Dopplermetingen van Estracks New Norcia. Met de breedband spectraalanalyse van PRIDE toonden we dat het zelfs mogelijk is om met kleine schotelantennes, zoals de 12-m Katherine van AuScope (Australia Northern Territory), het signaal van het ruimtevaartuig te detecteren onder het wolkendek van Venus.

Radio-occultatie-experimenten die worden uitgevoerd met PRIDE kunnen ten volste gebruik maken van de toegang tot grote radiotelescopen in het wereldwijde VLBI netwerk, zoals de 65-m Tianma (China), de 100-m Effelsberg (Duitsland) en de 305-m Arecibo (Puerto Rico). Bovendien kan de set-up, door de brede dekking van de netwerken, worden geoptimaliseerd voor detecties met een hoge *signal-to-noise* (SNR) waarde. Sinds de oprichting zijn de hardware en gegevensverzamelingssoftware van het DSN en VLBI netwerk in nauwe samenwerking ontwikkeld, waardoor vergelijkbare prestaties mogen worden verwacht. Tegelijkertijd is er, verspreid over de aarde, een groter aantal VLBI radiotelescopen dan *deep space network* antennes. Dit stelt ons in staat om slechts die telescopen te selecteren die de beste observatiecondities hebben (met andere woorden, die met de hoogste elevatie), terwijl de *deep space* faciliteiten beperkt zijn in dit soort operationele optimalisatie. De combinatie van uiterst gevoelige telescopen en een brede dekking biedt een geweldige kans, in het bijzonder voor radio-occultatie-experimenten aan planeten of manen met een dichte atmosfeer die worden gekenmerkt door lage SNR waarden.

Op basis van de resultaten in dit proefschrift is aangetoond dat de spectraalanalyse in PRIDE het mogelijk maakt Dopplermetingen af te leiden met een zeer hoge spectraalresolutie. Bovendien voorziet de analyse in precieze Doppler fasecorrecties die essentieel zijn voor het juist correleren van het bronsignaal van het ruimtevaartuig, waardoor correcties van de hoekpositie in zijn vooraf berekende baan precies kunnen worden berekend. Door de prestaties van PRIDE te demonstreren en een ruisbudget op te stellen voor zijn Dopplerdetecties, is aangetoond dat de PRIDE techniek voldoet aan de eisen voor een volledig operationeel radio-wetenschappelijk meetinstrument. Met de radio-occultatieproef met VEX werd specifiek aangetoond dat de PRIDE methode geschikt is voor experimenten waarbij zorgvuldige detectie

van zeer dynamische signalen is vereist. Er mag dan ook worden geconcludeerd dat PRIDE, met zijn wijdverbreide netwerk van radiotelescopen over de hele wereld, een alternatief biedt voor de algemeen gebruikte *deep space networks* voor radio-wetenschappelijke toepassingen. Dit geldt vooral als de aanvragen voor ondersteuning van meerdere *deep space* missies met elkaar conflicteren in het nominale volgschema van de ruimtevaartorganisaties, of als de systemen elkaar kunnen aanvullen, door de wetenschappelijke output te verbeteren van overvluchten die in eerste instantie niet voor radio-wetenschappelijke experimenten zijn bedoeld.

PRIDE is een van de elf experimenten die door ESA zijn geselecteerd voor de L-klasse JUpiter ICy moons Explorer (JUICE) missie, waarvan de lancering staat gepland voor 2022 [7]. Het werk in dit proefschrift zal gebruikt worden in de planning en optimalisatie van de set-up van PRIDE voor radio-occultatieonderzoek naar de atmosfeer van Jupiter. Daarbij is PRIDE betrokken bij de ontwerpstudie ESA EnVision M5 van een satellietmissie naar Venus [18]. Het hoofddoel van PRIDE zal bestaan uit radio-occultatieonderzoek naar de neutrale atmosfeer en ionosfeer van Venus. In zijn huidige vorm is de PRIDE techniek, met de gegevensverwerking en -analyse zoals beschreven in dit proefschrift, geschikt om radio-occultatie-experimenten uit te voeren voor zo goed als ieder planetair ruimtevaartuig.

De persoonlijke contributie van de promovendus is:

- De ontwikkeling van een gedetailleerd ruismodel voor de PRIDE *open-loop* Dopplermetingen.
- Het testen en verbeteren van de bestaande breedband spectraalanalysemethode van PRIDE experimenten voor observaties met lage Signal-to-Noise Ratio (SNR) en hoge signaaldynamica, zoals die verwacht mogen worden bij radio-occultatiemetingen.
- De ontwikkeling van een ad-hoc softwareprogramma waarmee radio-occultatiemetingen kunnen worden verwerkt die verkregen zijn met radiotelescopen met VLBI meetsystemen. Dit programma heeft als input de detecties van het signaal bij de verschillende VLBI stations om het frequentieresidu te berekenen. Eerst worden *open-loop* Dopplermetingen afgeleid uit de ontvangen signalen, en vervolgens van een Dopplervoorspelling afgetrokken die is afgeleid uit de geschatte baan. Daarna worden de parameters van het stralingspad afgeleid uit het Dopplerresidu met behulp van optische geometrie. De link tussen het stralingspad en de fysische eigenschappen van het bemonsterde deel van de atmosfeer wordt gelegd met behulp van het zogenaamde inverse model, dat een Abel inverse transformatie gebruikt. De software is gevalideerd met NASA's Magellan data en ESA's VEX data. Daarom is de software in staat om verschillende gegevensformaten te verwerken. In zijn huidige vorm is de software in staat radio-occultatieobservaties te verwerken, met de aannames dat de atmosfeer sferisch symmetrisch is en de neutrale atmosfeer een constante samenstelling heeft.
- De ontwikkeling van een foutpropagatiemodule die de ruis van het Dopplerresidu kan vinden, afgeleid uit de Dopplerdetecties en de Dopplervoorspellingen. Vervolgens propageert het de onzekerheid in deze frequentieresiduen door de verschillende stappen van het gegevensverwerkingsproces, om uiteindelijk de

onzekerheid van de brekingsindex, dichtheid, temperatuur en luchtdrukprofielen.

De nieuwe resultaten in dit proefschrift zijn:

- Het karakteriseren van de prestaties van PRIDE en het opstellen van een foutbudget van de *open-loop* Dopplermetingen. De onzekerheid die uit onze metingen werd verkregen is vergeleken met die van ESA's Estrack New Norcia station en DSN's Robledo en Goldstone, gedurende de zelfde meetsessie van ESA's MEX ruimtevaartuig, met consistente resultaten tot gevolg.
- De resultaten van het eerste radio-occultatie-experiment uitgevoerd met PRIDE, uit een proef met ESA's VEX ruimtevaartuig. Met deze experimenten werd bewezen dat de PRIDE techniek grote potentie heeft voor atmosferisch onderzoek via radio-occultatiemetingen. De verkregen atmosferische profielen and de bijbehorende foutpropagatieanalyse toonde de consistentie met de resultaten van voorgaand radio-occultatieonderzoek naar Venus.

Alle resultaten zijn gepubliceerd in wetenschappelijke tijdschriften en gepresenteerd in verscheidene internationale conferenties, met een leidende rol voor de promovendus.

References

[1] Beasley, A. & Conway, J. 1995, in Very Long Baseline Interferometry and the VLBA, Vol. 82, 327

[2] Bocanegra-Bahamon, T., Molera-Calvès, G., Gurvits, L., et al. 2018, Accepted to Astronomy and Astrophysics

[3] Bocanegra-Bahamón, T., Molera-Calvés, G., Gurvits, L., et al. 2018, Astronomy & Astrophysics, 609, A59

[4] Duev, D. A., Calvés, G. M., Pogrebenko, S. V., et al. 2012, Astronomy & Astrophysics, 541, A43

[5] Duev, D. A., Pogrebenko, S. V., Cimò, G., et al. 2016, Astronomy & Astrophysics, 593, A34

[6] Eshleman, VR and Tyler, GL and Anderson, JD and Fjeldbo, G and Levy, GS and Wood, GE and Croft, TA. 1977, Space Science Reviews, 21, 207

[7] Grasset, O., Dougherty, M., Coustenis, A., et al. 2013, Planetary and Space Science, 78, 1

[8] Häusler, B., Pätzold, M., Tyler, G., et al. 2007, ESA SP, 1295, 1

[9] Howard, H., Eshleman, V., Hinson, D., et al. 1992, in The Galileo Mission (Springer), 565–590

[10] Kliore, AJ and Anderson, JD and Armstrong, JW and Asmar, SW and Hamilton, CL and Rappaport, NJ and Wahlquist, HD and Ambrosini, R and Flasar, FM and French, RG and others. 2004, in The Cassini-Huygens Mission (Springer), 1–70

[11] Michael Jr, WH and Tolson, RH and Brenkle, JP and Cain, DL and Fjeldbo, G and Stelzried, CT and Grossi, MD and Shapiro, II and Tyler, GL. 1977, Journal of Geophysical Research, 82, 4293

[12] Molera-Calvés, G., Pogrebenko, S., Cimò, G., et al. 2014, Astronomy & Astrophysics, 564, A4

[13] Mudgway, D. J. & Launius, R. 2001, Uplink-Downlink: A History of the Deep Space Network, 1957-1997

[14] Pätzold, M., Neubauer, F., Carone, L., et al. 2004, in Mars Express: The Scientific Payload, Vol. 1240, 141–163

[15] Tellmann, S., Pätzold, M., Häusler, B., Bird, M. K., & Tyler, G. L. 2009, Journal of Geophysical Research: Planets, 114

[16] Thompson, A. R., Moran, J. M., & Swenson Jr, G. W. 2008, Interferometry and synthesis in radio astronomy (John Wiley & Sons)

[17] Tommei, Giacomo and Dimare, Linda and Serra, Daniele and Milani, Andrea. 2014, Monthly Notices of the Royal Astronomical Society, 446, 3089

[18] Widemann, T., Wilson, C., Ghail, R., et al. 2018, in 42nd COSPAR Scientific Assembly, Vol. 42

CHAPTER 1

Introduction

Since 1957, following the launch of Sputnik, radio telescopes around the world have been used to track spacecraft in their journeys throughout the Solar System. These tracking efforts do not only enable navigation (determination and planning of the spacecraft trajectory) and telemetry (acquisition and recording of the measurements taken by the instruments onboard the spacecraft), but also can be used to conduct scientific experiments using the carrier signal of the spacecraft.

In planetary exploration, the term 'radio science' is referred to the experiments and science that can be derived from accurately knowing the position and velocity of the spacecraft and from the interaction of the spacecraft signal with planetary bodies, their gravitational and electromagnetic fields, planetary atmospheres and interplanetary media. Through radio science investigations many planetary bodies in the Solar System have been characterized, by determining their gravitational fields, shapes, masses, ephemerides, magnetic fields, and atmospheric and ionospheric structure [*e.g.* 12, 15, 16, 20, 23, 30, 39]. Additionally, other scientific applications derived from the analysis of spacecraft signal are, for instance, studies of the interplanetary medium and solar plasma [*e.g.* 24, 25, 36, 37, 42], and contributions to experimental relativity investigations, such as the determination of the Parametrized Post-Newtonian (PPN) parameters [1, 35].

The radio science instrumentation consists of the telecommunications subsystem on board the spacecraft (including dedicated Ultra-Stable Oscillator (USO) in the case of one-way operations) and, conventionally, the deep space communication complexes of the major space agencies [27]. However, the main activities of these deep space networks is to provide navigation data and receive telemetry for the whole duration of the mission [26]. The Planetary Radio Interferometry and Doppler Experiment (PRIDE) is an experimental setup that presents an alternative (or additional option) to using the customary deep space networks for radio science investigations, using a wide range of radio telescopes distributed around the globe. The goal is to produce highly accurate radio science observables, which for the case

of PRIDE are accurate Doppler and Very Long Baseline Interferometry (VLBI) observables [4, 9, 10]. These observables are used to determine the radial velocity and angular positioning of the spacecraft, and to examine the variation in the phase and/or amplitude of the carrier signal for scientific purposes.

PRIDE is at is core a VLBI technique. The VLBI technique was conceived in the 1960s as a result of an urge to have higher angular resolutions in astronomy when observing natural celestial sources in the radio domain. VLBI relies on the technique of interferometry to, among other scientific objectives, precisely find the angular position of radio sources in the plane of the sky. This capability was, from the very onset of the technique, recognized for its potential for tracking and positioning of spacecraft in the Solar System [28]. The idea behind using radio interferometry for spacecraft orbit determination in the plane of the sky, resides in the difference between arrival times at the different radio telescopes of the signal transmitted by the spacecraft. This is due to the fact that the positions of the receiving stations on the rotating Earth are different and change in time as the spacecraft signal is received. The difference in arrival time at the telescopes due to the geometry of the tracking array, also known as the geometrical delay, is the key to finding the angular position of the radio source. The theory behind the VLBI technique and its application for spacecraft tracking will be treated in Chapter 2. The data processing and analysis methodology explaining how the radial velocity and angular position are estimated using PRIDE will be treated in Chapter 3.

VLBI observations of spacecraft date back to Apollo 16 and 17 [34], Pioneer Venus probes [6], Voyager [5] and the VEGA balloons [33], among others. The PRIDE technique, as it stands today, was conceived as part of the efforts to track the signal of the European Space Agency (ESA) Huygens Probe, during its descent into Saturn's moon Titan with VLBI radio telescopes in January 2005. The involvement of the VLBI stations was not considered in the original mission design but only up to one and a half years before the probe's descent, as a backup of the Doppler Wind Experiment (DWE). The DWE was designed to make use of the radio link between Huygens and Cassini spacecraft with the goal of determining the direction and strength of Titan's zonal winds from the probe's horizontal motion while immersing into the moon's atmosphere. However, due to a malfunction of the receiver on the Cassini spacecraft, the nominal implementation of the DWE was not possible. Instead, seventeen radio telescopes from multiple VLBI networks around the world were set to receive and record Huygens' signal. These observations achieved the DWE goal and contributed into the derivation of the probe's descent trajectory on the plane of the sky with a linear accuracy in the order of 1 km at 8 AU [40]. The success obtained with this experiment prompted the further development of the methodology, software and logistics that consolidated the PRIDE technique.

Over the period from 2005 to 2019, the use of the PRIDE technique has been demonstrated for multiple radio science applications. Among these, the tracking of the controlled impact of the ESA Smart-1 probe on the surface of the moon [32], tracking of ESA's Mars Express (MEX) during a close Phobos fly-by for its gravitational field determination [10], interplanetary plasma diagnostics and characterization of coronal mass ejections by performing tracking campaigns of ESA's Venus Express (VEX) and MEX[24, 25], sounding of Venus ionosphere and neutral atmosphere by radio occultation experiments with VEX [3], studies to improve the Jovian system

ephemerides in the framework of the upcoming ESA JUpiter ICy moons Explorer (JUICE) mission [7, 8], and contributions to fundamental physics experiments [21]. PRIDE has also been involved in the orbit determination activities of the space radio telescope RadioAstron [19]. RadioAstron's space-ground VLBI observations have enabled astronomical research with the highest angular resolutions to date [11, 22].

The performance of PRIDE and its capability for providing angular position and radial velocity estimates for spacecraft orbit determination have been demonstrated in Duev et al. [9], Duev et al. [10] and Bocanegra-Bahamón et al. [4]. In particular, Bocanegra-Bahamón et al. [4] (presented in Chapter 4 of this thesis) give a noise budget of PRIDE observations, showing that the spectral resolution to which the carrier tone of the spacecraft is detected corresponds to that reported by dedicated deep space agencies [2, 17]. Given the performance and current state-of-the-art of PRIDE, the work presented in this thesis focuses on determining the capability of PRIDE for studying planetary atmospheres by means of radio occultation experiments. Is the wideband spectral analysis carried out with PRIDE sensitive enough to capture the high dynamics of the signal resulting from the planet's atmospheric refraction? Does the PRIDE experimental setup and processing methodology have advantages compared to radio occultation investigations conducted with the deep space complexes?

The radio occultation technique has been carried out by many planetary missions to investigate planetary atmospheres and ionospheres [*e.g.* 13, 14, 18, 29, 31, 38, 41, 43]. Using this technique, the spacecraft carrier signal is detected by the ground station(s) on Earth as it gets occulted by a planet or natural satellite. In this process, the signal is successively refracted as it crosses deeper layers of the planet's atmosphere before being completely occulted by the center body. Therefore, the radio link received on Earth is perturbed, among other contributions, by the presence of the planet's atmosphere. After removing other sources of fluctuations, these perturbations in phase and amplitude can be accurately determined and converted into refractivity profiles of the section of the atmosphere the signal has probed. With the refractivity profile, information regarding the atmospheric properties with altitude can be derived, such as the electron distribution in the ionosphere, the neutral number density in the neutral atmosphere and temperature-pressure profiles of both. Chapter 5 presents a test case scenario of multiple radio occultation observations of VEX where the PRIDE capabilities are demonstrated.

1.1. Thesis goal and research questions

The main goal of this dissertation is to investigate the potential of the PRIDE technique for radio occultation experiments with planetary spacecraft. The definition of the technical approach of this dissertation was based on the following research questions:

1. Given its setup and processing methodology, how does the performance of PRIDE Doppler observables compare to those of the deep space complexes?

    - Conduct simultaneous spacecraft tracking experiments with VLBI radio telescopes and the deep space complexes (*e.g.*, DSN and/or Estrack).

- Provide a detailed noise model for the Doppler detections derived with PRIDE tracking experiments and compare the results with the deep space complexes' counterpart.

2. Are there any improvements or new procedures to be included into PRIDE's processing pipeline to be able to successfully perform radio occultations experiments?

   - Determine whether the wideband spectral analysis carried out with PRIDE is sensitive enough to capture the high dynamics of the spacecraft signal during a radio occultation event. Implement the necessary improvements into the processing methodology.
   - Develop software capable of processing spacecraft signal detections of radio telescopes that use VLBI data acquisition systems, to derive refractivity, density, temperature and density profiles of the target planet during a radio occultation experiment.
   - Test and validate the software with previous radio occultation experiments performed with ground stations from the deep space complexes.

3. What is the effect of the residuals of PRIDE frequency detections on the target planet's atmospheric properties derived from radio occultation observations?

   - Perform an error propagation analysis, starting from the frequency residual uncertainties derived from the detections of the VLBI stations. Propagate these errors through the multiple steps of data processing pipeline to derive the uncertainties in the atmospheric properties of the target planet, resulting from radio occultation observations with PRIDE.

4. What are the advantages of performing radio occultation experiments with PRIDE compared to deep space complexes?

   - Conduct radio occultation observations with ESA's Venus Express spacecraft with PRIDE.
   - Process the observations with the ad-hoc developed software and derive refractivity, density, temperature and pressure profiles of Venus' atmosphere.
   - Analyze and compare the results and its corresponding error propagation analysis with those obtained with Estrack's New Norcia station.

As a starting point, Chapter 2 gives an introduction to the theory behind VLBI and an overview of the use of radio interferometry to perform spacecraft tracking. Chapter 3 describes in detail the current status of the signal processing pipeline and analysis methodology of the PRIDE technique. This chapter explains step by step how standard PRIDE experiments are conducted. Chapter 4 addresses research question 1. For this purpose as a test case an experiment conducted with ESA's MEX spacecraft was used, where the spacecraft was tracked during a fly-by of Mars' moon Phobos, with multiple VLBI stations alongside DSN and Estrack stations. This

chapter provides the formulation of the observed and computed values of the open-loop Doppler data retrieved with PRIDE, and provides a noise budget of the Doppler detections based on the results of the tracking experiment. In order to be able to process radio occultation observations and derive atmospheric properties of the target planet (research question 2), the processing methodology of PRIDE had to be adapted and extended. Section 5.3.1 describes the radio occultation processing pipeline. In order to benchmark the performance of PRIDE for the purpose of radio occultation experiments (research question 3) an error propagation procedure was implemented through the data processing pipeline. Section 5.3.3 describes in detail the implementation of the error propagation analysis. Chapter 5 presents the results of multiple Venus radio occultation experiments performed with PRIDE, where the performance of the technique for this particular application is analyzed (research question 4). Finally, Chapter 6 gives the overall conclusions of this work, and presents recommendations for the preparations of PRIDE as one of the instruments for the upcoming JUICE mission.

References

[1] Anderson, J. D., Lau, E. L., & Giampieri, G. 2005

[2] Asmar, S., Armstrong, J., Iess, L., & Tortora, P. 2005, Radio Science, 40

[3] Bocanegra-Bahamon, T., Molera-Calvès, G., Gurvits, L., et al. 2018, Accepted to Astronomy and Astrophysics

[4] Bocanegra-Bahamón, T., Molera-Calvés, G., Gurvits, L., et al. 2018, Astronomy & Astrophysics, 609, A59

[5] Border, J., Donivan, F., Finley, S., et al. 1982, in Astrodynamics Conference, 1471

[6] Counselman, C., Gourevitch, S., King, R., et al. 1979, Science, 203, 805

[7] Dirkx, D., Gurvits, L., Lainey, V., et al. 2017, Planetary and Space Science, 147, 14

[8] Dirkx, D., Lainey, V., Gurvits, L., & Visser, P. 2016, Planetary and Space Science, 134, 82

[9] Duev, D. A., Calvés, G. M., Pogrebenko, S. V., et al. 2012, Astronomy & Astrophysics, 541, A43

[10] Duev, D. A., Pogrebenko, S. V., Cimò, G., et al. 2016, Astronomy & Astrophysics, 593, A34

[11] Duev, D. A., Zakhvatkin, M. V., Stepanyants, V. A., et al. 2015, Astronomy & Astrophysics, 573, A99

[12] Eshleman, VR and Tyler, GL and Anderson, JD and Fjeldbo, G and Levy, GS and Wood, GE and Croft, TA. 1977, Space Science Reviews, 21, 207

[13] Fjeldbo, G. & Eshleman, V. R. 1968, Planetary and Space Science, 16, 1035

[14] Fjeldbo, G., Kliore, A. J., & Eshleman, V. R. 1971, The Astronomical Journal, 76, 123

[15] Häusler, B., Pätzold, M., Tyler, G., et al. 2007, ESA SP, 1295, 1

[16] Howard, H., Eshleman, V., Hinson, D., et al. 1992, in The Galileo Mission (Springer), 565–590

[17] Iess, L., Di Benedetto, M., James, N., et al. 2014, Acta Astronautica, 94, 699

[18] Jenkins, J. M., Steffes, P. G., Hinson, D. P., Twicken, J. D., & Tyler, G. L. 1994, Icarus, 110, 79

[19] Kardashev, N. 1997, Experimental Astronomy, 7, 329

[20] Kliore, AJ and Anderson, JD and Armstrong, JW and Asmar, SW and Hamilton, CL and Rappaport, NJ and Wahlquist, HD and Ambrosini, R and Flasar, FM and French, RG and others. 2004, in The Cassini-Huygens Mission (Springer), 1–70

[21] Litvinov, D., Rudenko, V., Alakoz, A., et al. 2018, Physics Letters A, 382, 2192

[22] Lobanov, A., Gómez, J., Bruni, G., et al. 2015, Astronomy & Astrophysics, 583, A100

[23] Michael Jr, WH and Tolson, RH and Brenkle, JP and Cain, DL and Fjeldbo, G and Stelzried, CT and Grossi, MD and Shapiro, II and Tyler, GL. 1977, Journal of Geophysical Research, 82, 4293

[24] Molera-Calvés, G., Kallio, E., Cimo, G., et al. 2017, Space Weather, 15, 1523

[25] Molera-Calvés, G., Pogrebenko, S., Cimò, G., et al. 2014, Astronomy & Astrophysics, 564, A4

[26] Mudgway, D. J. & Launius, R. 2001, Uplink-Downlink: A History of the Deep Space Network, 1957-1997

[27] Mulhall, B. 1977, The Deep Space Network Progress Report 42, 39

[28] Ondrasik, V. & Rourke, K. 1971, in AAS/AIAA Astrodynamics Specialists Conference, Fort Lauderdale, Fla

[29] Pätzold, M., Häusler, B., Bird, M., et al. 2007, Nature, 450, 657

[30] Pätzold, M., Neubauer, F., Carone, L., et al. 2004, in Mars Express: The Scientific Payload, Vol. 1240, 141–163

[31] Phinney, R. & Anderson, D. 1968, Journal of Geophysical Research, 73, 1819

[32] Pogrebenko, S., Gurvits, L., Wagner, J., et al. 2006, in Presentation at Cassini, PSG meeting, 21–23

[33] Preston, R., Hildebrand, C., Purcell, G., et al. 1986, Science, 231, 1414

[34] Salzberg, I. 1973, Proceedings of the IEEE, 61, 1233

[35] Shapiro, S. S., Davis, J. L., Lebach, D. E., & Gregory, J. 2004, Physical review letters, 92, 121101

[36] Stone, R., Bougeret, J., Caldwell, J., et al. 1992, Astronomy and Astrophysics Supplement Series, 92, 291

[37] Tappin, S. 1986, Planetary and space science, 34, 93

[38] Tellmann, S., Pätzold, M., Häusler, B., Bird, M. K., & Tyler, G. L. 2009, Journal of Geophysical Research: Planets, 114

[39] Tommei, Giacomo and Dimare, Linda and Serra, Daniele and Milani, Andrea. 2014, Monthly Notices of the Royal Astronomical Society, 446, 3089

[40] Witasse, O., Lebreton, J.-P., Bird, M. K., et al. 2006, Journal of Geophysical Research (Planets), 111, 7

[41] Withers, P., Moore, L., Cahoy, K., & Beerer, I. 2014, Planetary and Space Science, 101, 77

[42] Woo, R. & Armstrong, J. 1979, Journal of Geophysical Research: Space Physics, 84, 7288

[43] Yakovlev, O. I. 2002, Space radio science (CRC Press)

CHAPTER 2

Introduction to Radio Interferometric Techniques for Spacecraft Tracking

Different radio tracking systems on Earth are used for generating radiometric data of spacecraft. These data are used to determine the precise location of a spacecraft along its trajectory throughout its operational life. A detected radio signal provides information about the relative position and velocity of transmitters and receivers. Therefore, if the coordinates of the tracking station are accurately known, the position and velocity of the spacecraft can be inferred.

The communications between ground stations and spacecraft are made within the internationally allocated frequency bands (Table 2.1). Early capabilities for uplinks and downlinks developed by all major space agencies were in the S-band. Gradually, communications have shifted towards higher frequencies; spacecraft started to be equipped with dual-frequency S/X downlinks, then the X-band uplink capability was added to ground stations, and nowadays dual-frequency X/Ka downlinks are available for spacecraft. Further use of the Ka band will continue to increase in the coming decades. The reason to move to higher frequencies is driven by the urge of improving the communications performance and the accuracy of radiometric measurements, by using shorter wavelengths at which the propagation effects through the ionosphere are reduced.

Table 2.1: Uplink and downlink frequencies for deep-space communications [35].

Band	Uplink Frequency (MHz)	Downlink Frequency (MHz)
S	2110-2120	2290-2300
X	7145-7190	8400-8450
Ka	34200-34700	31800-32300

The different types of radiometric data are the range, the Doppler and the inter-

ferometric data. Spacecraft range is a group delay measurement derived from the round-trip transit time of a ranging signal that is generated from a transmitting station. The transmitted carrier signal is received at the spacecraft, by a receiver that locks and tracks the uplink carrier by means of a phase-locked loop. Subsequently, the signal is phase modulated onto the downlink carrier coherently with the uplink carrier but with a frequency offset (as shown in Table 2.1). The received ranging signal will be locked at the receiving station, and will produce a reference signal coherent to the downlink carrier. By measuring the phase offset between the reference signal at the receiving station and the transmitted signal at the transmitting station, the elapsed time between transmission and reception can be determined, and the range ρ can be approximated to $\rho = 1/2tc$, where t is the measured round-trip light time and c the speed of light in vacuum.

Doppler shift is a phase delay measurement derived by comparing the frequency of the received carrier signal f_R with the frequency of the transmitted carrier signal f_T. Hence, for Doppler measurements the observable is not the absolute phase but rather phase change over time. The Doppler shift Δf can be approximated by $\Delta f = f_T - f_R = (\dot{\rho}/c) f_T$, where $\dot{\rho}$ is the spacecraft instantaneous range rate. Therefore, Doppler measurements provide directly one component of the spacecraft state vector, the line-of-sight radial velocity. The actual Doppler extraction process from the received carrier signal as performed by PRIDE will be treated in Section 3.4.

For both, ranging and Doppler, the setting that provides the measurements with the highest accuracy is the so-called two-way mode. In this mode, the transmitting and receiving stations are the same. Hence, the frequency standard used in the phase-lock loops to generate the reference signals for both the uplink and downlink is the same. Another mode is the so-called three-way mode, where the transmitting ground station is different than the receiving ground station, therefore using independent frequency references at each end. However, ground stations typically use hydrogen masers as frequency standards, which provide a stability better than $4 < 10^{-14}$ at $\tau = 10\,\mathrm{s}$ [9]. Therefore, in a three-way mode the noise contribution related to the frequency standard can be expected to be of the same order of magnitude at the transmitting and the receiving station. To this day, the same cannot be said of the so-called one-way mode. In the one-way mode, the spacecraft antenna is the transmitter and the receiving antenna is at a ground station on Earth. In this mode, the frequency reference used onboard the spacecraft is an USO, typically with a stability in the order of 10^{-13} at $\tau = 10\,\mathrm{s}$ [1], one order of magnitude worse than the hydrogen maser. However, with the Deep Space Atomic Clock (DSAC) mission, to be launched in November 2018, an onboard mercury ion atomic clock with a frequency stability in the same order as those obtained on the ground stations will be tested [34]. Besides range and range rate, the spacecraft declination and right ascension can be inferred from long and continuous range and/or Doppler tracking arcs[33]. This information can be derived from the amplitude and phase of the diurnal modulation of the range and Doppler signal. This modulation results from the ground station rotation about the Earth's spin axis.

Until the early 1980s, Doppler and range systems were the only techniques used for interplanetary radio tracking. However, the determination of the spacecraft angular position from long arcs of Doppler and range data can be largely degraded by inaccurate modeling of the forces acting on the spacecraft. This is due to the

fact that the spacecraft angular position is not directly measured by the observables, but rather weakly determined from the diurnal signature of the data. Hence, when estimating the angular positioning parameters, the effect of mismodeled forces that affect the amplitude and/or phase of the data signature can be wrongly interpreted as changes in declination and/or right ascension (refer to Taylor et al. [31] and Thornton & Border [33] pp.35 for examples of this effect). Because of the limitations of Doppler and range tracking for determining the spacecraft angular position, the VLBI technique was adopted in order to directly measure the spacecraft declination and right ascension.

The idea behind the VLBI technique, is that by differencing the radio signal received simultaneously at every two ground stations on Earth a measure of the angular position of the radio source can be derived, as shown in Figure 2.2a. The adaptation of this VLBI technique for navigation was initially implemented by the National Aeronautics and Space Administration (NASA) Deep Space Network (DSN) and it was called Differential One-way Ranging (DOR). The process conducted in order to determine the difference between the time of arrival at the two stations, also known as the total interferometric delay, will be discussed in Section 3.2. As explained in detail in Section 3.2.6, the component of the total interferometric delay from which the angular position of the spacecraft can be derived is the so-called geometrical delay. However, this is not the sole component measured from differencing the arrival time of the signals. Additionally, there are differences in the delays measured due to Doppler, station clock offsets, ionosphere and troposphere propagation, antenna position errors and instrumentation errors. This means that the accuracy to which the spacecraft angular position can be derived, depends on the precision of the total interferometric delay measurement and on the accuracy to which the other components of the total delay, besides the geometrical delay, can be calibrated for. For this end, the so-called phase-referencing technique is used, where a second measurement of an angularly nearby source is introduced. This source is usually chosen to be a natural radio source located at billions of light-years from Earth for which its absolute position is known very accurately. By differencing the observations of the spacecraft signal from those of the reference source, the antenna-dependent errors will be substantially reduced. The remaining errors are related to the spacecraft and reference source position, from which the relative angular position of the spacecraft is derived. The VLBI method used for this is called differently depending of the type of delay measured. The Delta Differential One-way Ranging (ΔDOR) method measures the differential group delay (phase gradient in a frequency range) and the VLBI phase-referencing technique measures the phase delay (the resolution of the phase cycles). Typically, the former is used for spacecraft navigation purposes and the latter for radio science applications.

The use of VLBI observations of spacecraft, also commonly referred to as VLBI tracking, was initially suggested by Ondrasik & Rourke [20] and has been demonstrated on a wide range of deep space missions, such as Apollo 16 and Apollo 17 [27], Pioneer Venus probes [5], Voyager [3], VEGA [24], Huygens Titan Probe [15, 22], Cassini [13], SELENE [10], IKAROS [30], Chang'E [11], Venus Express [7], Mars Express [8], among others.

In this work, the Planetary Radio Interferometry and Doppler Experiment (PRIDE) technique is presented. This is a VLBI phase-referencing technique used for space-

craft tracking that measures phase delay from which the angular position of the spacecraft is derived. Additionally, precise Doppler observables are produced as a by-product of the processing pipeline, from which the radial velocity of the spacecraft is derived. The details regarding the data processing and analysis methodology specific to PRIDE will be treated in Chapter 3. In this chapter, a brief introduction to the VLBI technique is presented in Section 2.1, followed with a review of the use of the VLBI technique for the purpose of spacecraft tracking in Section 2.2.

2.1. Introduction to VLBI

VLBI is a technique that was originated in the field of radio astronomy. This field is considered to be founded by Karl Jansky in 1933, when he published the first detection of the galactic radio emission at a frequency of 20.5 MHz [12]. The discoveries that followed in radio astronomy were initially done with single-dish telescopes. However, these single-dish radio observations are subject to strong diffraction effects, resulting in larger angular resolutions θ than with an optical telescope of the same aperture (following Rayleigh's criterion $\theta \sim \lambda/D$, where λ is the wavelength and D is the telescope's diameter). Soon after Jansky's discovery, it was recognized that it would be prohibitively expensive and technically unfeasible to increase the dish diameters to the sizes needed to improve the poor resolution obtained at radio wavelengths. The solution was found using multiple telescopes, separated by a certain distance, all connected as an interferometer array [25, 26]. Figure 2.1 shows the comparison between the angular resolution of a single dish and a two-element interferometer, while the former is proportional to λ/D the latter is proportional to λ/B, where B is the baseline (*i.e.*, the projected distance between the elements, in a plane perpendicular to the direction the antennas are pointing). In the late 1960s, the conventional interferometer arrays had connected elements, physically limiting the baseline to a maximum of 10 kilometers of length. With the advent of the digital revolution, in which the rapid improvement of the digital electronic equipments benefited the capabilities of the radio interferometers, and the natural tendency of thriving for better angular resolutions, the VLBI technique was conceived. This technique introduced separated array elements, theoretically enabling the use of as large baselines as needed. In practice, the set-up of the VLBI technique enables observations with different radio telescopes located around the world (B_{max} ~10000 km), angular resolutions better than 1 mas (~5 nrad) can be achieved at centimeter and shorter wavelengths. Dedicated VLBI satellites have also been developed to enable a space-borne array element [28]. Such is the case of Roscosmos' RadioAstron [14], that with baselines of 350,000 km enables the longest radio interferometer arrays to date, with angular resolutions in the level of μas. VLBI is currently the technique that provides the highest angular resolution available when observing cosmic sources at any waveband. Its adaptation for spacecraft tracking has been successfully adopted by different space agencies for navigation and enhancement of other scientific experiments that depend on precise orbit determination.

In Sections 2.1.1 and 2.1.2 the hardware and the mathematical treatment of radio interferometry will be treated, respectively.

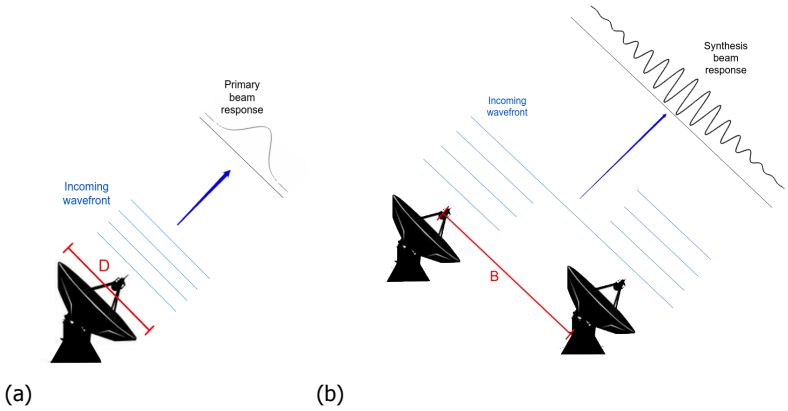

Figure 2.1: Comparison between the resolution of a single dish and a two-element interferometer. The Full Width Half Maximum (FWHM) of the antenna response for the single dish antenna (a) is given by $1.22\lambda/D$, where λ is the wavelength and D is the dish diameter. The FWHM of the synthesized beam response of a two-element interferometer (b) is given by $1.22\lambda/B$ where B is the baseline length.

2.1.1. Technical implementation of VLBI

Let us consider a generic interferometer consisting of two antenna dishes, separated by a baseline length B, each with a receiving system, and a digital backend, as shown in Figure 2.2. The wavefront from a distance source arrives at each antenna, a sensor known as the feed will convert the electric field detected at the focal point of the antenna to an electrical voltage. Hence, the time-dependent voltage signal $v(t)$ generated at the feed will be linearly proportional to the electric field $E(t)$ present at the feed. The amplitude of the initial voltage signal is very small, as it is expected from wavefront generated at a distant source. Therefore, the first step is to amplify the signal while adding as little noise as possible. This is done using a Low Noise Amplifier (LNA), that is kept along with the feed in a cooled chamber in order to minimize the noise contribution from the thermal electron motion. In order to calibrate the received power a thermally controlled resistive load with known properties is injected to the receiving system prior to the observation, coupling it to the input of the LNA. The resistive load is turned on and off during the observation. By measuring the increase in power when it is on the total received power can be calculated.

Once the signal is amplified, it will be heterodyned to baseband. In other words, this means that the signal will be downconverted from the sky frequency to a lower frequency range starting at 0 Hz (*i.e.*, baseband) by a series of mixing and filtering operations. The reference frequency used in the mixing operations comes from the so-called *local oscillator*, which is based on an atomic oscillator with excellent frequency stability (*e.g.*, hydrogen).

When the signal is at baseband it is sampled, digitized and recorded (this last step only for VLBI) in the digital backend. The digitized data coming from the digital backend of each station is input into the correlator. At the correlator is where the interference fringes are formed. As shown in Figure 2.2, when performing an observation, the incoming wavefront will arrive at one element at a time τ_g before

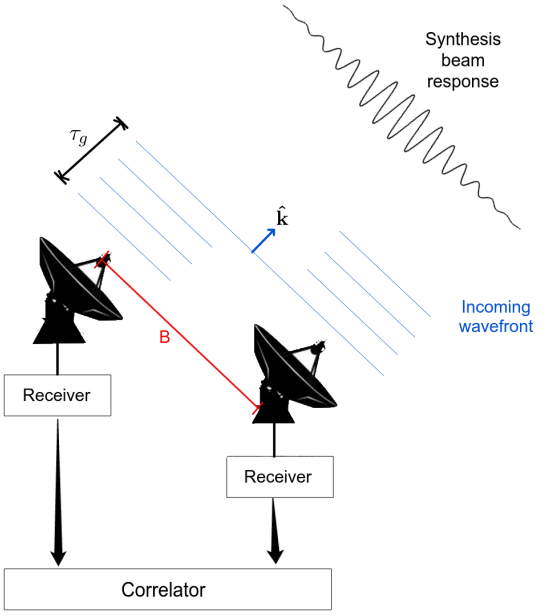

(a) Two-element interferometer. The planar wave reaches the two antennas from the direction $\hat{\mathbf{k}}$, separated by a baseline B on the Earth's surface. The Full Width Half Maximum (FWHM) of the synthesized beam response of a two-element interferometer is given by $1.22\lambda/B$.

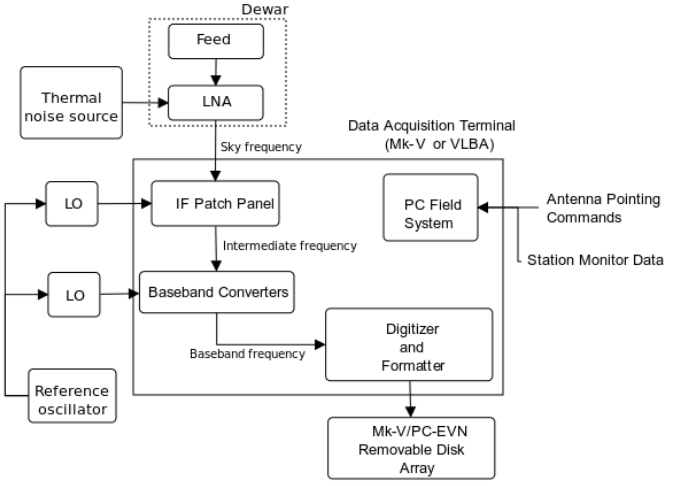

(b) Hardware components of the receiving system of a VLBI station.

Figure 2.2

it reaches the second element of a baseline. As a consequence, the signal detected by each antenna will have a phase difference with respect to the other antenna. To compensate for the total signal delay, $\tau(t)$, (including the geometrical delay, τ_g, and other delays caused by Doppler, propagation and instrumentation effects) the recorded signals are shifted stepwise one against the other and cross-multiplied, until both signals are perfectly aligned. The result of the correlation will be an interference fringe pattern of the radio source with maximum amplitude for signal alignment. In Section 2.1.2 the mathematical formulation of the correlation will be treated.

The main difference between the traditional interferometry, with connected elements, and VLBI lies in the local oscillator and the correlation procedure. In the case of the connected-elements, there is one local oscillator whose signal is distributed to all the antennas, and in the case of VLBI each antenna has an independent local oscillator. As for the correlation, for the former case the correlation occurs directly after the signal is digitized, while for the latter case the data are recorded in disks and delivered to the data processing center where it will be correlated. However, recent developments have allowed the transference of data through high bandwidth fiber optics links from each station to the correlation center, enabling near real-time VLBI correlation. This operational mode is known as eVLBI.

2.1.2. Mathematical treatment of VLBI

In this section an introduction to the theory of radio interferometry will be presented, based on the explanation presented by Thompson et al. [32]. To understand the underlying principle of radio interferometry, let us come back to the simplified two-element interferometer illustrated in Figure 2.2, assuming that the radio source is in the far-field (*i.e*, the incoming wavefront is planar) and it is spatially incoherent. The geometrical time delay τ_g between the antennas is given by

$$\tau_g(t) = \mathbf{b} \cdot \hat{\mathbf{k}}/c \tag{2.1}$$

where $\mathbf{b}$ is the baseline vector and $\hat{\mathbf{k}}$ is the direction of the incoming wavefront (*i.e.*, the direction in which the antennas are pointing).

In the simplest case, assuming the incoming signal is a monochromatic wave of frequency ν, the correlator is a simple multiply and average function. In this way, when considering that each single element has a response of the form $V = v\cos 2\pi\nu t$, and neglecting any propagation and instrumentation effects, the correlator output would be

$$\begin{aligned} r(t) &= \langle V_i(t)V_j(t)\rangle \\ &= \langle v_i\cos(2\pi\nu(t-\tau_g(t)))v_j\cos(2\pi\nu t)\rangle \\ &= \langle v_iv_j(\cos^2(2\pi\nu t)\cos(2\pi\nu\tau_g(t)) + \sin(2\pi\nu t)\cos(2\pi\nu t)\sin(2\pi\nu\tau_g(t)))\rangle \\ &\simeq v_iv_j\cos(2\pi\nu\tau_g(t)) \end{aligned} \tag{2.2}$$

For Earth-based interferometers, τ_g will slowly vary because of the Earth's rotation. This variation is several orders of magnitude smaller than the averaging timescales. Hence, in Equation 2.2, for an averaging period $T \gg 1/\nu$ the average value of $\cos^2(2\pi\nu t) = \frac{1}{2}$ and the average value of $\sin(2\pi\nu t)\cos(2\pi\nu t) = 0$. Therefore,

the resulting signal $r(t)$ will have an oscillation induced by the variation of the term τ_g. This effect is known as the fringe pattern.

Since v_i and v_j are proportional to the electric field of the incident wave, the correlator output $r(t)$ is proportional to the received power. The received power from an element of the source of solid angle $d\Omega$, in the direction $\hat{\mathbf{k}}$ is equal to $A(\hat{\mathbf{k}})I(\hat{\mathbf{k}})\Delta v d\Omega$ where $A(\hat{\mathbf{k}})$ is the antenna effective area, $I(\hat{\mathbf{k}})$ is the source brightness distribution and Δv is the bandwidth of the receiving system. Hence, by integrating over the whole sky ($S \equiv 4\pi$) [1], the correlator output can be written as follows:

$$r(\mathbf{b}_\lambda, \hat{\mathbf{k}}) = \Delta v \int_{4\pi} A(\hat{\mathbf{k}}) I(\hat{\mathbf{k}}) \cos(2\pi \mathbf{b}_\lambda \cdot \hat{\mathbf{k}}) d\Omega \tag{2.3}$$

where $\mathbf{b}_\lambda$ represents the baseline measured in wavelengths. The interferometric image is formed within a small solid angle defined by the antenna primary beams. Assuming the direction to the image center, also known as the phase tracking center, is $\mathbf{k}_0$, then $\hat{\mathbf{k}} = \mathbf{k}_0 + \boldsymbol{\sigma}$, where $\boldsymbol{\sigma}$ is a vector pointing to the source position from the phase center on a plane perpendicular to $\mathbf{k}_0$ (see Figure 2.3). Substituting this into Equation 2.3 yields:

$$\begin{aligned} r(\mathbf{b}_\lambda, \mathbf{k}_0) &= \Delta v \int_{4\pi} A(\boldsymbol{\sigma}) I(\boldsymbol{\sigma}) \cos(2\pi \mathbf{b}_\lambda \cdot (\mathbf{k}_0 + \boldsymbol{\sigma})) d\Omega \\ &= \Delta v \cos(2\pi \mathbf{b}_\lambda \cdot \mathbf{k}_0) \int_{4\pi} A(\boldsymbol{\sigma}) I(\boldsymbol{\sigma}) \cos(2\pi \mathbf{b}_\lambda \cdot \boldsymbol{\sigma}) d\Omega \\ &\quad - \Delta v \sin(2\pi \mathbf{b}_\lambda \cdot \mathbf{k}_0) \int_{4\pi} A(\boldsymbol{\sigma}) I(\boldsymbol{\sigma}) \sin(2\pi \mathbf{b}_\lambda \cdot \boldsymbol{\sigma}) d\Omega \end{aligned} \tag{2.4}$$

Let us introduce the term *complex visibility* V which gives a measure of the coherence of the sky brightness distribution, as given by the antenna response, between an antenna pair. It will be shown subsequently, that given certain assumptions the complex visibility V and the source brightness $I(\boldsymbol{\sigma})$ are Fourier transform pairs. The complex visibility or simply the visibility is defined as,

$$V \equiv |V| e^{i\Phi_V} = \int_{4\pi} \mathcal{A}(\boldsymbol{\sigma}) I(\boldsymbol{\sigma}) e^{-2i\pi \mathbf{b}_\lambda \cdot \boldsymbol{\sigma}} d\Omega \tag{2.5}$$

where $\mathcal{A}(\sigma) \equiv A(\sigma)/A_0$ is the normalized antenna reception pattern and A_0 is the response at the beam center. The modulus and phase of V are equal to the amplitude and phase of the fringes, and V has the dimension of flux density given in Jansky (Jy) where 1 Jy= $10^{-26} W m^{-2} Hz^{-1}$. Replacing the real and imaginary components of Equation 2.5 in Equation 2.4, the output of the correlator can be rewritten as,

$$\begin{aligned} r &= \Delta v \cos(2\pi \mathbf{b}_\lambda \cdot \mathbf{k}_0) A_0 |V| \cos(\Phi_V) + \Delta v \sin(2\pi \mathbf{b}_\lambda \cdot \mathbf{k}_0) A_0 |V| \sin(\Phi_V) \\ &= \Delta v A_0 |V| \cos(2\pi \mathbf{b}_\lambda \cdot \mathbf{k}_0 - \Phi_V) \end{aligned} \tag{2.6}$$

In order to understand the effect that the bandwidth of the receiving system has on the interferometer response, let us consider the response with an infinitesimal bandwidth dv:

[1] Because of the limitations of the primary beam of the antenna, $A(\hat{\mathbf{k}})$ will only be non-zero for a small solid angle

$$dr = A_0|V| \cos(2\pi\nu\tau_g - \Phi_V)d\nu \tag{2.7}$$

Then, for a rectangular frequency band the output signal is:

$$R = A_0|V| \int_{\nu_0-\Delta\nu/2}^{\nu_0+\Delta\nu/2} \cos(2\pi\nu\tau_g - \Phi_V)d\nu \tag{2.8}$$

It can be proved that by replacing $\nu = \nu_0 + \Delta\nu$, the evaluation of the integral in equation 2.8 leads to the following result,

$$R = A_0|V|\Delta\nu \cos(2\pi\nu\tau_g - \Phi_V)\frac{\sin(\pi\Delta\nu_0\tau_g)}{\pi\Delta\nu\tau_g} \tag{2.9}$$

Equation 2.9 shows that if the signals received by the telescopes were to be directly correlated, the correlator would measure the visibility modulated by a *fringe pattern* given by the cosine term, rising from the variation of τ_g as the Earth rotates, which in turn is weakened by a sinc envelope, also known as the *bandwidth pattern*, due to the finite bandwidth of the receiving system. Therefore, to allow the measurement of the actual visibility the effects of the fringe and bandwidth patterns, in addition to frequency conversion, propagation and instrumental effects, have to be accounted for during the correlation process.

Generally, when observing a source with a radio interferometer the desired result is an image of the radio sky brightness distribution $I(\sigma)$. In order to understand the principle of synthesis imaging, in other words, how the sky brightness distribution image is obtained from the corrected output of the correlator (*i.e.*, the complex visibility of the source), let us start by establishing a geometrical relationship between the radio source and the antenna pair. The coordinates for a complex visibility point will be given in units of the observing wavelength λ, with respect to the orthogonal axes $(\hat{\mathbf{u}}, \hat{\mathbf{v}}, \hat{\mathbf{w}})$, whose origin is one of the antennas, with directions towards the celestial East, the celestial North and along the phase tracking center $\mathbf{k}_0$, respectively. The baseline vector is then expressed as $\mathbf{b}_\lambda = u\hat{\mathbf{u}} + v\hat{\mathbf{v}} + w\hat{\mathbf{w}}$. The coordinates of a source in the sky will be given with respect to the orthogonal axes $(\hat{\mathbf{l}}, \hat{\mathbf{m}}, \hat{\mathbf{n}})$, with origin on the phase tracking center position, as follows $\hat{\mathbf{k}} = l\hat{\mathbf{l}} + m\hat{\mathbf{m}} + n\hat{\mathbf{n}}$ (the (l,m) plane is parallel to the (u,v) plane). The synthesized image will represent the projection of the celestial sphere onto the (l, m) plane. As shown in Figure 2.3, from the above definitions the following relations can be established:

$$\mathbf{b}_\lambda \cdot \hat{\mathbf{k}} = ul + vm + wn \tag{2.10}$$

$$\mathbf{b}_\lambda \cdot \mathbf{k}_0 = w \tag{2.11}$$

Since $n = \sqrt{1 - l^2 - m^2}$ then,

$$d\Omega = \frac{dldm}{n} = \frac{dldm}{\sqrt{1 - l^2 - m^2}} \tag{2.12}$$

Thus, substituting Equations 2.10 to 2.12 into Equation 2.5,

$$V(u,v,w) = \int_{-\infty}^{\infty}\int_{-\infty}^{\infty} \mathcal{A}(l,m)I(l,m)e^{[-2\pi(ul+vm+w(\sqrt{1-l^2-m^2}-1))]}\frac{dldm}{\sqrt{1-l^2-m^2}} \tag{2.13}$$

where the integrand is equal to zero for $l^2 + m^2 \geq 1$.

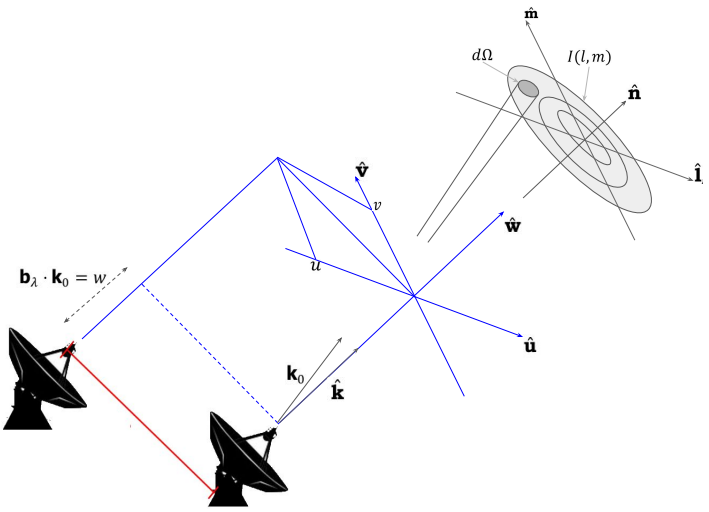

Figure 2.3: Geometry of the interferometer coordinate system (u,v,w) and the source coordinate system (l,m,n).

In order to simplify the inversion of Equation 2.13, it is desirable to reduce this expression to a two-dimensional form. When the synthesized field is small (*i.e.,* when Ω is a small solid angle), which is the case for VLBI, the term $\sqrt{1-l^2-m^2}$ reduces to 1, Therefore by eliminating w from Equation 2.13, the relationship between the visibility and the intensity distribution multiplied by the antenna power pattern reduces to a 2D Fourier transform. Assuming, u and v are computed for the center frequency ν_0,

$$V(u,v) \rightleftharpoons \mathcal{A}I(l,m) \tag{2.14}$$

Equation 2.14 and the discussion presented in this section allows us to conclude that the output of the correlator is the sampled visibility as a function of frequency and time, which once calibrated, can be used to produce an image of the source, yielding the original sky brightness. Throughout this section, multiple assumptions have been made in order to be able to arrive to this conclusion. The limitations and methods to approach the violation of the small synthesized field approximation are treated in Thompson et al. [32]. At the beginning of this section, the incoming signal was assumed to be monochromatic, the non-monochromatic case will be treated in Section 3.2.1. The wavefront of the source signal has been assumed to be planar, however following the criteria given by the Fraunhofer's distance [4], for spacecraft signals within the Solar System this assumption does not hold. The implication of

this will be treated in Section 3.2.6. With Equation 2.9 it was highlighted that several signal effects have to be removed in order to enable the correct measurement of the visibilities by the correlator. The mathematical interpretation of these corrections and their practical implementation will be explained in Section 3.2. Finally, the details concerning the VLBI imaging process will be given in Section 3.3.

2.2. VLBI measurement techniques for spacecraft tracking

In Section 2.1 an introduction to the VLBI technique was given and its mathematical background was treated in order to explain the response of an interferometer. However, in VLBI observations the data processing is not finished after the signals are correlated. In fact, the data reduction actually starts after the signals are correlated, and the procedure to follow strongly depends on what the scientific purpose of the observations is. For the purpose of spacecraft tracking using VLBI, we borrow the underlying theory of radio astrometry, which is to use the error of the true visibility phase of the target source Φ_V (the phase term of the correlator output as shown in Equation 2.6) to calculate the error in the assumed position of the radio source (*i.e.*, corrections to the a priori right ascension and declination of the source).

Let us consider again Equation 2.6. After the signals received by two telescopes are cross-multiplied, the phase term of the response contains the true visibility phase of the target source Φ_V and the geometric phase $\phi_g = 2\pi \mathbf{b}_\lambda \cdot \mathbf{k}_0$. In theory, in order to retrieve Φ_V first the geometric delay is modeled (see Section 3.2.6) and used as input into the correlator to correct for the term τ_g (*i.e.,* a procedure also known as geometrical delay compensation), before performing the actual cross-correlation of the antenna signals. However, this correction depends on the knowledge of the vectors $\mathbf{b}_\lambda$ and $\mathbf{k}_0$, which will inevitably translate in an error in the correlator output phase. This visibility residual phase can be used to calculate the error in the assumed angular position of the target source. VLBI is regularly used to perform this type of astrometric measurements of natural radio sources across the sky [16, 29], but it can also be applied to other radio emitting sources, such as planetary spacecraft, with the appropriate modifications that this requires. This procedure will be discussed in detail in Chapter 3.

In practice, the input model to the correlator needs to correct for the total interferometric delay τ_t. Hence, the model does not only include corrections for the geometric delay τ_g, but also delay corrections related to errors in the propagation of the signal through the atmosphere and ionosphere, instrumental errors, and clock and clock-rate offsets. Therefore, in Equation 2.6 there are several error contributions to the phase of the interferometer response $\phi_{t,\nu} = 2\pi \mathbf{b}_\lambda \cdot \mathbf{k}_0 = 2\pi\nu\tau_t$. By differentiating this relation, it is obtained that the correlator delay errors result in frequency and time dependent errors of the phase,

$$d\phi_{t,\nu} = 2\pi d\tau_t \tag{2.15}$$

and using a first order expansion of Equation 2.15, the interferometer phase error can be written as,

$$\Delta\phi_{t,\nu} = \phi_0 + \left[\frac{\partial\phi}{\partial\nu}\Delta\nu + \frac{\partial\phi}{\partial t}\Delta t\right] \tag{2.16}$$

where $\frac{\partial\phi}{\partial\nu}$ is the *group delay*, $\frac{\partial\phi}{\partial t}$ is the *delay rate* and ϕ_0 is the *phase delay* error. After correlation, the procedure used to estimate the group delay and delay rate residuals is known as *fringe-fitting*, and the procedure used to estimate the phase delay is known as *self-calibration*. These procedures will be treated in Section 3.3. For the discussion in this section, it is sufficient to understand that while both, the group delay and phase delay, are two independent measurables they give the same phase solution but with different precision. The precision of the measurement of the group delay and phase delay are proportional to [21],

$$\sigma(\tau) \propto \frac{1}{\mathrm{SNR} \cdot \Delta\nu}, \quad \sigma(\Phi) \propto \frac{1}{\mathrm{SNR} \cdot \nu_0} \tag{2.17}$$

where SNR is the signal-to-noise ratio of the fringe detection. This means that since the spanned bandwidth, $\Delta\nu$, will be considerably less than the reference frequency, ν_0, the precision of phase delay measurements is much higher than the precision of measurements of group delays. However, the phase delay measurement inherits the problem of ambiguity in resolution because the phase of the cross correlation function can only be determined within a multiple of 2π,

$$\Phi(t) = 2\pi\nu_0\tau + 2\pi n \tag{2.18}$$

Different approaches can be used to resolve this 2π-ambiguity, one of which is discussed in Section 3.6.2.

The VLBI methods of delay measurements for spacecraft tracking can be classified in two types: those that measure the group delay (phase gradients versus frequency), and those that measure the phase delay (the resolution of the phase cycles). In practice, these methods can be used together, depending on the observing strategy and data reduction being used. ΔDOR [6] is an example of a technique that measures the differential group delay, and it is commonly used by various space agencies to support the navigation of interplanetary missions. For navigation purposes the precision given by group delay measurements is sufficient, however, for conducting scientific experiments, such as gravity field determination or measuring properties of planetary atmospheres, more accurate measurements might be desired. The techniques that measure group delay are commonly known as wideband spacecraft interferometry. On the other hand, VLBI techniques that measure the phase delay are known as narrowband spacecraft interferometry. An example of such technique is the Planetary Radio Interferometry and Doppler Experiment (PRIDE), the technique treated and used throughout this thesis.

In conventional VLBI experiments, fringe-fitting and self-calibration are performed on the target data itself, to estimate and remove the large phase errors, delays and delay rates. However, when the target is a weak source, with inaccurate information regarding its position and structure, the SNR is typically low, therefore these techniques, especially when estimating the phase errors, could lead to erroneous solutions. To tackle this problem, a technique known as *phase-referencing* is used, in which during an observation all participating antennas make their measurements alternating between the target source (in our case the spacecraft) and an angularly near-by bright calibrator source, with periods of a few minutes on each. This VLBI mode is used to calibrate the main target signal for propagation effects and other

effect inherent to each antenna. Typically, the reference sources, known as *calibrators*, are extragalactic radio sources, such as quasars, whose absolute coordinates are known to several tens of μas accuracy. By choosing a reference which is no more than a few degrees away from the target signal this type of effects on both, the target and calibrator, can be closely matched. Hence, the fringe-fit and self-calibration solutions of the calibrator can be used to greatly reduce the delay, delay rate and phase errors from the spacecraft signals due to the propagation and antenna-based effects, leaving as the main source of error the measured spacecraft position with respect to its a priori position. This is in a nutshell, the principle behind the VLBI phase-referencing technique for spacecraft tracking.

2.2.1. Involvement of the VLBI networks in spacecraft tracking

The main purpose of the tracking activities of the deep space networks, such as NASA's DSN and ESA's Estrack, is for spacecraft navigation, and telemetry transmission and reception. From the techniques used for navigation, ΔDOR is the VLBI technique used by the deep space networks to provide the angular positioning of spacecraft. With ΔDOR the difference in group delay is measured using specific tones (known as DOR tones) that are modulated onto the downlink carrier signal. Using the bandwidth synthesis technique [6], ΔDOR can achieve 0.2 mas (1 nrad) of angular accuracy, which at 1 AU corresponds to $\sim$150 m in the plane of the sky. The processing scheme of ΔDOR has been optimized to meet the timeliness requirements by the users of navigation data.

There are other networks of radio telescopes around the world that make use of the VLBI technique, observing mainly natural radio sources for scientific purposes. Among these are the European VLBI Network (EVN) and Very Long Baseline Array (VLBA) networks. These networks are routinely used for astrometry, where the carrier phase difference between of the antennas is measured. Because of the wide range of baselines that can be formed with the antennas of these networks, the carrier phase delays ambiguities can be resolved as part of the data reduction process that is routinely performed in VLBI imaging (this process will be discussed in detail in Section 3.6). Angular accuracies in the order of tens of μas can be achieved by measuring the carrier phase delays [8], thus $\sim$5-10 times better than with group delay measurements. These higher accuracies can enable the use of the spacecraft radio signal for scientific experiments, where the burden of having more complex observations, involving more stations, and a non-standardized and more time-consuming data reduction, is not a limiting factor.

The EVN is a consortium of radio astronomy institutes, formed in 1980 and initially composed of five European institutes. Nowadays, the EVN consortium includes 14 institutes, not only in Europe, but also in Asia and South Africa. With its current 21 radio telescopes the EVN is the largest and most sensitive VLBI array in the world (refer to Figure 2.4 and Table 2.2). In an observation, each observing station processes and records the received signal, and then sends the recorded data for correlation to the Joint Institute for VLBI ERIC (JIVE) located in Dwingeloo, the Netherlands.

The VLBA is an interferometer consisting of 10 identical antennas distributed throughout the USA, with transcontinental baselines of $\sim$8000 km between Mauna Kea, Hawaii to St. Croix, Virgin Islands (refer to Figure 2.5 and Table 2.3). The

Table 2.2: Status tables of EVN antennas regularly used in PRIDE experiments.

EVN Observatories	Country	Telescope		SEFD*	Recording	e-VLBI
		Code	Diameter (m)	at X-band	format	capability
Medicina	Italy	Mc	32	320	Mark-5A	Yes
Noto	Italy	Nt	32	770r	Mark-5B	Yes
Matera**	Italy	Ma	20	3000	Mark-3A	No
Onsala	Sweden	On-85	25	1000	Mark-5B	Yes
		On-60	20	1000	Mark-5B	Yes
Sheshan (Shanghai)	China	Sh	25	800	Mark-5B	Yes
Tianma	China	Tm65 (T6)	65	48	Mark-5B	Yes
Nanshan (Urumqi)	China	Ur	25	350	Mark-5B	No
Kunming	China	Km	40	480	Mark-5B	Yes
Metsähovi	Finland	Mh	14	3200r	Mark-5B	Yes
Yebes	Spain	Ys	40	200	Mark-5B	Yes
Arecibo	USA	Ar	305	6	Mark-5A	Yes
Hartebeesthoek	South Africa	Hh	26	630	Mark-5B	Yes
		Ht	15	1400	Mark-5B	Yes
Wettzell	Germany	Wz	20	750r	Mark-5A	No
Svetloe	Russia	Sv	32	200	Mark-5B	Yes
Zelenchukskaya	Russia	Zc	32	200	Mark-5B	Yes
Badary	Russia	Bd	32	200	Mark-5B	Yes

* System Equivalent Flux Density (SEFD), commonly used a measurement of the system's performance. The lower the SEFD is the better the performance.
** Not part of EVN.
r = RHC polarization only.

Figure 2.4: The European VLBI Network (EVN). Credit: EVN.

VLBA is controlled remotely from the Science Operations Center in New Mexico, USA. Each VLBA station consists of a 25 m antenna and a respective control building. The received signals are amplified, digitized, and recorded at each station, and then are sent to the correlator in New Mexico.

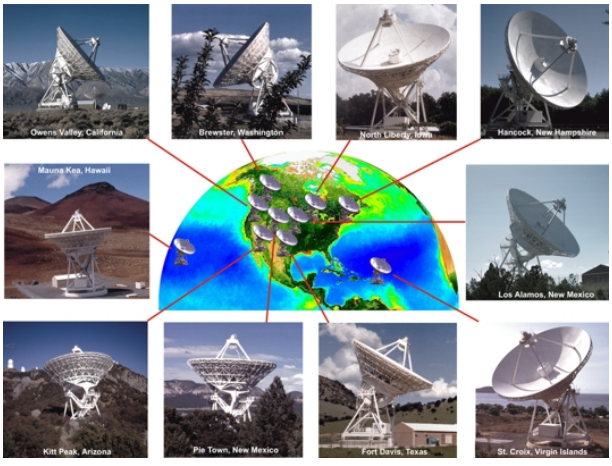

Figure 2.5: The Very Long Baseline Array (VLBA). Credit: NRAO.

The EVN and VLBA activities are primarily related to astronomy research beyond our Solar System and beyond our galaxy. However, the use of the VLBI technique for scientific research where the spacecraft signal is the target radio source has been

Table 2.3: Status tables of the VLBA stations.

VLBA Observatories	Location	Telescope code	
Saint Croix	Virgin Islands	Sc	
Hancock	NH, USA	Hn	
New Liberty	IA, USA	Nl	
Fort Davis	TX, USA	Fd	Diameter: 25 m
Los Alamos	NM, USA	La	SEFD* at X-band: 327
Pie Town	NM,USA	Pt	Recording format: Mark-5C
Kitt Peak	AZ, USA	Kp	e-VLBI capability: No
Owens Valley	CA, USA	Ov	
Brewster	WA, USA	Br	
Mauna Kea	HI, USA	Mk	

*System Equivalent Flux Density (SEFD), commonly used a measurement of the system's performance.

recognized in the last decades. The advantages of using these VLBI networks for narrowband spacecraft interferometry resides mainly in the number of stations that can be used for the observations, and the type of analysis that this feature enables. While the DSN and Estrack use a maximum of 3 stations to produce ΔDOR measurements, with the EVN and/or VLBA the maximum of stations to be used is limited by the visibility of the radio signal from the stations' topocentric position. As an indication, in their current status, ∼15 stations of these networks can be used simultaneously while tracking a spacecraft at ∼1 AU, and a minimum of 4 stations is required in order to be able to correctly perform amplitude calibration [32]. While the key enabling technology of ΔDOR is the DOR tones [6], in the case of the narrowband spacecraft interferometry is the use of multiple baselines that allow the phase ambiguity resolution [8]. This results in a higher angular resolution for the latter (tens of μas, as reported by Duev et al. [8], versus hundreds of μas, as reported by Curkendall & Border [6]). Additionally, the multiple baselines and wide band onto which the signals are recorded allow the detection of much weaker quasars to be used as calibrator sources. This means that calibrators angularly closer to the spacecraft can be used, which will reduce the propagation errors introduced by the difference in the line-of-sight between the spacecraft and the quasar observations.

The advantage of ΔDOR is however, that due to its limited number of simultaneously operating stations and limited bandwidth, the recording and transference of data between ground stations and processing centers is faster. This enables the near real-time derivation of ΔDOR observables which is a key requirement for navigation. It is however important to mention, that while ΔDOR requires DOR tones to operate, narrowband spacecraft interferometry does not require DOR tones and can be conducted while telemetry is being transmitted.

After their consolidation as VLBI networks, the EVN and VLBA have participated in several radio science experiments performing global near-field VLBI tracking of

spacecraft. Among these, the tracking of the descent of ESA's Huygens probe in Titan's atmosphere [36], the impact of ESA's Smart-1 probe on the Moon's surface [23], the tracking of Mars Exploration Rover B (MER-B) spacecraft during the final days before landing on Mars [17], the ephemerides determination of Saturn tracking NASA's Cassini orbiter [13], the tracking of a close fly-by of ESA's MEX by Phobos for gravimetry studies [8], radio occultation observations of ESA's VEX for atmospheric characterization of Venus [2], and the observing campaigns of VEX and MEX for interplanetary plasma and coronal mass ejections studies [18, 19]. In Chapter 3 the PRIDE technique, which regularly uses EVN radio telescopes, will be introduced and a detailed description of its data processing methodology will be given.

References

[1] Asmar, S., Atkinson, D., Bird, M., & Wood, G. 2004, Planetary Probe Atmospheric Entry and Descent Trajectory Analysis and Science, 544, 131

[2] Bocanegra-Bahamon, T., Molera-Calvès, G., Gurvits, L., et al. 2018, Accepted to Astronomy and Astrophysics

[3] Border, J., Donivan, F., Finley, S., et al. 1982, in Astrodynamics Conference, 1471

[4] Born, M. & Wolf, E. 1964, Principles of Optics Electromagnetic Theory of Propagation, Interference and Diffraction of Light, 1

[5] Counselman, C., Gourevitch, S., King, R., et al. 1979, Science, 203, 805

[6] Curkendall, D. W. & Border, J. S. 2013, The Interplanetary Network Progress Report, 42, 193

[7] Duev, D. A., Calvés, G. M., Pogrebenko, S. V., et al. 2012, Astronomy & Astrophysics, 541, A43

[8] Duev, D. A., Pogrebenko, S. V., Cimò, G., et al. 2016, Astronomy & Astrophysics, 593, A34

[9] Finnie, C., Sydnor, R., & Sward, A. 1971, in 25th Annual Symposium on Frequency Control. 1971, IEEE, 348–351

[10] Goossens, S., Matsumoto, K., Liu, Q., et al. 2011, Journal of Geodesy, 85, 205

[11] Huang, Y., Chang, S., Li, P., et al. 2014, Chinese science bulletin, 59, 3858

[12] Jansky, K. G. 1933, Radio Engineers, Proceedings of the Institute of, 21, 1387

[13] Jones, D. L., Fomalont, E., Dhawan, V., et al. 2011, The Astronomical Journal, 141, 29

[14] Kardashev, N. 1997, Experimental Astronomy, 7, 329

[15] Lebreton, J.-P., Witasse, O., Sollazzo, C., et al. 2005, Nature, 438, 758

[16] Marcaide, J. & Guirado, J. 1994, in Very High Angular Resolution Imaging (Springer), 445–447

[17] Martin-Mur, T., Antresian, P., Border, J., et al. 2006, Proceedings 25th International Symposium Space Technol. Sci.

[18] Molera-Calvés, G., Kallio, E., Cimo, G., et al. 2017, Space Weather, 15, 1523

[19] Molera-Calvés, G., Pogrebenko, S., Cimò, G., et al. 2014, Astronomy & Astrophysics, 564, A4

[20] Ondrasik, V. & Rourke, K. 1971, in AAS/AIAA Astrodynamics Specialists Conference, Fort Lauderdale, Fla

[21] Petrov, L. 1999, in Proceedings of the 13th Working Meeting on European VLBI for Geodesy and Astrometry

[22] Pogrebenko, S., Gurvits, L., Campbell, R., et al. 2004, in Planetary Probe Atmospheric Entry and Descent Trajectory Analysis and Science, Vol. 544, 197–204

[23] Pogrebenko, S., Gurvits, L., Wagner, J., et al. 2006, in Presentation at Cassini, PSG meeting, 21–23

[24] Preston, R., Hildebrand, C., Purcell, G., et al. 1986, Science, 231, 1414

[25] Ryle, M. 1952, in Proceedings of the Royal Society of London A: Mathematical, Physical and Engineering Sciences, Vol. 211, The Royal Society, 351–375

[26] Ryle, M. & Vonberg, D. 1946, Nature, 158, S82

[27] Salzberg, I. 1973, Proceedings of the IEEE, 61, 1233

[28] Schilizzi, R. 2012, in Resolving The Sky-Radio Interferometry: Past, Present and Future, Vol. 163, SISSA Medialab, 010

[29] Shapiro, I., Wittels, J., Counselman III, C., et al. 1979, The Astronomical Journal, 84, 1459

[30] Takeuchi, H., Horiuchi, S., Phillips, C., et al. 2011, in General Assembly and Scientific Symposium, 2011 XXXth URSI, IEEE, 1–4

[31] Taylor, T., Campbell, J., Jacobson, R., et al. 1984, Journal of Guidance, Control, and Dynamics, 7, 301

[32] Thompson, A. R., Moran, J. M., & Swenson Jr, G. W. 2008, Interferometry and synthesis in radio astronomy (John Wiley & Sons)

[33] Thornton, C. & Border, J. 2003, Radiometric Tracking Techniques for Deep Space Navigation, 1st edn. (Wiley-Interscience)

[34] Tjoelker, R. L., Prestage, J. D., Burt, E. A., et al. 2016, IEEE transactions on ultrasonics, ferroelectrics, and frequency control, 63, 1034

[35] Wertz, J. & Larson, W., eds. 1999, Space Mission Analysis and Design, 5th edn. (Microcosm Press & Kluwer Academic Publishers)

[36] Witasse, O., Lebreton, J.-P., Bird, M. K., et al. 2006, Journal of Geophysical Research (Planets), 111, 7

CHAPTER 3

Description of the PRIDE technique: signal processing pipeline and analysis methodology

In Chapter 2 the VLBI technique was introduced and its application for spacecraft tracking. In this chapter, current status of the signal processing pipeline and analysis methodology of the Planetary Radio Interferometry and Doppler Experiment (PRIDE) technique will be presented. PRIDE can be defined as an experimental setup which utilizes a wide range of Earth-based radio telescopes and their respective facilities to perform spacecraft tracking observations, and several *ad hoc* signal processing software to provide precise estimates of the spacecraft state vector. This is achieved using a narrowband spacecraft interferometry approach, were the differenced carrier phase delay and Doppler carrier phase corrections are determined to estimate the spacecraft angular position and radial velocity. Combined with the analysis of the changes in phase and amplitude that the spacecraft carrier signal undergoes as it interacts with the planetary bodies and the interplanetary media, PRIDE can be used in multiple radio science experiments, such as Solar corona and Solar wind research, determination of gravitational properties of planets, planetary atmospheric studies, planetary rings characterization, determination of planetary ephemerides, among others. In this work, the particular application for planetary atmospheric characterization via radio occultation experiments will be treated in Chapter 5.

PRIDE is a technique based on the VLBI phase-referencing principle, that has been adapted to observe planetary spacecraft as its main target. Because PRIDE applies phase-referencing, all telescopes participating in the experiment will make their observation measurements alternating between the spacecraft and an angularly nearby background source, with periods of a few minutes on each. Unless, the separation of the target and calibrator sources is sufficiently small. In this case, the calibrator is also detected within the antenna primary beam when pointing at the target source, which means that all the observing time is spent on the target. This mode is known as in-beam phase-referencing. In order to be able to use the

reference source signal as a calibrator, the coherency of phases between the two signals - spacecraft and reference source - must be ensured. Therefore, it is essential that both signals are recorded onto the same standard VLBI recording medium (*e.g.*, Mark-5 disk packs).

By maximizing the cross-correlation of the signals between every two antennas in the observing array, the interferometer measures the geometric delay. With this information and with the phase and frequency of the resulting interference fringe pattern, the parameters of both the baseline (i.e., the projected distance between two antennas, in a plane perpendicular to the direction the antennas are pointing) and the source position, can be determined. The procedure used to solve for the baseline and source position vectors is a common practice in radio astrometry with VLBI systems. In VLBI position measurements, the method that delivers the highest accuracy is called phase referencing. This approach consists of finding the relative position of the main radio source with respect to an angularly near-by source, for which its absolute position its known to high degree of accuracy ($\sim$0.1 mas). For the PRIDE technique, we borrow the underlying theory behind radio astrometry using the phase referencing method and apply it for spacecraft positioning, with the appropriate modifications that this requires.

The first step in the PRIDE technique is to perform precise Doppler tracking of the spacecraft carrier signal on every antenna involved in the tracking session. As PRIDE uses the phase referencing method, in the nominal setup of the technique we observe two types of sources, the spacecraft signal and a (multiple) closely spaced natural radio source(s) [10]. The latter are known as phase calibrator sources, which are usually sources used to define the International Celestial Reference Frame (ICRF). Because of the nature of the radio sources, *i.e.*, a weaker natural radio source that emits broadband electromagnetic radiation covering ranges in the order of gigahertz in the frequency domain, and a stronger artificial radio signal that spans only a fraction of a millihertz, we perform wideband spectral analysis to filter out the spacecraft carrier signal from the several MHz of bandwidth on which both signals are recorded. With this procedure, the topocentric Doppler shift of the carrier signal can be extracted for every station. This is the first product of the PRIDE technique, the open-loop[1] Doppler detections.

In order to find the angular position of the spacecraft with respect to the phase calibrator, the received signals of both sources have to be correlated separately. To proceed with the correlation two delay models are used, one for the background calibrator source and one for the spacecraft signal. This is due to the fact that the background sources are usually quasars located at billions of light-years away from the Earth, for which their wavefront can be assumed to be planar as it approaches the ground stations. In this case, a far-field model can be used for the geometric delay compensation of the different antennas of the interferometric array. If the distance to the source is $R \leq D^2/\lambda$ from the telescope's aperture, where D is the characteristic aperture size and λ the radio wavelength, this assumption does not hold. Using this so-called Fraunhofer criterion [4], all the radio signals transmitted within our Solar system at Ka-, X- and S-bands cannot be treated as planar wave-

[1]The concept of open-loop will be properly introduced in Chapter 4. At this point, it is sufficient to know that this name is used to describe the PRIDE Doppler products because a wideband spectral analysis approach is used to derive them.

fronts. For this reason, when processing spacecraft signals, a near-field delay model should be used to correct for the curvature of the wavefront as it approaches the receivers on Earth. For the correlation the data processing pipeline is split in three branches: broadband correlation of the background source with the far-field delay model, broadband correlation of the spacecraft broadband data with the near-field delay model and narrowband correlation of the spacecraft carrier tone with the near-field delay model. Figure 3.1 shows the overall PRIDE data processing block diagram. In this chapter the experiment design and logistics will be discussed in Section 3.1. In Section 3.2 the practical implementation of the correlation procedure will be described. Section 3.3 describes the output of the correlation and post-processing of the broadband reference source data. Sections 3.4 and 3.5 described the narrowband and broadband spacecraft signal processing, respectively. Finally, Section 3.6 describes the application of phase-referencing and the estimation of the spacecraft angular position corrections.

3.1. Experiment design, data acquisition and logistics

PRIDE observations are usually conducted on the basis of peer-reviewed proposals (open sky policy), for the EVN and other VLBI networks, to request the observation time for the telescopes participating in the experiment. Once the scientific proposal is approved, the telescopes need to be scheduled. Within the VLBI community it is customary to define any wideband VLBI experiment by means of the VLBI experiment (VEX) file. The program that allows to create such files is called SCHED [2], which is currently the standard program used to schedule any EVN, VLBA, Very Large Array (VLA) and Global VLBI observations.

SCHED uses as input a text file that describes the experiment schedule. The program has at its disposal accurate information regarding station locations and equipment, radio source positions and frequency setups from a wide number of catalogs. After running SCHED on the input file, it generates different output files; one of these is the VEX file. This file format contains a complete description of the VLBI experiment to be carried out, including scheduling, data acquisition and correlation. In order to create the SCHED input text file that describes the experiment schedule the following information needs to be determined:

Spacecraft position The a priori spacecraft position is obtained using the Jet Propulsion Laboratory (JPL) SPICE software [1]. SPICE is an information system developed by NASA's Navigation and Ancillary Information Facility (NAIF) widely used by different space agencies to plan, model and execute different activities related to planetary missions. The principal system components of SPICE are the so-called kernels, which are data files containing ancillary data, and the SPICE toolkit, which is the software package itself (consisting of a subroutine/function library and a number of programs). The SPICE kernels are developed by the mission operations center of the target spacecraft and are usually available for public use. However, if for the target of interest there are

[2] http://www.aoc.nrao.edu/software/sched/

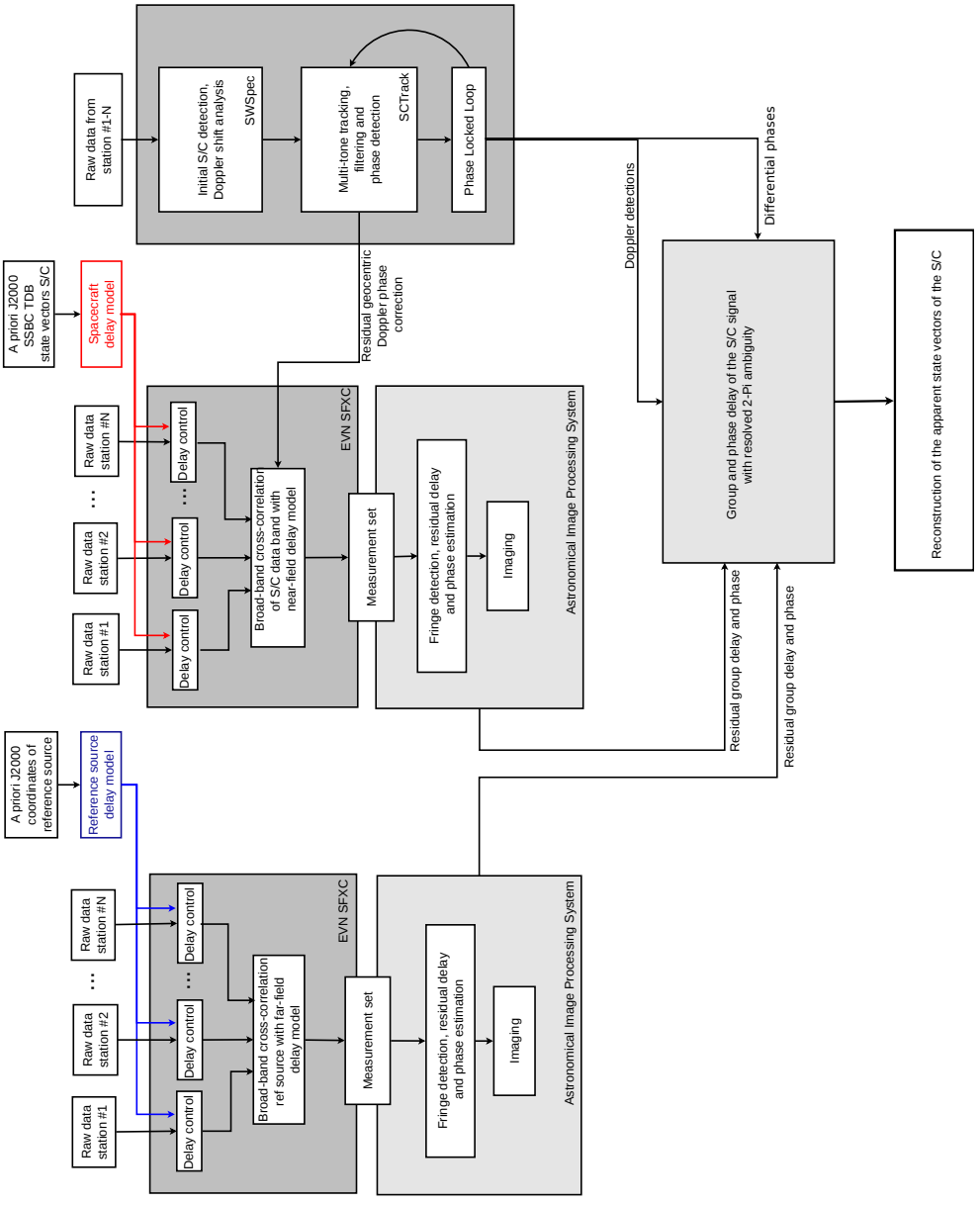

Figure 3.1: Block diagram of PRIDE data processing pipeline.

no SPICE kernels available these have to be generated, using as input a list of discrete state vector estimates of the spacecraft.

Additionally, other kernels need to be generated: an spk-file containing the locations of the EVN stations, and their corresponding topocentric frame kernels (fk-file) with respect to the Earth body-fixed frame (*e.g.*, ITRF2000). Currently, the reference used for the planetary ephemeris is the DE430 series [16], and, for the Earth's orientation was the high accuracy EOP-based kernel, which are updated on a weekly basis by NAIF. Once all these kernels are created, the spacecraft state vectors with respect to each station are evaluated using built-in SPICE routines, in Terrestrial Dynamical Time (TDT) time system and reference frame J2000, corrected for one-way light time and stellar aberration. Then, the obtained state vectors in rectangular coordinates are converted to right ascension and declination coordinates, to serve as input for the antenna pointing.

The advantage of using SPICE for this purpose is that the ephemerides of the spacecraft, of the ground stations and of any collection of solar system bodies can be generated and used under a common file format, which can be easily accessed by a common set of functions. Additionally, SPICE allows the calculation of the antenna elevation during the observation in order to select the best configuration. In the case of radio occultation investigations, SPICE easily allows the identification of the occultation periods of the spacecraft signal by any celestial body.

Participating stations Once the observation proposal is accepted, it is known which stations will take part on the observation. The locations of the stations are supplied by the locations catalog which is available within the SCHED program.

Observation band The observation band (S,X or Ka) for the experiment is chosen depending on the communications architecture of the target spacecraft. Naturally, the band availability on the antennas has to be considered when preparing the experiment.

Frequency setups The Radio Frequency (RF) range to be covered, the local oscillator and polarization of each Intermediate Frequency (IF) have to be specified in the so-called frequency catalog file. A set of channels for the observation band needs to be defined. In order to get high precision measurements, the channel frequencies span should be wide, since the two outermost channels determine its precision.

Calibrators and fringe finders Strong background radio sources are selected to be used as fringe finder and as phase reference calibrator from the calibrators list published by Petrov [30]. Usually, as fringe finder (which is used to find interferometric fringes, for clock search and bandpass correction) the strongest compact source angularly in the vicinity of the spacecraft ($\lesssim$10 deg) is chosen, and as phase-reference calibrator, a rather strong compact source but as angularly close to the spacecraft as possible, should be chosen. Preferably, within $\sim$2 deg from the spacecraft. These calibrators are chosen using a nearest-neighbor algorithm that fits the calibrators' positions to the spacecraft position

on the sky during the observation. The best case scenario would be to have both the spacecraft and phase-referencing source within the antenna beam. This modality is known as in-beam VLBI phase-referencing. This mode has two advantages: firstly, all observing time is spent pointing at the target and observing both sources, and secondly, because the observations are simultaneous and covering the same patch of the sky the phase calibration will cancel out the same propagation and antenna-based phase errors, including the phase variability in short timescales.

Nodding cycle The nodding cycle specifies the amount of time that will be spent observing the spacecraft and the calibrator, and the time needed to re-point the antennas between the two sources. Because of the random nature of the varying atmospheric and ionospheric phase errors, the duration of the switching time τ_s between sources has to ensure that the path length change due to these phase errors is $< \lambda/4$, where λ is the signal wavelength [2]. If this condition is not met, there can be ambiguities introduced when connecting the phase between the spacecraft and calibrator observations (*i.e.*, extra 2π turns of the phase between observations). As explained by Beasley & Conway [2], using this requirement the critical switching time τ_s can be derived: $\tau_s(\max \text{ in minutes}) = 25\lambda^{6/5}\cos^{3/5}(z)C_n^{-6/5}v^{-1}$, where z is the zenith angle, C_n is the tropospheric refractive density in units of $10^{-7}\,m^{-1/3}$ and v is the turbulence screen velocity. Generally, in PRIDE experiments two modes of nodding cycle are used. The VLBI mode with a short nodding cycle, for instance of 5 minutes, of which 2 minutes are spent observing the calibrator, 2 minutes on the spacecraft and 1 minute of switching time. The Doppler mode has a longer nodding cycle, for instance of 20 minutes, of which 2 minutes are used to observed the calibrator, 17 minutes the spacecraft and 1 minute for re-pointing. This nodding cycle chosen is then repeated for the length of the observation. Each time slot when the antenna is observing a specific target, whether it is the spacecraft or target, is called a *scan*. In the optimal case of in-beam VLBI phase-referencing, the whole observing time is spent pointed at the target, picking up simultaneously both the spacecraft and calibrator signals.

Once this file is sent to each participating station, its parameters are read by the Personal Computer Field System (PCFS) which uses the DRUDG program [42] to translate them into the necessary antenna pointing to conduct the experiment. During the experiment, the incoming radio signal, whether it is coming from the calibrator or the spacecraft, is captured by each antenna participating in the observation, as explained in Section 2.1.1. Subsequently, at each receiver, the signal is amplified by a cryogenically-cooled LNA and downconverted from the RF signal to an IF. The signal is forwarded to the VLBI Data Acquisition System (DAS) where the baseband converters mix the IFs with a local oscillator derived from the station frequency standard using the single-sideband mixing technique. This results in two filtered baseband channels corresponding to the upper and lower sidebands centered about the local oscillator frequency. The outputs of the baseband converters are routed to the Mark-5 formatter where they are digitized using 2-bit digitization, placed into recording frames and sent to a disk array. The recorded data is then transferred to the correlation center in JIVE, either in real-time in the *e-VLBI* mode or after the experiment is

completed, where it will be processed and analyzed. In Chapter 2, Figure 2.2 shows a basic schematic diagram of the typical VLBI station equipment.

3.2. Correlation

In Section 2.1.2 a mathematical description of the correlation was given, showing that the correlator is considered to be the 'lens' of a VLBI telescope array, since it is at the correlator where the interference fringes are formed, and the complex visibility is measured. In this section, the practical implementation of the correlation process in PRIDE experiments will be treated (the mathematical description is based on Thompson et al. [41]). As shown in Figure 3.1, bare in mind that the PRIDE processing pipeline deals with the correlation of two different streams of data: the raw broadband spacecraft data and the raw broadband calibrator data.

3.2.1. Correlation of quasi-monochromatic electromagnetic radiation

The mathematical treatment given in Section 2.1.2 assumes the unrealistic case of an incoming wave from the source that is monochromatic of frequency ν. In reality, the electric field detected will produce a band-limited signal, centered at a frequency ν_0. Therefore, it is convenient to represent the electromagnetic radiation from the source as a quasi-monochromatic plane with an electric field component given by the real part of

$$E(t+\tau_{gc,i}) = A(t+\tau_{gc,i})e^{i2\pi\nu_0(t+\tau_{gc,i})} \tag{3.1}$$

where $A(t+\tau_{gc,i})$ is a complex, band-limited process, centered at ν_0, which is covariance-stationary, ergodic and stochastic, and $\tau_{gc,i}$ is the signal delay between the station i and geocenter.

The spectral representation of $A(t+\tau_{gc,i})$, as a band-limited process, can be written as follows,

$$A(t+\tau_{gc,i}) = \int_{-\infty}^{\infty} s(\nu)e^{i2\pi\nu(t+\tau_{gc,i})}d\nu \tag{3.2}$$

where $s(\nu) = 0$ for $|\nu| \leq B$, where B is the bandwidth.

As explained in Section 2.1.2, an interferometer measures the expectation of the cross-correlation of the signal received at two stations. For the case of a band-limited quasi-monochromatic signal this results in:

$$\begin{aligned} r_{i,j}(\tau) &= \left\langle E_i(t+\tau_{gc,i})E_j^*(t+\tau_{gc,j})\right\rangle \\ &= \left\langle E_i(t+\tau_g)E_j^*(t)\right\rangle \\ &= \left\langle A(t+\tau_g)A_j^*(t)\right\rangle e^{i2\pi\nu_0\tau_g} \\ &= \gamma_{ij}(\tau)e^{i2\pi\nu_0\tau_g} \end{aligned} \tag{3.3}$$

and, since $A(t)$ is ergodic, the expectation, denoted by the angle brackets, can be approximated by averaging with respect to t. In this equation the term τ_g is the geometrical time delay, as defined in Equation 2.1, between stations i and j. Since the angle between the baseline vector $\mathbf{b}$ and the source unit vector $\hat{\mathbf{k}}$ changes as

the Earth rotates, τ_g will change throughout the observation giving rise to the fringe pattern of the interferometric signal. The term γ_{ij} is the covariance function of the stochastic process $A(t)$, which as shown in Section 2.1.2, is the unmodulated correlation between the electric fields detected at each of the two stations, *i.e.,* the visibility. This term, γ_{ij}, is modulated by the fringe signal given by the phasor in τ_g.

Using the spectral representation of $A(t)$ given in Equation 3.2, γ_{ij} can be written as,

$$\begin{aligned}\gamma_{ij}(\tau) &= \left\langle A(t+\tau_g)A_j^*(t)\right\rangle \\ &= \left\langle \int_{-\infty}^{\infty}\int_{-\infty}^{\infty} s_i(\nu)s_j^*(\nu')e^{i2\pi[(\nu-\nu')t+\nu\tau_g]}d\nu d\nu' \right\rangle \\ &= \int_{-\infty}^{\infty} S_{ij}(\nu)e^{i2\pi\nu\tau_g}d\nu \end{aligned} \tag{3.4}$$

where $S_{ij}(\nu)$ is the cross-power spectrum of $A(t)$,

$$S_{ij}(\nu) = s_i(\nu)s_j^*(\nu) = \int_{-\infty}^{\infty}\gamma_{ij}(\tau)e^{-i2\pi\nu\tau}d\tau \tag{3.5}$$

Equation 3.5 shows that the term we want to obtain $S_{ij}(\nu)$, which is the visibility, is simply the Fourier transform of the covariance function $\gamma_{ij}(\tau)$. Therefore in practice, a correlator must convert the time domain signal into the frequency domain and compensate for the phasor term $e^{i2\pi\nu_0\tau_g}$ shown in Equation 3.3. This compensation also includes the effects of frequency conversion and digital sampling of the signal, and the fractional sample error remaining after the geometrical delay is corrected for. The steps necessary to correct for these effects will be treated in Sections 3.2.2 and 3.2.3.

3.2.2. Baseband conversion and sampling

Let us consider the frequency conversion that occurs at the VLBI station when observing a source. The received field at the station i, which is given by Equation 3.1, is converted to baseband by a real single sideband mixer with Local Oscillator (LO) frequency ν_0:

$$V_i(t+\tau_{gc,i}) = E_i(t+\tau_{gc,i})\times\cos 2\pi\nu_0 t = A(t+\tau_{gc,i})\left(\frac{e^{i2\pi\nu_0\tau_{gc,i}} + e^{i2\pi\nu_0(2t+\tau_{gc,i})}}{2}\right) \tag{3.6}$$

The output of the down-conversion is the real part of Equation 3.6. For the sake of simplicity, the mathematical treatment here assumes only a single conversion step to baseband, while in reality this is usually a multi-stage process including broad front-end filters, a couple of IF filters and sometimes digital filtering after sampling. Applying a low-pass filter after the conversion to baseband removes the high-frequency term from Equation 3.6. At this point, the frequency and phase offsets between the LOs of the different stations are ignored. This is accounted for at a later stage during the fringe-rotation and fractional sample error corrections, as explained in Section 3.2.3.

After the frequency conversion, the baseband signal V_i is sampled with a sampling interval no longer than $\Delta t = 1/2B$, in order to avoid aliasing, through a non-linear sampling function $f[]$:

$$R_i(n) = f[V_i(t = n\Delta t)] \tag{3.7}$$

Once the signal is sampled, the operations of the signals are conducted on discrete digital samples. However, the continuous notation is generally preferred in literature when explaining the following steps for the sake of clarity. The digital samples are recorded on disk packs.

3.2.3. Geometrical delay compensation and fractional delay error correction

In order to be able to correctly correlate the antenna signals, the correlator has to account for the changing geometric delay τ_g. As shown in Figure 3.2, this is done by delaying the sampled signal $R_i(n)$ by N integer samples, where N is the rounded number of $t_{gc,i}/\Delta t$ and Δt is the sampling interval:

$$P_i(t) = V_i(t + \tau_{gc,i} - N\Delta t) = A(t + \tau_{gc,i} - N\Delta t)e^{i2\pi\nu_0\tau_{gc,i}} \tag{3.8}$$

The remaining error due to the integer sample shift, known as the fractional delay error, is equal to $\epsilon_i = \tau_{gc,i} - N\Delta t$. A phase rotation, also known as fringe rotation,

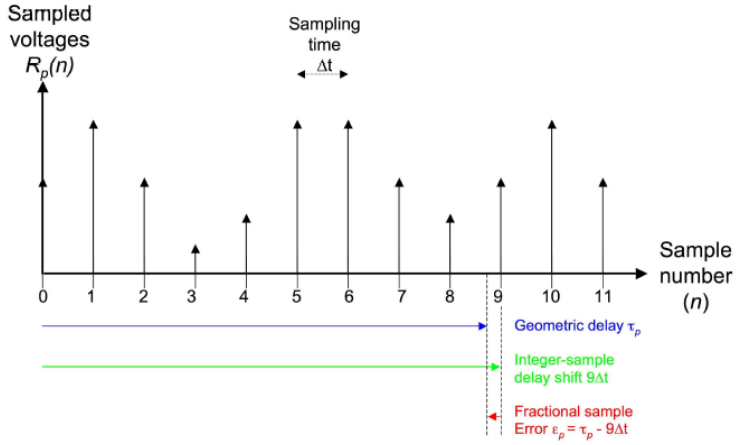

Figure 3.2: Delay compensation. Credit: Deller et al. [9]

must also be applied in order to stop the fringe signal. This is done by applying the phase rotation $\theta_i = 2\pi\nu_0\tau_{gc,i}$ as a complex mixer, which conceptually speaking means performing a complex multiplication to P_i by a function $e^{-i\theta_i}$. This procedure yields a shifted, fringe-rotated baseband signal, whose output is the real part of:

$$X_i(t) = P_i(t)e^{-i\theta_i} = A(t + \epsilon_i) \tag{3.9}$$

The last step is to remove the fractional delay error, for which the the signal that has been shifted and fringe-rotated into the frequency domain:

$$\mathcal{F}\{A(t+\epsilon_p)\} = s_\nu e^{i2\pi\nu\epsilon_i} \tag{3.10}$$

and the resulting spectrum is multiplied by $e^{-i\theta_{frac}}$, where the phase $\theta_{frac} = 2\pi\nu\epsilon_i$. In practice, this correction is implemented by dividing the data into segments of N samples, to which a Fast Fourier Transform (FFT) is applied. The selection of the number of samples N and windowing function to which the segments are multiplied is discussed in [21]. With this final step, the exact spectral representation of the original signal $s(\nu)$ is recovered.

3.2.4. Cross-correlation and normalization

After the previous steps (delay compensation, fringe rotation and fractional-sample error correction) have been applied to all the signals coming from each station, the cross-correlations (along with the auto-correlations for each station) are computed for all possible baselines (for an array of K elements there are $K(K-1)/2$ baselines):

$$S_{ij}(\nu) = s_i(\nu)s_j^*(\nu) \tag{3.11}$$

where i and j are the two radio elements forming a baseline. The cross correlation results are integrated for a user-specified time interval (usually 1 second). After integration, the visibility data are normalized - using the total power information of the signal per telescope derived from the auto-correlations - and stored in a disk.

3.2.5. JIVE's software correlator SFXC

For PRIDE experiments the broadband and narrowband correlation is carried out with the EVN Software FX Correlator (SFXC), developed and operated at JIVE [21]. The SFXC is based on the original design developed for VLBI tracking of the Huygens probe as it entered the atmosphere of Saturn's largest moon Titan [18]. As indicated by its name, the SFXC is a correlator of the FX type [32], and its correlation algorithm is implemented by a software designed to run on a standard Linux cluster. As discussed in the previous section, the visibility output of the correlator can be formed by Fourier (F) transforming the corrected station data and then cross-multiplying (X) it, hence the name of FX-style correlator (Fig. 3.3). The opposite procedure can be also implemented - convoluting the times series for each baseline and then Fourier transform the result - which is known as the XF-style correlators. For more details on the XF correlators and the functional differences between these two types of correlators refer to Romney [32].

In its current status, the SFXC operates as a general purpose VLBI correlator for astronomy and space science, which accepts Mark-4, VLBA and Mark-5A/B/C input data, and is capable of supporting both far field and near field delay models, which is essential for PRIDE experiments. The default far-field delay model used in SFXC is the CALC 10 software [3] developed at the Goddard Space Flight Center, but SFXC allows the input of other models supplied by the user. The output of the correlation is provided in so-called $aips++$ measurement sets. Subsequently, the measurement

[3] http://gemini.gsfc.nasa.gov/solve/

sets are transformed into FITS[4] files, for further standard VLBI post-processing and analysis with different software packages.

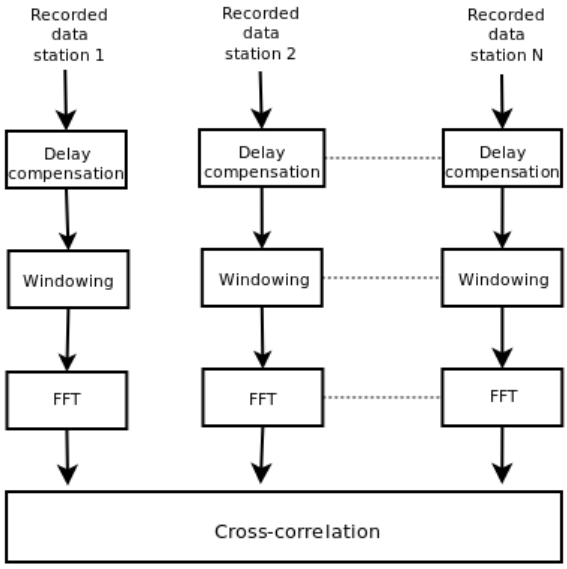

Figure 3.3: SFXC correlator data flow. Credit: Keimpema et al. [21]

3.2.6. Delay models

As explained in Sections 2.1.2 and 3.2.1, it is essential for the correlator to use an appropriate total delay model in order to remove the effects of all the different delay contributions present in the signal. Besides the geometrical delay, there are other delays present in the recorded signals, due to the propagation through the ionosphere and atmosphere, the antenna geometry and deformation, and through the electronics at each receiving system. The antenna related contributions due to axis offsets, and thermal and gravitation deformations, are modeled as explained by Nothnagel [28], Sarti et al. [33] and Clark & Thomsen [6]. The delay introduced by the electronics of the system is calibrated after correlation during the broadband data post-processing, as explained in Section 3.3. The models used to calculate the geometrical delays and delays due to propagation effects will be presented in this section. These models have been implemented in the software package *pypride* (PYthon tools for PRIDE) developed at JIVE.

Geometric delay

The far field model, also known as the *consensus model* [14], is used to determine the time difference in signal arrival between two ground stations for an emitting radio source located at an infinite distance from Earth (for instance, quasars, which are extragalactic sources, can be assumed to be at an infinite distance). In this case, the wave front arriving at the telescopes can be assumed to be planar. However,

[4]FITS is a binary format standard for astronomical data

this assumption does not hold when observing radio sources at finite distances. As explained by Born & Wolf [4], following Fraunhofer's criterion, an incoming radio wave is considered to be in the near field if the distance to the source is $R \leq D^2/\lambda$ from the telescope's aperture, where D is the characteristic aperture size and λ the radio wavelength. Therefore, even when choosing short baselines, (*e.g.,* a VLBI array with a synthesized aperture of 1000 km), an incoming wave front from a spacecraft transmitting at X-band should be considered to be curved, since for this case $R \lesssim 200$ AU. If a near field model is not used for these cases, this will amount for a delay error in the order of microseconds.

The VLBI delay model is formulated in the Barycentric Celestial Reference System (BCRS)(a space–fixed system, whose origin is the center of the mass of the Solar system, and its inclination is equatorial), therefore, there are a number of time-scale and station coordinates transformations required in order to derive this model. In VLBI observations the recorded signals are measured in proper time by the station clocks, which are synchronized to the Coordinated Universal Time (UTC). The coordinates of the calibrator sources are given by the ICRF catalog which are defined in BCRS. The spacecraft ephemerides are obtained from SPICE kernels, for which a realization of the BCRS is adopted to output the spacecraft coordinates. On the other hand, the VLBI antennas' coordinates are defined in the International Terrestrial Reference System (ITRS) (an Earth–fixed system, whose origin is the center of the mass of the Earth). Therefore, in order to derive the VLBI delay model, for both, the far- and the near-field case, the station coordinates should be transformed from ITRS to BCRS, and the measurement timing at each station should be transformed from UTC to Barycentric Dynamical Time (TDB). TDB is the time-scale used in the ephemerides of planetary spacecraft and Solar System bodies. It is a scaled version of the Barycentric Coordinate Time (TCB), which is the time coordinate of the BCRS space-time metric. All the above mentioned transformations should be carried out according to the latest recommendations of the International Earth Rotation Service (IERS) [29].

- **Plane wave approximation**

  In the BCRS, the vacuum geometric delay according to the consensus model is given by,

$$T_j - T_i = -\frac{\hat{\mathbf{k}}}{c} \cdot (\mathbf{R}_j(T_j) - \mathbf{R}_i(T_i)) + \Delta T_{\text{grav}} \tag{3.12}$$

  where T_i and T_j are the reception times in TDB at the stations i and j, respectively, $\mathbf{R}_i$ and $\mathbf{R}_j$ are the position vectors of stations i and j with respect to the Solar System Barycenter (SSB) in BCRS, respectively, $\hat{\mathbf{k}}$ is the unit vector from the SSB to the radio source (in absence of gravitational or aberrational bending) and ΔT_{grav} is the general relativistic delay.

  Then, the total barycentric vacuum delay given in Equation 3.12 is converted to geocentric delay, applying the Lorentz transformations as explained by Sovers & Jacobs [38]:

$$t_j - t_i = \frac{\Delta T_{\text{grav}} - \frac{\hat{\mathbf{k}}\cdot\mathbf{b}}{c}\cdot\left[1 - \frac{(1+\gamma)U_{\text{E}}}{c^2} - \frac{V_{\text{E}}^2}{2c^2} - \frac{\mathbf{V}_{\text{E}}\cdot\hat{\mathbf{r}}_{\text{j,gc}}}{c^2}\right] - \frac{\mathbf{V}_{\text{E}}\cdot\mathbf{b}}{c^2}\cdot\left(1 + \frac{\hat{\mathbf{k}}\cdot\mathbf{V}_{\text{E}}}{2c}\right)}{1 + \frac{\hat{\mathbf{k}}\cdot(\mathbf{V}_{\text{E}}+\hat{\mathbf{r}}_{\text{j,gc}})}{c}} \quad (3.13)$$

where t_i and t_j are the reception times in Geocentric Coordinate Time (TCG) at stations i and j, respectively, $\mathbf{b} = \mathbf{r}_j(t_i) - \mathbf{r}_i(t_i)$ is the baseline vector in Geocentric Celestial Reference System (GCRS) at t_i with respect to geocenter, $\hat{\mathbf{r}}_{\text{j,gc}}$ is the velocity vector in GCRS of station j with respect to geocenter, $\mathbf{V}_{\text{E}}$ is the Earth velocity vector in BCRS with respect to SSB, γ is the PPN parameter (equal to 1 in general relativity) and U_{E} is the summation of the Newtonian potentials of all major bodies of the Solar system excluding the Earth evaluated at geocenter: $U_{\text{E}} = \sum_{p\neq q}\frac{GM_p}{r_{\text{E}q}}$. The total gravitational delay ΔT_{grav} is obtained summing the individual contributions of the major bodies in the Solar System, including the Earth,

$$\Delta T_{\text{grav}} = \sum_N \Delta T_{\text{grav},N} \quad (3.14)$$

where $\Delta T_{\text{grav},N}$ is the general relativistic delay due to the presence of the N_{th} body:

$$\Delta T_{\text{grav},N} = 2\frac{GM_N}{c^3}\ln\frac{R_{iN} + \hat{\mathbf{k}}\cdot\mathbf{R}_{iN}}{R_{jN} + \hat{\mathbf{k}}\cdot\mathbf{R}_{jN}} \quad (3.15)$$

where,

$$\mathbf{R}_{iN} = \mathbf{R}_{iN}(t_i) = \mathbf{R}_i(t_i) - \mathbf{R}_N(t_{iN})$$

and,

$$\mathbf{R}_{jN} = \mathbf{R}_{jN}(t_i) = \mathbf{R}_j(t_i) - \frac{\mathbf{V}_{\text{E}}}{c}(\hat{\mathbf{k}}\cdot\mathbf{b}) - \mathbf{R}_N(t_{iN})$$

where t_{iN} is the moment of closest approach of the photon to the gravitating body N in TCG.

- **Curved wave front**

  Different approaches have been use to develop near-field VLBI delay models, among them are Klioner, S. A. [23], Fukushima [17], Sovers et al. [39], Moyer [27] and Sekido & Fukushima [37]. For PRIDE experiments a near-field model has been developed [10, 12], which allows a simple integration of the near field delay model into the SFXC operational environment.

  Figure 3.4 shows the geometry of VLBI observations of a spacecraft in the Barycentric Celestial Reference Frame (BCRF). As shown in this figure, the signal delay is given by the difference between the light-times LT_i and LT_j, from the source to the stations i and j, respectively, in TDB. The signal reception time T_i is known, therefore the spacecraft transmission time T_0 is to be estimated by iteratively solving the light-time equation,

$$LT_i = \frac{R_{0i}}{c} + RLT_{0i} \quad (3.16)$$

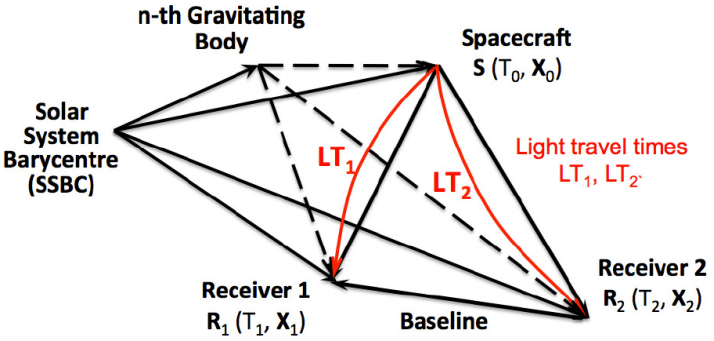

Figure 3.4: Geometry of VLBI observations of spacecraft in the BCRF. Credit: Dmitry Duev.

where $\mathbf{R}_{0i} = \mathbf{R}_i(T_i) - \mathbf{R}_0(T_0)$, where $\mathbf{R}_0$ is the spacecraft position vector with respect to SSB in BCRS, and RLT_{0i} is the relativistic term, accounting for both the special and the general relativity effects, as derived in Moyer [27](Equation 8.55), retaining the terms in each component of the n-body metric tensor to order $1/c^2$ only:

$$RLT_{0i} = \frac{(1+\gamma)\cdot GM_{\mathrm{S}}}{c^3}\cdot \ln\frac{R_0^{\mathrm{S}} + R_i^{\mathrm{S}} + R_{0i}^{\mathrm{S}} + \frac{(1+\gamma)\cdot GM_{\mathrm{S}}}{c^2}}{R_0^{\mathrm{S}} + R_i^{\mathrm{S}} - R_{0i}^{\mathrm{S}} + \frac{(1+\gamma)\cdot GM_{\mathrm{S}}}{c^2}} + \sum_{B=1}^{10}\frac{(1+\gamma)\cdot GM_B}{c^3}\cdot \ln\frac{R_0^B + R_i^B + R_{0i}^B}{R_0^B + R_i^B - R_{0i}^B} \tag{3.17}$$

where the subscript S denotes the Sun and the subscript B denotes a specific body in Solar System, the summation includes the planets, Pluto and the Moon, and $\mathbf{R}_0^\alpha = \mathbf{R}_0(T_0) - \mathbf{R}_\alpha(T_0)$, $\mathbf{R}_i^\alpha = \mathbf{R}_i(T_i) - \mathbf{R}_\alpha(T_i)$, and $\mathbf{R}_{0i}^\alpha = \mathbf{R}_i^\alpha(T_i) - \mathbf{R}_0^\alpha(T_0)$ for $\alpha = S, B$.

At each iteration step, the correction ΔT_0 to the estimate of T_0 is given by,

$$\Delta T_0 = \frac{T_i - T_0 - R_{0i} - RLT_{0\mathrm{i}}}{1 - \dot{p}_{0\mathrm{i}}/c}, \tag{3.18}$$

where,

$$\dot{p}_{01} = \frac{\mathbf{R}_{0i}}{R_{0i}}\cdot\dot{\mathbf{R}}_0(T_0) \tag{3.19}$$

The procedure described above is repeated to solve for LT_j.

The difference $T_j - T_i = LT_j - LT_i$ is the VLBI signal delay in TDB. In order to obtain this VLBI near-field delay in the geocentric Terrestrial Time (TT) frame, the following conversion is applied:

$$t_j - t_i = \frac{\frac{T_j - T_i}{1-L_C}\cdot\left[1 - \frac{1}{c^2}\left(\frac{V_{\mathrm{E}}^2}{2} + U_{\mathrm{E}}\right)\right] - \frac{\mathbf{V}_{\mathrm{E}}\cdot\mathbf{b}}{c^2}}{1 + \frac{\mathbf{V}_{\mathrm{E}}\cdot\dot{\mathbf{r}}_{\mathrm{j,gc}}}{c^2}} \tag{3.20}$$

where $L_C = 1.48082686741 \times 10^{-8}$ [20] is the general relativistic scale factor of the Earth. Equation 3.20 is the equivalent of Equation 3.13 for the case of a curved wave front.

Delay due to propagation effects

The transmitted signal from the source propagates through different media before it is received at the Earth-based antennas: the interplanetary plasma, and the ionosphere and troposphere of the Earth. Therefore, the impact that the radio waves propagation has on the signal delay has to be modeled.

- **Propagation through the interplanetary medium**

  The variations in the flux density of a radio wave being propagated across the Solar System are dominated by the Interplanetary Scintillation (IPS) present in the Solar wind. The scintillations are due to the electron density variations of the Solar wind, which is an ionized plasma. The turbulence generated as the Solar wind expands radially outwards in the heliosphere can be modeled as a hydrodynamic turbulence as described by Kolmogorov [24]. In Molera-Calvés et al. [26], it was demonstrated that using the narrowband processing of the spacecraft signal (see Section 3.4), the phase scintillation can be directly derived from the phase fluctuations of the spacecraft signal. To estimate the variance of the phase fluctuations, the spectral power density for each of the scans is computed, and then averaged over an entire observing session. Subsequently, the spectral index m - the slope of the averaged spectral power density - is determined. Then, the phase scintillation index, σ_{sc}, is determined as follows:

$$\sigma_{sc} = \left[-\frac{D(f_0) \cdot f_0}{m+1} \right]^{\frac{m+1}{2}} \tag{3.21}$$

  where $D(f_0)$ is the spectral power density, $f_0 = 1/\tau$ is the cut-off frequency of the spectrum, with τ being the length of the phase referencing nodding cycle. The phase scintillation index is defined as the standard deviation of the phase fluctuations caused by the interplanetary plasma within the scintillation band. When using the phase-referencing technique the shorter the nodding cycle is, the better the target phase can be calibrated.

- **Propagation through the Earth's ionosphere**

  The signal delay due to the Earth's ionosphere is derived using the ionosphere maps, given in an Earth-fixed reference frame, provided by the International GNSS Service (IGS)[15]. The vertical Total Electrical Content (vTEC) maps, are "snapshots" of the ionosphere produced every 2 hours on a daily basis on a global grid, using raw Global Navigation Satellite System (GNSS) data measurements. For details on how these vTEC maps are generated and how the data is formatted refer to Hernández-Pajares et al. [19] and Schaer et al. [34]. As shown in Figure 3.5 the map is generated approximating the ionosphere to a single thin layer at a given height H. When calculating the delay, the vTEC needs to be mapped onto the direction of the target to properly get the electron content integrated along the slant path of the signal from the target to the receiver. By calculating the corresponding pierce point in the model's thin

ionosphere layer and applying the necessary grid interpolations (in latitude, longitude and time) of the concerning vTEC map, the vTEC value for each time step during the observation can be derived. The slant Total Electrical Content (sTEC) is then derived using the following relation,

$$sTEC = \frac{vTEC}{\cos z'}, \tag{3.22}$$

where z' is the angle between the zenith and the target as seen from the model's ionospheric layer:

$$z' = \arcsin \frac{R}{R+H} \cdot \sin z, \tag{3.23}$$

where R is the mean radius of the Earth, H is the height of the ionospheric layer and z is the angle between the zenith and the target as seen from the receiver, assuming a vacuum condition.

The ionospheric delay, for each station at each time step, can be then computed as,

$$\tau_{\text{iono}} = \frac{e^2 \cdot sTEC}{8cm_e\epsilon_0\pi^2 \cdot f^2}, \tag{3.24}$$

where f is the observational frequency, c is the speed of light in vacuum, m_e is the electron mass, ϵ_0 is the permittivity of free space and e is the elementary charge.

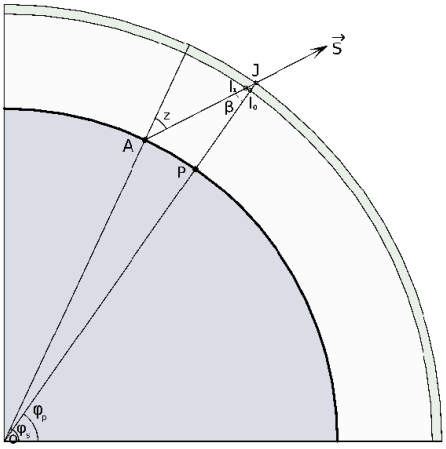

Figure 3.5: Thin layer model of the ionosphere to calculate the ionospheric delay. Credit: Duev et al. [12]

- **Propagation through the troposphere**

  The propagation of the signal in the neutral atmosphere is dependent of the medium's refractivity dependence on height and geographical coordinates. Therefore, the tropospheric path delay is computed numerically using empirical data regarding the global partial refractivity distribution. The tropospheric delay,

which is dependent on the antenna pointing's azimuth and elevation, is usually described as the sum of two terms, the hydrostatic or 'dry' slant delay component τ_h, and the non-hydrostatic or 'wet' slant delay component τ_w [8]:

$$\tau_{tr} = \tau_h + \tau_d \tag{3.25}$$

Furthermore, in the modeling of the tropospheric delay a difference is made between the azimuthally symmetric delay and the azimuthally asymmetric delay, where the later is determined by modeling the horizontal tropospheric gradient [35].

$$\begin{aligned}\tau_{tr} &= \tau_{h,symm} + \tau_{h,asymm} + \tau_{w,symm} + \tau_{w,asymm} \\ &= \tau_h^z mf_h(e) + mf_{AZ,h}(e)(G_{N,h}\cos\alpha + G_{E,h}\sin\alpha) \\ &+ \tau_w^z mf_w(e) + mf_{AZ,w}(e)(G_{N,w}\cos\alpha + G_{E,w}\sin\alpha) \\ &\simeq \tau_h^z mf_h(e) + \tau_w^z mf_w(e) + mf_{AZ}(e)(G_N\cos\alpha + G_E\sin\alpha)\end{aligned} \tag{3.26}$$

where τ_h^z is the hydrostatic zenith delay, τ_w^z is the wet zenith delay, mf_{AZ} is the mapping function, where e is the elevation above the horizon and α is the azimuth of the source, and G_N and G_E are the gradients in the North and East direction, respectively. In order to calculate τ_{tr}, the goal is then to properly derive the zenith delay and the mapping function. One approach is to make use of the empirical Vienna Mapping Functions (VMF1) data [3] produced by the Global Geodetic Observing System (GGOS) Atmosphere project, where the hydrostatic and wet zenith delays, and the coefficients of the mapping function - needed to map the delays from the local zenith onto the direction of the source - are provided on a global grid every 6 hours. The derivation of the mapping function coefficients relies on the method of ray-tracing through Numerical Weather Models (NMW) of the European Centre for Medium-Range Weather Forecasts (ECMWF). The practical implementation of the gridded VMF1 data in order to derive the tropospheric delay is explained in detail in Kouba [25].

3.3. Broadband reference source signal processing

The goal of the calibrator broadband data processing and analysis for PRIDE experiments, is to derive the delay residuals, delay rate and phase corrections for each telescope of the reference natural source data, and use them to calibrate the spacecraft visibility data. To apply this so-called phase-referencing technique, it is desirable to use calibrator sources that are compact (*i.e.,* point-like) extragalactic sources, such as quasars, whose absolute coordinates are accurately known to the level of $\sim$ 0.1 mas[5].

The processing pipeline starts with the broadband raw data correlation of the calibrator source, implemented with the SFXC correlator, using the far-field model described in Section 3.2.6. The inputs to the correlation step are the a priori J2000 coordinates of the reference source, the modeled VLBI delay for the far field observations and the formatted raw data of the calibrator scans. The VLBI delay model used

[5]Suitable calibrators can be chosen from the latest VLBI calibrators' catalog available at http://astrogeo.org/calib/search.html

by the correlator will inevitably contain some residual phase error. This phase error will be a summation of different sources of errors, such as errors in the position of the target and the antenna, errors in the Earth model, instrumental errors, atmospheric and ionospheric errors, and errors in the clock epoch and clock rate at each antenna.

In conventional VLBI imaging the estimation and removal of the effects of delays and delay-rates errors is done using the process known as *fringe fitting*. After these effects are removed, the phase estimation is improved using a well-documented iterative process of self-calibration and imaging [5, 7, 31, 40]. However, with this procedure, where the target source itself is used to estimate the phase errors, the information regarding the absolute position of the source is lost given the fact that the above-mentioned parameters are estimated assuming they are antenna-based errors.

Therefore, an angularly nearby source to the main target is used instead to calibrate the phase data. The delay, delay-rate and phase errors from the reference source observations are estimated by fringe-fitting, self-calibration and imaging. In this case, the loss of the position-related information is irrelevant, due to the a priori precise knowledge of the calibrator's absolute coordinates. The retrieved corrections are then applied to the target visibility data, and since both, the target and calibrator, are "angularly close" to each other, the phase errors common to both observations will be (ideally) removed. In this way, the only phase error remaining in the target data is due to the difference between the measured spacecraft angular position and the predicted position, derived with the a priori spacecraft orbit used for the near-field delay model. This last step will be described in Section 3.6. The description on how the calibration phase parameters, per antenna-basis, are derived from the reference source's raw data is described in this section.

In the interferometer receiving system the input signal is related to the output signal through a transfer function, which includes all the effects the receiving system imposes on the true incoming signal. Hence, the process of calibration basically consists in the proper calculation of transfer function parameters, so that the true input values can be estimated from the observed data. The visibilities $\tilde{V}$ measured with the interferometer on the baseline $i-j$ can be expressed as the product of true visibilities V and antenna complex gains g of each element i and j,

$$\tilde{V}_{ij}(\nu,t) = g_i(\nu,t)g_j(\nu,t)V_{ij}(\nu,t) \tag{3.27}$$

Consequently, in order to obtain the true visibilities, the amplitude and phase terms of the antenna complex gains have to be properly estimated. The complex gains $g(\nu,t)$ can be split in two terms, the bandpass characteristic and frequency dependent terms $B(\nu)$, and the time dependent term $G(t)$, as follows:

$$g(\nu,t) = B(\nu)\cdot G(t)$$

Section 3.3.1 describes how these terms, $B(\nu)$ and $G(t)$, are estimated in order to retrieve the true visibilities $V_{ij}(\nu,t)$.

3.3.1. Data Processing Path in AIPS

The results of the broadband data correlation with SFXC are written in FITS files which are then imported into Astronomical Image Processing System (AIPS)[6]. This section summarizes the necessary steps to be taken to generate the calibration phase parameters from the point-like continuum source data.

AIPS provides a cluster of programs for data reduction that are known as 'tasks'. The tasks will produce different tables, among which, the solution tables which contain the gain solutions ($B(\nu)$ or $G(t)$) from specific calibration routines. Using the task 'FITLD' multiple disk files in FITS format can be imported to start the data processing.

- **Examining data:** The imported data has to be examined to identify corrupted data due to possible problems during the observation, for instance, Radio Frequency Interference (RFI), instrumental failure or serious propagation effects. The incorrect visibilities that cannot be calibrated should be removed, with a process known as flagging. The flagging procedure can be automated or performed manually following certain criteria, as explained in Ekers [13].

- **Calibration of Instrumental Delays:** When the uncalibrated cross-power spectra are plotted for each individual IF channel, the phase offsets and phase gradient against frequency will not agree between the channels. These offsets are caused by the passage of the signal through the electronics of the baseband converters. Usually a narrowband signal with well-known characteristics is injected at each antenna, and recorded along with the observation data. These so called 'phase-cals' measurements, are subsequently used to determine and remove the IF channel phase offsets, and single-band instrumental delay, induced by the electronics. The phase-cals measurements are incorporated in a solution table with the task 'PCCOR'.

- **Amplitude Calibration:**

  The calibration of the interferometer output amplitude, to obtain the true visibility amplitude, requires the conversion of the output data from the correlator (cross-power spectrum S_{ij}) into the source flux density (in Jy units) by using the system noise temperature (T_{sys}) and the antenna gain information. The relation between the visibility amplitude an the cross correlation coefficient can be written as follows,

$$|V_{ij}| = \left(2k_B \sqrt{\frac{T_{sys,i} T_{sys,j}}{A_{e,i} A_{e,j}}} \right) S_{ij} \tag{3.28}$$

  where k_B is the Boltzmann constant, T_{sys} is the system noise temperature and A_e is the antenna effective aperture area. The factor by which S_{ij} is multiplied within Equation 3.28 is the square root of the System Equivalent Flux Density (SEFD) of each antenna i, which is used as measure of the antenna's system performance,

[6] AIPS is a software package developed by the National Radio Astronomy Observatory (NRAO) (Virginia, USA) for interactive calibration and editing of radio interferometric data, and construction and analysis of images from those data using Fourier synthesis methods. URL: http://www.aips.nrao.edu/.

$$\mathrm{SEFD}_i = \frac{2k_B T_{sys,i}}{A_{e,i}} \tag{3.29}$$

The amplitude calibration is then performed calculating the SEFD values for each antenna based on the so-called ANTAB (ANtenna TABle) file, provided by each station operator, which contains the system temperature and gain curve of each antenna throughout the observation. This procedure is carried out in AIPS, with the tasks 'ANTAB' and 'APCAL', the former will import the system temperature and gain curve of each antenna, and the latter will apply them and generate a solution table.

- **Bandpass calibration:** The effect of the bandpass filter on the cross correlation amplitude is calibrated using the task 'BPASS'. Even if the data being reduced is that of a continuum source, by applying the bandpass calibration the dynamic range of the observations can be improved.

- **Phase Calibration: Fringe Fitting**

  The phases of the visibilities reflect the positions of radio sources, therefore, it is important that the visibility phases are properly calibrated in order to allow the correct estimation of position and structure of the source. The visibility phases should be almost constant to be able to integrate visibilities coherently - which is necessary to improve the SNR - but if time variations are present in the visibilities, the amplitude of the visibilities decreases because of coherence loss. For instance, if the visibility phases are shifted by ϕ with respect to the true values, the effective visibility value would be $V\cos\phi$. In this case, assuming that the probability density distribution of phases $p(\phi)$ is a Gaussian distribution with standard deviation σ, the visibility amplitude would result in,

$$\langle V\rangle = \int_{-\infty}^{\infty} V\cos\phi\, p(\phi)d\phi = \int_{-\infty}^{\infty} V\cos\phi\,\frac{1}{\sigma\sqrt{2\pi}}e^{-\frac{\phi^2}{2\sigma^2}}d\sigma = Ve^{-\frac{\sigma^2}{2}} \tag{3.30}$$

  This means that, for example, a standard deviation of ~ 1 rad will account for a 40% of amplitude decrease. The operation that flattens out the visibility phases by calibrating delay residuals and time residuals of delay residuals is known as *fringe fitting*.

  At this point, after removing the instrumental delays, the remaining delays residuals after the correlation process are caused by clock offsets at antennas, station positioning errors and atmosphere effects. The phase shift is a function of these delay residuals $\Delta\tau$,

$$\Phi = 2\pi\nu\Delta\tau \tag{3.31}$$

  which is in turn a function of time and can be expressed as,

$$\Delta\tau = \Delta\tau_0 + \Delta\dot{\tau}(t - t_0) \tag{3.32}$$

  where $\Delta\dot{\tau}$ is the time derivative of delay residuals. Thus, the phase becomes,

$$\Phi = 2\pi\nu[\Delta\tau_0 + \Delta\dot{\tau}(t - t_0)] \tag{3.33}$$

To calibrate the delay residuals and the corresponding time derivatives, the integration of visibilities in the $(\Delta\tau_0, \Delta\dot{\tau})$ domain is evaluated and the values of $(\Delta\tau_0, \Delta\dot{\tau})$ for which the visibility amplitudes are maximized are determined. This process is called *fringe search*. In AIPS, the data is fringe-fitted using a global fringe search method [36]. AIPS provides the task 'FRING' which applies the global fringe search method. The estimated delay residuals and their time derivatives are stored in a solution table, which will be used at a later step for the phase-referencing procedure of the spacecraft signal. After fringe fitting, the visibilities can be integrated coherently. The calibrated spectrum should be plotted to check whether the phases have been correctly calibrated.

- **Frequency integration:** Once the results of the above-mentioned VLBI calibration steps are satisfactory, the gains stored in the solution tables are applied to the data with the task 'CLCAL'. At this point, all the spectral channels and IFs can be averaged to produce a data set with one channel per polarization. In this process, the calibration table produced by the application of all the solution tables to the original data is used. The visibilities are then integrated in the frequency direction, and the output are the calibrated visibilities, which can be used to produce an image of the source.

- **Imaging**

  In Section 2.1.2 it was shown that an image of the source observed with an interferometer could be produced by simply applying the Fourier transform on the measured visibilities. At this point the visibilities have been calibrated, however, a real interferometer samples the visibilities in an irregular and incomplete fashion, as shown in Figure 3.6. For this reason, a technique called *hybrid mapping* is used [7, 31]. Hybrid mapping is an imaging method which solves simultaneously for both the radio source image and the calibration parameters of the antennas. The procedure consists in first assuming some calibration parameters to produce a deconvolved image, and then to use the image to improve the calibration parameters.

  As shown in Equation 2.14 an interferometer measures the visibility function,

$$V(u,v) = \int\int \mathcal{A}(x,y) I(x,y) e^{[-2i\pi(ux+vy)]} \tag{3.34}$$

  where $\mathcal{A}(x,y)$ is the normalized antenna power pattern and $I(x,y)$ is the source intensity distribution. The imaging process consists of retrieving the intensity distribution $I(x,y)$ in the best way possible. Since equation 3.34 is a convolution, the imaging process needs to use deconvolution techniques. Let us define $I_w(x,y)$ as,

$$I_w(x,y) = \int\int S(u,v) W(u,v) V(u,v) e^{[2i\pi(ux+vy)]} du dv \tag{3.35}$$

  where $S(u,v)$ is the spectral sensitivity function containing information on the relative weights of each visibility (derived from system temperature, antenna

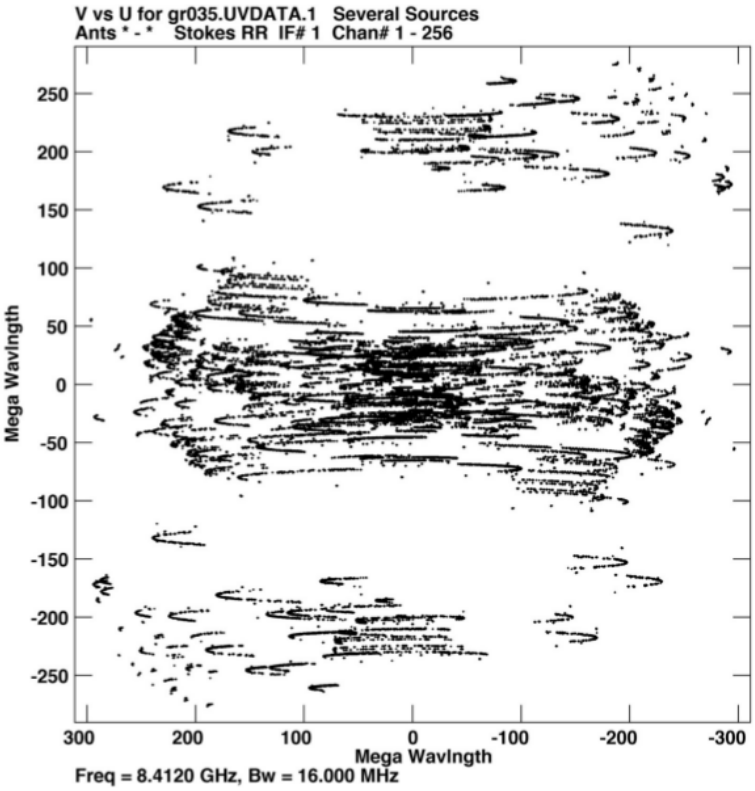

Figure 3.6: Example of the uv-coverage of observations with the EVN plus VLBA [11]. The plot shows the so-called uv-coverage (the axes u and v are defined in Section 2.1.2) which indicates the spatial sampling of the source brightness distribution given by the interferometric baselines. As the signal is recorded, the baselines rotate with respect to the sky as a function of time, "filling in" the image. The more baselines and the longer duration of the observations the better the coverage. The uv-coverage can be understood as a mask on the Fourier transform of the image, showing where on the Fourier plane the image has been sampled.

efficiency, integration time and bandwidth) and $W(u,v)$ is a weighting function (natural or uniform weighting function). Taking into account that the Fourier transform of a product of two functions is the convolution of the Fourier transform of the functions, $I_w(x,y)$ can be expressed as,

$$I_w(x,y) = (A(x,y)I(x,y)) * *(D_w(x,y)) \tag{3.36}$$

where the double asterisk indicates two-dimensional convolution, and,

$$D_w(x,y) = \int\int S(u,v)W(u,v)e^{[2i\pi(ux+vy)]}dudv = \widetilde{SW} \tag{3.37}$$

where $D_w(x,y)$ is known as the *dirty beam*, and $I_w(x,y)$ is known as the *dirty image*.

In brief, these equations show the mechanism behind the imaging process; a Fourier transform is required to derive the I_w from the measured visibilities and spectral sensitivity function, and deconvolution is needed to retrieve the source intensity distribution I from I_w. As previously mentioned, the hybrid mapping is an iterative procedure that alternates between self-calibration and image deconvolution. In this process, an image is produced in AIPS by subtracting CLEAN components from the dirty image. The imaging procedure can be summarized as follows:

1. Generate a starting model

   The imaging process starts by applying a primary self-calibration to the input (u,v) data (with the task 'CALIB'), correcting only for the antenna phases. Then, the input model is chosen to be a point-like source model, from which an initial dirty map is generated, with the task 'IMAGR'.

2. Running the CLEAN algorithm

   The CLEAN deconvolution algorithm [5] is shown the block diagram in Figure 3.7.

   In AIPS the CLEAN operation is carried out with the task 'IMAGR'. Among the parameters to define are: the maximum number of CLEAN iterations, the CLEAN loop gain, which sets the fraction of the peak (absolute) residual that is subtracted on each CLEAN iteration (usually is assigned between 0 to 1), and the cutoff value (in Jy), with respect to which the CLEANing will stop if the maximum absolute residual falls to this value or lower. After each CLEAN iteration, the total flux 'cleaned' will corresponds to the sum of the flux densities of all CLEANed components up to the current step. The CLEANing procedure should in principle continue until the total flux cleaned becomes the total flux density of the observed sources.

   As for the data weighting for each visibility point, there are two options: to choose for natural weighting, where all visibilities have equal weight, or to choose for uniform weighting, where the density weight on the (u,v) coverage is inversely proportional to the density of sample points. For VLBI, there is often a wide range of antenna sensitivities (due to the wide range of antenna sizes and receivers quality), which in turn, leads to a wide

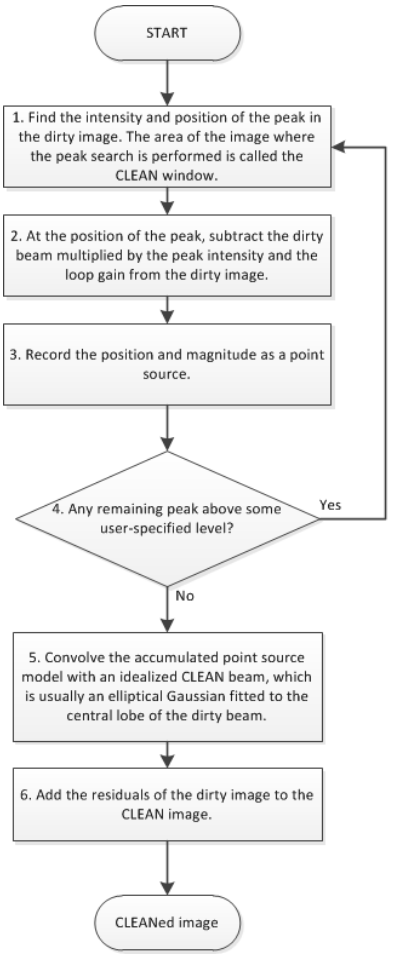

(a) Schematic diagram of the CLEAN algorithm.

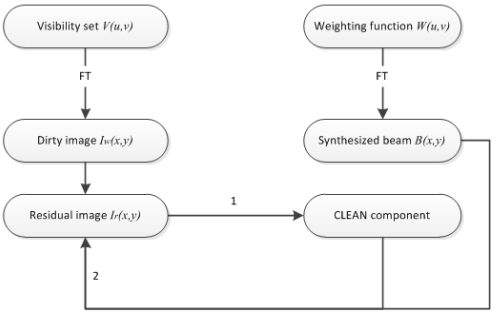

(b) Diagram of objects generated during the hybrid mapping process, where the products of steps 1 and 2 of the CLEAN algorithm are shown.

Figure 3.7

range of weights available for the individual data points. Usually, during the first couple of iterations, when the calibration is poor, it is best to have nearly equal weights on all baselines. In this way, the best advantage is taken from the (u, v) coverage, allowing weak baselines to help the process converge. When the calibration improves, the weights can be adjusted according to the antennas sensitivities. Otherwise, if the natural weights are kept the noise limit will be determined by the weak baselines, possibly limiting the quality of the final image.

After a number of CLEAN iterations the procedure will stop having visible improvements on the output image. At this point, the dynamic range of the map should be improved with self-calibration.

3. Self-calibration of phase and amplitude

   The method of self-calibration is used to calibrate the remaining errors of the amplitude and phase components of the antenna gain. The idea behind the self-calibration algorithm is to minimize the differences between the observed visibilities and the model visibilities, which are theoretically calculated. The residual is minimized by adjusting the antenna gain values in the model visibilities in an iterative process. The solution of the self-calibration will be the set of antenna gains that lead to the minimum residuals of the difference of the models. Subsequently, the imaging procedure can start again, this time using the new solution given by the self-calibration. By alternating between CLEAN and self-calibration for a certain number of times, the obtained solution should converge to the true brightness distribution.

   The self-calibration operation can solve amplitude components and phase components either separately or simultaneously. Usually, the phase components are calibrated first, and then both the phase and amplitude components simultaneously.

   When the process converges, the final map (CLEANed map) is obtained.

The final map of the calibrator sources should be examined to corroborate whether the amplitude and phase calibration solutions have been correctly determined; by obtaining a point-like source image and by comparing it with the images presented in VLBI calibrator catalogs (for instance, the VLBA calibrator list). Values such as peak brightness should be comparable to the catalog images, taking into account the size of the synthesized beam.

The output of the broadband processing of the calibrator data, within the PRIDE pipeline, are the delay and phase corrections derived in the process of obtaining the calibrator image: the group delay and delay-rate residuals estimated by means of the fringe-fitting technique, and the phase errors extracted from the self-calibration process.

3.4. Narrowband spacecraft signal processing

The first step in the narrowband data processing part of the pipeline is to retrieve the topocentric Doppler detections from the single dish open-loop data collected by

each of the participating stations. The software used to process these data is the SWSpec/SCtracker/DPLL package, developed between Metsähovi Radio Observatory (MRO) and JIVE.

3.4.1. Software spectrometer (SWSpec)

In PRIDE experiments, multiple wide sub-bands (typically 8 or 16 MHz) are necessary for a successful detection of the phase-referencing background radio source calibrators, while the spacecraft signal itself can be represented in a band of several kHz (taking into account the range of possible Doppler shifts). Therefore, the initial step for the spacecraft signal processing is to extract from the Mark-5 data the channel corresponding to the sub-band containing the spacecraft signal. Since the nominal frequency of the spacecraft is known, the channel where the spacecraft carrier signal is expected to have been recorded is known. Subsequently, a Window-OverLapped Add (WOLA) Discrete Fourier Transform (DTF) is applied on the data extracted and a time integration over the obtained spectra is performed. This procedure is carried out using the high resolution software spectrometer SWSpec [43], which allows the initial detection of the spacecraft carrier and sub-ranging tones, and the temporal evolution of their frequencies throughout the scans. This software, which was developed at MRO, supports different input formats; from raw data to formatted data like Mark-5A/B/C (developed by Haystack/MIT), PC-EVN (developed by Metsähovi/Aalto) or the VLBI Data Interchange Format (VDIF) (developed by a collaboration of international institutes).

Figure 3.8 shows a typical spacecraft signal spectrum, consisting of a carrier line with the highest spectral density power, sub-carriers, usually separated by 100 - 200 kHz from the carrier, data band with effective width of 200-500 kHz, and several ranging tones separated by ~ 1 MHz from the carrier and spread over 5-10 MHz, with a power decreasing with the harmonic number.

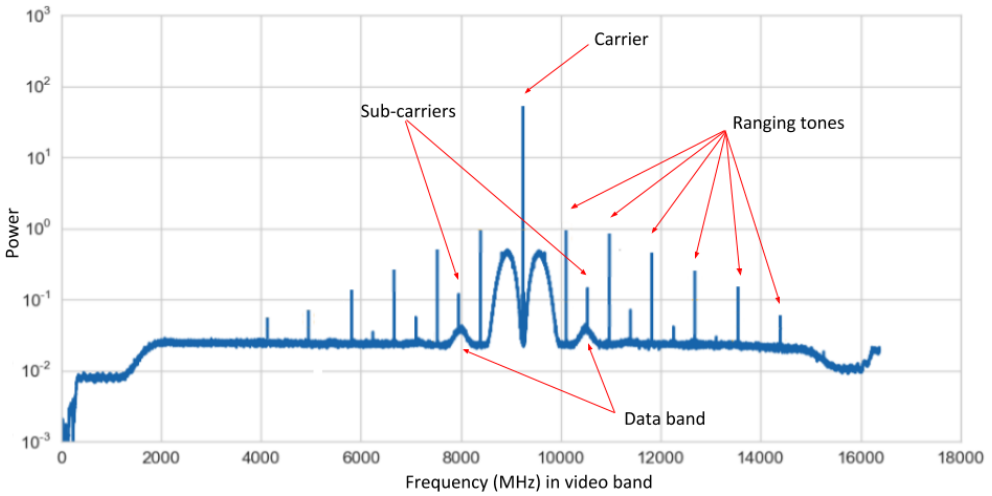

Figure 3.8: Example of the spectrum of a spacecraft signal. This is the power spectrum of ESA's Mars Express spacecraft signal (X-band), obtained during the experiment GR035 (treated in Chapter 4).

Figure 3.9 shows an example of the resulting spectrum after the raw spacecraft signal has been processed with Software Spectrometer (SWSpec).

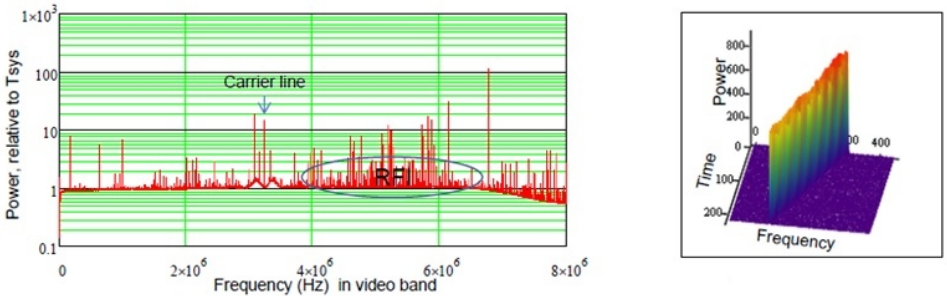

Figure 3.9: Left panel: SWSpec detection 10 Hz resolution over an 8 MHz bandwidth, 19 minutes averaged spectrum. Right panel: temporal evolution of the carrier line spectrum. Both figures correspond to detections with Wettzell station of the Venus Express.

3.4.2. Phase-stop polynomial fit

Using as an input the time-integrated spectra generated by SWSpec, the goal of this step is to determine the frequency drift of the spacecraft detections along the series of spectra. For this purpose, a polynomial fit is used to model the moving phase of the spacecraft carrier tone frequencies (Fig. 3.9, right panel) along the time-integrated spectra per scan. The M-order phase polynomial is estimated using the following relation (in practice, $M = 6$ is usually used):

$$P(t) = 0 + \tilde{C}_{pp}(1) \cdot t + \tilde{C}_{pp}(2) \cdot t^2 + \ldots + \tilde{C}_{pp}(M-1) \cdot t^{M-1} \tag{3.38}$$

where $P(t)$ is the phase polynomial function, $\tilde{C}_{pp}$ are the phase polynomial coefficients to be estimated and t is the elapsed time of the scan. The phase polynomial fit is conducted using the Weighted Least Mean Square (WLMS) method, in which the weights assigned depend on the detection's SNR and the nearby RFI characteristics:

$$(T^T W_{\mathrm{SNR}} T)\tilde{C}_{pp} = T^T W_{\mathrm{SNR}} F \tag{3.39}$$

where the T is the time matrix, F is the frequency matrix and W_{SNR} is the weighted SNR matrix, all representing the data along the entire integrated spectra. The output of this step are the estimates of the phase-stopping polynomial coefficients, $\tilde{C}_{pp}$. They will be used as input to the next processing step: phase stopping and narrow band tone filtering and extraction.

3.4.3. Spacecraft multi-tone tracking

In order to stop the moving phase of the carrier signal and retrieve the Doppler frequency detections of the spacecraft signal the spacecraft multi-tone detection and tracking software (SCtracker) is used. As shown in Figure 3.9, the carrier tone frequency shifts in time as the observation progresses. This Doppler shift is the instantaneous Doppler observable to be retrieved. For this purpose, it is necessary to stop the

moving phase of the carrier tone, and accumulate the corrections (Doppler shift corrections) until the spectral resolution of the carrier tone is within the desired (~mHz) level. The algorithm implemented in SCtracker applies the double-precision polynomial coefficients obtained in the previous step to the baseband sample sequence $x[n]$ in order to stop the carrier tone phase, by means of the following relation:

$$\tilde{x}[n] = x[n]e^{\left(\pm\sum_{k=1}^{M-1}\tilde{C}_{pp}(k)\cdot(T_n)^k\right)} \tag{3.40}$$

where the $\tilde{x}[n]$ are the new samples, the $x[n]$ is the original raw samples and the T_n is the time samples of the spectrum. The resulting time-integrated spectrum is thus corrected for an initial Doppler shift approximation along the corresponding scan, given by the polynomial fit. Subsequently, a narrow band is selected around the spacecraft carrier tone. The selected narrow band is extracted from the stopped baseband signal and then filtered and downconverted, using a 2^{nd} order WOLA Direct Fourier Transform (DFT)-based algorithm of the Hilbert transform approximation. The output of this step is the Doppler-corrected (initial fit) carrier signal in a narrow band of 2 kHz bandwidth (in contrast to the initial 8/16 MHz bandwidth of the channel where it was recorded). The extracted complex time-domain signal is written with complex floating-point precision in an output file.

3.4.4. Digital Phase-Locked Loop

Having extracted the narrow band containing the carrier tone, the remaining residuals resulting from the initial polynomial fit will be corrected for with the Digital Phase-Locked-Loop (DPLL) software, which allows to track the carrier tone at a higher precision along the scan. The DPLL will run high precision iterations from equation 3.38 to 3.40 on the filtered signal. At each iteration, the PLL first calculates a new time-integrated overlapped spectra, then it estimates a new set of phase polynomial fit, and finally it performs the phase stopping of the time-integrated spectra. After each iteration, the output of the DPLL is a new filtered and down-converted signal, with its corresponding residual frequency and phase. The number of iterations is dependent on the desired frequency precision, which is usually in the order of mHz. The output of the DPLL is the filtered down-converted signal and the accumulated residual frequency in the stopped band. The bandwidth of the output detections is 20 Hz with a frequency spectral resolution of 2 mHz. As an indication, when running the DPLL using 20000 FFT points and 10 s integration time on a three-way Doppler detection, a Doppler noise of 2 mHz, at X-band, translates into a range rate random error of $\sim 30\,\mu$m/s . This is the total Doppler noise derived from the data reduction following the PRIDE approach, and gives the uncertainty to which the spacecraft carrier tone frequency is estimated at every sampled point.

3.4.5. Phase delay of the carrier line

After running the DPLL, the topocentric Doppler detections f_{tc} can be obtained by adding the base frequency of the selected channel to the obtained time averaged carrier tone frequencies. Then, each of the topocentric Doppler detections are reduced to geocenter using the following relation:

$$f_{gc,i} = f_{tc,i}(t - \tau_{gc}) \cdot (1 - \dot{\tau}_{gc}) \tag{3.41}$$

where $f_{gc,i}$ is the geocenter frequency detection at the station i, the time t is given in UTC, and τ_{gc} and $\dot{\tau}_{gc}$ are the total near-field VLBI signal delay and delay rate with respect to the geocenter, respectively.

The geocentric phases ϕ_{gc} per station are derived by averaging and integrating the geocentric frequencies for each station. Subsequently, the differential phases per baseline $i-j$ are formed,

$$\phi_{ij} = \phi_{gc,j} - \phi_{gc,i} \tag{3.42}$$

The differenced phases are converted to phase delay using the relation $\tau_{ph} = \phi/f_0$, where f_0 is the observational frequency. This relation can be used provided that the 2π-ambiguity of the phases is resolved. As it will be explained in Section 3.6.2, the group delays derived from the broadband processing of the spacecraft signal are used to resolve this ambiguity.

When forming the cross-correlation spectrum from the spacecraft signals, a frequency smearing effect is present in the spectrum if the difference in the Doppler phase of each of the topocentric detections are not accounted for. For this reason, the previously reduced geocentric phases ϕ_{gc} are used as input for the broadband spacecraft correlation.

3.5. Broadband correlation of the spacecraft signal: group delay estimation

The correlation of spacecraft data is implemented with the SFXC correlator, using the near field model described in Section 3.2.6. The inputs to the correlation step are the a priori J2000 spacecraft state vectors with respect to SSB in TDB, the modeled VLBI delay for the near field observations (*i.e.,* the $uvw-$projections of the baselines as explained in Duev et al. [10]) the broadband spacecraft raw data and the Doppler phase corrections derived from the narrowband processing of the spacecraft data.

The broadband correlation of the spacecraft signal allows the derivation of the group delay τ_{gr}, which will be used to solve the 2π-ambiguity of the phase delay. As shown in Figure 3.8, usually ranging tones (spread around the carrier signal over $\sim 5-10$ MHz) are also transmitted along with the spacecraft carrier signal. These tones, whose phases are directly related to the carrier's phase as they are both generated using the same transmission reference signal, are used to estimate the group delay. After the Doppler phase corrections are applied to the spacecraft data, the correlation is conducted at a very high spectral resolution, due to the fact that these sub-carrier lines are intrinsically narrow. The different spectrum filtration and compression procedures [11] needed to correlate the broadband spacecraft signal have been added to the standard SFXC source code, allowing the user specification of spectral and window filters.

Once the complex cross-correlation functions are obtained, they are corrected for clock and clock-rate offsets, and subsequently smoothed in the frequency domain. For each averaged spectrum, the phase is extracted and fitted by a linear function. The group delay τ_{gr} is derived from the slope of the fitted function:

$$\tau_{gr} = \frac{d\phi_{fit}}{df} \tag{3.43}$$

evaluated at the center of the averaging interval. The cross-correlation spectra are saved in FITS files.

3.6. Phase-referencing and estimation of the spacecraft angular position corrections

In Section 3.3 it is explained the process of the calibrator data reduction in AIPS. The output of this procedure is the CLEANed self-calibrated map of the calibrator source and the corresponding delay, delay-rate and phase corrections that were derived from fringe-fitting and self-calibration of the calibrator's data. To apply phase-referencing, the calibrator residual delays are interpolated and smoothened in time. From this solution estimates of the spacecraft delays are derived, allowing the integration of the spacecraft data over frequency without loss of coherence. For this reason, the observations are done alternating between the calibrator and the target. Once, all the spectral channels and IFs are averaged to a data set per source with one channel, the calibrator phases are interpolated in time. The solution of the interpolation is used to estimate the calibrator phases $\tilde{\phi}_{cal}$ for the times t corresponding to the spacecraft scans. These interpolated calibrator phases can be written as follows,

$$\tilde{\phi}_{cal}(t) = \tilde{\phi}^{cal}_{struc}(t) + \tilde{\phi}^{cal}_{inst}(t) + \tilde{\phi}^{cal}_{pos}(t) + \tilde{\phi}^{cal}_{ant}(t) + \tilde{\phi}^{cal}_{atmo}(t) + \tilde{\phi}^{cal}_{iono}(t) \quad (3.44)$$

and differencing the spacecraft phases and the interpolated calibrator phases,

$$\begin{aligned}\phi_{S/C} - \tilde{\phi}_{cal} = (\phi^{S/C}_{struc} - \tilde{\phi}^{cal}_{struc}) + (\phi^{S/C}_{inst} - \tilde{\phi}^{cal}_{inst}) + (\phi^{S/C}_{pos} - \tilde{\phi}^{cal}_{pos}) \\ + (\phi^{S/C}_{ant} - \tilde{\phi}^{cal}_{ant}) + (\phi^{S/C}_{atmo} - \tilde{\phi}^{cal}_{atmo}) + (\phi^{S/C}_{iono} - \tilde{\phi}^{cal}_{iono}) \end{aligned} \quad (3.45)$$

where the contributions of the phase errors are due to the source structure ϕ_{struc}, the instrumental errors ϕ_{inst}, the source position errors ϕ_{pos}, the antenna position and deformation errors ϕ_{ant}, and propagation through atmosphere ϕ_{atmo} and ionosphere ϕ_{iono}. The superscripts indicate the source to which the phase error correspond, the spacecraft or the calibrator. If during the observation the separation between the spacecraft and calibrator lies within ~ 2 deg, it can be assumed that both sources are within isoplanatic patch. Therefore, the phase errors due to the propagation through the atmosphere and ionosphere are approximately the same along both lines of sight, hence $\phi^{S/C}_{atmo} \approx \tilde{\phi}^{cal}_{atmo}$ and $\phi^{S/C}_{iono} \approx \tilde{\phi}^{cal}_{iono}$. The same holds for the antenna related errors, therefore, $\phi^{S/C}_{ant} \approx \tilde{\phi}^{cal}_{ant}$. As explained in Section 3.3, after fringe-fitting the calibrator data is self-calibrated to correct for the source structure phase, so it can be assumed that $\tilde{\phi}^{cal}_{struc} = 0$. Hence, the remaining information in the phase-referenced difference phase are related to the spacecraft source structure, and the errors of the measured positions of the spacecraft and calibrator with respect to the a priori positions.

$$\phi_{S/C} - \tilde{\phi}_{cal} = \phi^{S/C}_{struc} + (\phi^{S/C}_{pos} - \tilde{\phi}^{cal}_{pos}) + \epsilon_{int} \quad (3.46)$$

where ϵ_{int} are the interpolation residuals errors.

As shown in Section 3.3, the fringe-fitting and self-calibration techniques were used on the calibrator data to determine and remove the delay, delay-rate and phase errors. This same procedure can be conducted with the spacecraft data, with the advantage that since phase-referencing was previously applied the parameters to be

estimated are reduced to only the phase errors (Equation 3.46). When applying the phase-referencing, the spacecraft data is coherently averaged over frequency, and, the residual phase variations in time become negligible, thus removing the delay and delay-rate parameters from the search space, respectively. Once the spacecraft is self-calibrated, the spacecraft source structure error $\phi_{struc}^{S/C}$ will be corrected for. Hence, the remaining phase error is due to the relative separation between the spacecraft and calibrator.

In order to retrieve the relative spacecraft position two approaches are considered: 1) imaging the spacecraft visibilities and 2) solving the astrometric measurement equation.

3.6.1. Imaging

When an image of the spacecraft is produced, the self-calibration process sets the center of the map to the a priori spacecraft position. The position of the spacecraft in the image will have an offset with respect to the map's center. This shift represents the error in the a priori spacecraft ephemeris. By determining the position offset and using the a priori spacecraft position and the calibrator position (whose absolute position with respect to ICRF is usually known with an accuracy better than 0.1 mas), then the relative position of the spacecraft is determined. In AIPS, the spacecraft position offset per solution interval is found with the task 'JMFIT', which fits a 2D Gaussian to the peak of the CLEANed map, as explained in Duev et al. [11]. The procedure carried out in AIPS was automated with a ParselTongue script [22].

3.6.2. Solving the fundamental astrometric equation

As explained in Duev et al. [10], the fundamental astrometric equation, for the case when the target is in the near field, can be written as,

$$\overrightarrow{\Delta\phi}\,\big|_t = \left(J_{ij}\cdot\overrightarrow{\Delta\alpha}\right)\big|_t, \tag{3.47}$$

where the vector $\overrightarrow{\Delta\phi}$ contains the differential phases of all baselines as in Equation 3.42, and the vector $\overrightarrow{\Delta\alpha} = (\Delta\varphi, \Delta\theta)$ are the spacecraft angular position corrections with respect to the a priori positions, and the matrix J contains the partial derivatives of the predicted geocentric differential delays τ_{ij} with respect to the geocentric spherical angular coordinates of the source, φ and θ, along the line of sight,

$$J\big|_t = \begin{pmatrix} \frac{\partial\tau_{12}}{\partial\varphi} & \frac{\partial\tau_{12}}{\partial\theta} \\ \vdots & \vdots \\ \frac{\partial\tau_{1N}}{\partial\varphi} & \frac{\partial\tau_{1N}}{\partial\theta} \\ \vdots & \vdots \\ \frac{\partial\tau_{N-1,N}}{\partial\varphi} & \frac{\partial\tau_{N-1,N}}{\partial\theta} \end{pmatrix} = \begin{pmatrix} \frac{\partial(\tau_1-\tau_2)}{\partial\varphi} & \frac{\partial(\tau_1-\tau_2)}{\partial\theta} \\ \vdots & \vdots \\ \frac{\partial(\tau_1-\tau_N)}{\partial\varphi} & \frac{\partial(\tau_1-\tau_N)}{\partial\theta} \\ \vdots & \vdots \\ \frac{\partial(\tau_{N-1}-\tau_N)}{\partial\varphi} & \frac{\partial(\tau_{N-1}-\tau_N)}{\partial\theta} \end{pmatrix}, \tag{3.48}$$

where N is the number of participating stations.

The phases $\overrightarrow{\Delta\phi}$ are subject to a 2π-ambiguity. This uncertainty corresponds to a bias in the phase delays $\tau_{ph} = \phi/2\pi f_0$, where f_0 is the transmitting frequency, of $\sim$ 120 ps for observations at X-band. In order to resolve this ambiguity, an optimal fit of the phase delays τ_{ph} (obtained from the narrowband processing of the spacecraft

data) to the group delays (obtained from the broadband processing of the spacecraft data) can be found by minimizing the squared error,

$$\Sigma_n \Sigma_i ((\tau_{ph}[i] + 2\pi n) - \tau_g[i])^2 \text{ , for } n \in \mathbb{N} \tag{3.49}$$

For more details in the practical implementation of the $2\pi-$ambiguity resolution and how to deal with the problems arising from the observation gaps in the spacecraft data due to phase-referencing refer to Duev et al. [11].

Once the unambiguous phases are retrieved, the least-squares solution of Equation 3.47 for each epoch t is given by,

$$\overrightarrow{\Delta\alpha}\Big|_t = \left((J^{\mathrm{T}} \cdot J)^{-1} \cdot J^{\mathrm{T}} \cdot \overrightarrow{\Delta\phi}\right)\Big|_t \tag{3.50}$$

The resulting angular corrections $\Delta\alpha$ are the angular displacements in the plane defined by the vector from geocenter to the target at a given epoch.

References

[1] Acton, C. H. 1996, Planetary and Space Science, 44, 65

[2] Beasley, A. & Conway, J. 1995, in Very Long Baseline Interferometry and the VLBA, Vol. 82, 327

[3] Boehm, J., Werl, B., & Schuh, H. 2006, J. Geophys. Res., 111, B02406, doi:10.1029/2005JB003629

[4] Born, M. & Wolf, E. 1999, Principles of Optics: Electromagnetic Theory of Propagation, Interference and Diffaction of Light, 7th edn. (Cambridge University Press)

[5] Clark, B. 1980, Astronomy and Astrophysics, 89, 377

[6] Clark, T. A. & Thomsen, P. 1988, Deformations in VLBI antennas (National Aeronautics and Space Administration, Goddard Space Flight Center, Greenbelt, Md.:), 1 v.

[7] Cotton, W. 1979, The Astronomical Journal, 84, 1122

[8] Davis, J., Herring, T., Shapiro, I., Rogers, A., & Elgered, G. 1985, Radio science, 20, 1593

[9] Deller, A. T., Tingay, S., Bailes, M., & West, C. 2007, Publications of the Astronomical Society of the Pacific, 119, 318

[10] Duev, D. A., Calvés, G. M., Pogrebenko, S. V., et al. 2012, Astronomy & Astrophysics, 541, A43

[11] Duev, D. A., Pogrebenko, S. V., Cimò, G., et al. 2016, Astronomy & Astrophysics, 593, A34

[12] Duev, D. A., Pogrebenko, S. V., & Molera-Calvés, G. 2011, Astronomy Reports, 55, 1008

[13] Ekers, R. 1999, in Synthesis Imaging in Radio Astronomy II, Vol. 180, 321

[14] Eubanks, T. 1991, in Proc. of the USNO workshop on Relativistic Models for Use in Space Geodesy, 60–82

[15] Feltens, J. & Schaer, S. 1998, in Proceedings of the IGS AC Workshop, Darmstadt, Germany

[16] Folkner, W. M., Williams, J. G., Boggs, D. H., Park, R. S., & Kuchynka, P. 2014, Interplanet. Netw. Prog. Rep, 196, 1

[17] Fukushima, T. 1994, Astronomy and Astrophysics, 291, 320

[18] Gurvits, L. & Pogrebenko, S. e. 2008, in ESA-ESTEC Contract No. 18386/NL/NR Final Report, jIVE Research Note 0011

[19] Hernández-Pajares, M., Juan, J., Sanz, J., et al. 2009, Journal of Geodesy, 83, 263

[20] Irwin, A. W. & Fukushima, T. 1999, Astronomy and Astrophysics, 348, 642

[21] Keimpema, A., Kettenis, M., Pogrebenko, S., et al. 2015, Experimental Astronomy, 39, 259

[22] Kettenis, M., van Langevelde, H. J., Reynolds, C., & Cotton, B. 2006, in Astronomical data analysis software and systems XV, Vol. 351, 497

[23] Klioner, S. A. 1991, in Geodetic VLBI: Monitoring Global Change, 188

[24] Kolmogorov, A. N. 1991, Royal Society of London Proceedings Series A, 434, 9, 10.1098/rspa.1991.0075

[25] Kouba, J. 2008, Journal of Geodesy, 82, 193

[26] Molera-Calvés, G., Pogrebenko, S., Cimò, G., et al. 2014, Astronomy & Astrophysics, 564, A4

[27] Moyer, T. 2005, Formulation for Observed and Computed Values of Deep Space Network Data Types for Navigation, JPL Deep-Space Communications and Navigation Series (John Wiley & Sons)

[28] Nothnagel, A. 2009, Journal of Geodesy, 83, 787, doi:10.1007/s00190-008-0284-z

[29] Petit, G. & Luzum, B. 2010, IERS conventions 2010 (IERS Technical Note No. 36), Tech. rep., Bureau International des Poids et Mesures Sevres.

[30] Petrov, L. 2018, RFC source position catalogue: rfc2018b. Consulted on June 2018

[31] Readhead, A. & Wilkinson, P. 1978, The Astrophysical Journal, 223, 25

[32] Romney, J. 1999, in Synthesis Imaging in Radio Astronomy II, ASP Conference Series, Vol. 180, 57

[33] Sarti, P., Abbondanza, C., & Vittuari, L. 2009, Journal of Geodesy, 83, 1115, doi:10.1007/s00190-009-0331-4

[34] Schaer, S., Gurtner, W., & Feltens, J. 1998, in Proceedings of the IGS AC workshop, Darmstadt, Germany, Vol. 9

[35] Schüler, T. 2001, On ground-based GPS tropospheric delay estimation (Univ. der Bundeswehr München)

[36] Schwab, F. R. & Cotton, W. D. 1983, The Astronomical Journal, 88, 688

[37] Sekido, M. & Fukushima, T. 2006, Journal of Geodesy, 80, 137

[38] Sovers, O. & Jacobs, C. S. 1996, Jet Propulsion Lab. Report, 1, 8339

[39] Sovers, O. J., Fanselow, J. L., & Jacobs, C. S. 1998, Reviews of Modern Physics, 70, 1393, 10.1103/RevModPhys.70.1393

[40] Steer, D., Dewdney, P., & Ito, M. 1984, Astronomy and Astrophysics, 137, 159

[41] Thompson, A. R., Moran, J. M., & Swenson Jr, G. W. 2008, Interferometry and synthesis in radio astronomy (John Wiley & Sons)

[42] Vandenberg, N. 1997, DRUDG: Experiment Preparation Drudge Work. NASA/Goddard Space Flight Center, Space Geodesy Program, VLBI Software Manual

[43] Wagner, J. 2009, Intel and Cell Software Spectrometer, `http://cellspe-tasklib.sourceforge.net`, open source project

CHAPTER 4

On the performance of the Doppler component of PRIDE

In Chapter 3 a description of the signal processing and analysis methodology used by PRIDE is given. The purpose of Chapter 3 is to explain how from the carrier signal received at multiple telescopes the angular position and radial velocity of the spacecraft can be derived. In this chapter, we will focus on the radial velocity observable, which is derived from the Doppler phase corrections of the spacecraft carrier tone. The purpose of this chapter is to, firstly, give the complete formulation of the observed measurements as obtained with PRIDE and the corresponding computed values, and secondly, to characterize the remaining Doppler noise of the measurements. The latter with the goal of providing an error budget for the Doppler component of the PRIDE technique to be able to benchmark its performance. This chapter addresses research question 1.

Planetary Radio Interferometry and Doppler Experiment (PRIDE) technique: A test case of the Mars Express Phobos Flyby

2. Doppler tracking: Formulation of observed and computed values, and noise budget.

T. M. Bocanegra-Bahamón[1,2,3], *G. Molera Calvés*[1,4], *L.I. Gurvits*[1,2], *D.A. Duev*[5], *S.V. Pogrebenko*[1], *G. Cimò*[1,6], *D. Dirkx*[2], *P. Rosenblatt*[7]

Published in *Astronomy & Astrophysics*, Vol. 609, A59, 2018

Abstract

Context. Closed-loop Doppler data obtained by deep space tracking networks, such as the NASA Deep Space Network (DSN) and the ESA tracking station network (Estrack), are routinely used for navigation and science applications. By shadow tracking the spacecraft signal, Earth-based radio telescopes involved in Planetary Radio Interferometry and Doppler Experiment (PRIDE) can provide open-loop Doppler tracking data when the dedicated deep space tracking facilities are operating in closed-loop mode only.

Aims. We explain the data processing pipeline in detail and discuss the capabilities of the technique and its potential applications in planetary science.

Methods. We provide the formulation of the observed and computed values of the Doppler data in PRIDE tracking of spacecraft and demonstrate the quality of the results using an experiment with the ESA Mars Express spacecraft as a test case.

Results. We find that the Doppler residuals and the corresponding noise budget of the open-loop Doppler detections obtained with the PRIDE stations compare to the closed-loop Doppler detections obtained with dedicated deep space tracking facilities.

1. Introduction

The Planetary Radio Interferometry and Doppler Experiment (PRIDE) technique exploits the radio (re-)transmitting capabilities of spacecraft from the most modern space science missions [10]. A very high sensitivity of Earth-based radio telescopes involved in astronomical and geodetic Very Long Baseline Interferometry (VLBI) observations and an outstanding signal stability of the radio systems allow PRIDE to conduct precise tracking of planetary spacecraft. The data from individual telescopes are processed both separately and jointly to provide Doppler and VLBI observables, respectively. Although the main product of the PRIDE technique is the VLBI observables (Duev et al. [11], paper 1 of this series), the accurate examination of the

1: Joint Institute for VLBI ERIC, The Netherlands
2: Delft University of Technology, The Netherlands
3: Shanghai Astronomical Observatory, China
4: Finnish Geospatial Research Institute, Finland
5: California Institute of Technology, USA
6: Netherlands Institute for Radio Astronomy, The Netherlands
7: Royal Observatory of Belgium, Belgium

changes in phase of the radio signal propagating from the spacecraft to each of the ground radio telescopes on Earth make the open-loop Doppler observables derived from each telescope very useful for different fields of planetary research.

Dedicated deep space tracking systems, for example, NASA's Deep Space Network (DSN) and ESA's tracking station network (Estrack), provide data to determine the precise state vector of a spacecraft, based on the spacecraft signal detected at the ground-based receivers. To this end, the tracking systems can provide a variety of radiometric data (*e.g.,* Doppler, range and interferometry data) under different operational schemes [48]. The type of tracking data needed for a particular spacecraft depends on the mission stage of the spacecraft and for which means these data will be used. However, this does not imply that several tracking data types cannot be used for the same purpose. In fact, the use of different precise and reliable tracking techniques not only enables a more challenging navigation performance, but could enhance various scientific experiment carried out during the mission [19, 31, 32].

The Doppler effect due to the relative motion of the radio elements can be retrieved from the signal received at the ground station in different ways. One way is to measure the changes in light travel time of the received spacecraft signal with a closed-loop mechanism [22]. In this tracking scheme, the received signal at the station is mixed with a local oscillator signal. Once the carrier frequency is found at the receiving station, a numerically controlled oscillator is set at the same value of the detected frequency and the carrier loop is closed [14, 45]. The bandwidth of the loop is gradually reduced to a preset operational value using its feedback mechanism. Once the 'phase-lock' is acquired, the resulting Doppler shifted beat frequency is input into a Doppler cycle counter. The cycle counter measures the total phase change of the Doppler beat over a count interval, thus yielding the change in range over the count interval. The output, *i.e.*, the Doppler cycle count, consists of an integer number from the Doppler counter itself and a fractional term from a Doppler resolver and is used to reconstruct the received spacecraft frequencies, also known as *sky frequencies* [36, 37]. The precision at which these measurements can be obtained, is limited by the way the time is tagged (*i.e.,* the quality of the timing standards) and the signal-to-noise ratio (S/N) of the measurements. Because of the mechanism used, the data derived is commonly known as *Doppler closed-loop* data.

The straightforwardness of this technique and the real-time availability of the data make closed-loop Doppler tracking the preferred tracking scheme when performing navigation and telemetry measurements with the DSN and Estrack networks. However, for radio science applications this is not necessarily the case. The term 'radio science' includes all the scientific information that can be derived from the interaction of the spacecraft signal with planetary bodies and interplanetary media as it propagates from the spacecraft to Earth [16–18, 23, 39, 51]. In some scenarios, for instance planetary atmospheric occultation [20, 46, 47] and ring occultation [29], the received signal can present abrupt changes in frequency and amplitude, yielding a loss-of-lock in a closed-loop tracking scheme. For such cases, an open-loop receiver is preferable. In this case, no real-time signal detection mechanism is present, but instead the frequency spectrum of the detected signal is downconverted, digitized, and recorded with a sufficiently wide bandwidth to be able to capture the high dynamics of the signal [25]. The data processing is performed at a later stage with a digital phase-lock loop (PLL), which simulates the real-time PLL-controlled system used in

the closed-loop receivers, and a fast Fourier transform (FFT) that estimates the frequency and amplitude of the received signal. The difference resides in the ability of the digital PLL of starting new locking processes once the system is considered out of lock, and the direct estimation of the frequency of the carrier tone at each sampling time. This mechanism allows an observer to directly reconstruct the sky frequency of parts of the detected signal that would be otherwise considered lost. For the post-processing of the open-loop Doppler, although it relies on the same main detection methods (PLL and FFT), there are various spectral analyses approaches that can be used [21, 28, 38, 50].

We present our approach for deriving Doppler open-loop data with the PRIDE technique, using a set of radio telescopes from the European VLBI Network (EVN) and the Very Large Baseline Array (VLBA). Although these telescopes are typically used for observations of natural cosmic radio sources, ranging from nearby stars to distant quasars, we demonstrated in the past that our approach, based on precision wideband spectral analysis, is capable of tracking planetary spacecraft signals [10, 11, 35, 53]. Since their conception, the equipment and data acquisition software of the DSN and VLBI networks have been developed in close collaboration between the two scientific communities. For this reason, the characteristics and capabilities of the VLBI network receivers and the DSN/Estrack open-loop receivers, also known as radio science receivers, are very similar. The post-processing techniques, however, may differ even between radio science teams using the same network because once the data are recorded the tracking center delivers these data to the science teams, who use their own software for data processing and analysis.

For these reasons, the two goals of this paper are as follows. First, we seek to present our processing technique to derive the open-loop Doppler data, and provide a clear formulation of the observed and computed Doppler observables and a noise budget of the derived tracking data. In this way we analyze the quality of open-loop Doppler data derived with VLBI telescopes through the PRIDE technique and compare it to the standards of the closed-loop Doppler data provided by the deep space networks. Second, since PRIDE uses another network of ground stations, this technique allows for the possibility of acquiring precise Doppler open-loop data independently from the tracking networks of the space agencies. For instance, one potential application is to use PRIDE, with the EVN and VLBA networks, to track spacecraft for navigation and telemetry purposes only when there are closed-loop tracking passes scheduled by the tracking facilities of the corresponding agency. In this way, PRIDE could allow radio science activities to be conducted in parallel by performing shadow tracking on the spacecraft signal. These goals are addressed in this paper in the framework of the PRIDE tracking of the ESA Mars Express (MEX) spacecraft during its flyby of Phobos in December 2013.

The MEX orbiter was launched in June 2, 2003 and has been orbiting the red planet since December 2003 in a highly elliptical polar orbit, with 86° inclination, periaerion of ~ 300 km, apoaerion of ~ 10100 km, and an orbital period of 6.7 h. Owing to its highly valuable science return the mission has been extended six times beyond its nominal mission duration [9]. The MEX telemetry, tracking, and command (TT&C) subsystem operates in a two-way mode, receives the transmitted uplink signal in X band (7.1 GHz), and provides coherent dual-frequency carrier downlinks at X band (8.4 GHz) and S band (2.3 GHz) via the spacecraft's 1.8 m high gain antenna (HGA)

for all radio science operations of the Mars Express Radio Science Experiment (MaRS) team [39]. On the ground MaRS activities are supported by the 35 m ESA Estrack New Norcia (NNO) station and the 70 m NASA Deep Space Network (DSN) stations, which are all equipped with hydrogen masers as part of the frequency and timing systems. On December 29, 2013, MEX performed a Phobos fly-by at a distance of ~ 45 km from its surface. Under the European Satellite Partnership for Computing Ephemerides (ESPaCE) consortium an opportunity was offered to track the spacecraft with the PRIDE technique using VLBI stations alongside the customary Estrack and DSN stations. The tracking session lasted for 25 hours around the flyby event, using 31 VLBI stations around the world, which are also equipped with hydrogen masers as frequency standards, observing at X-band (channel starting at 8412 MHz, recording bandwidth of 16 MHz) in a three-way mode. The PRIDE setup for this particular tracking experiment is described in detail in Duev et al. [11] (paper 1).

The paper is organized as follows. In Section 2, the processing pipeline to extract the Doppler detections from the raw open-loop data is explained along with the formulation of the observed and computed values of the instantaneous Doppler observables. In Section 3, the observations and the open-loop Doppler detections obtained from the ESA MEX spacecraft in December 2013 are discussed. The quality of the PRIDE Doppler detections is assessed by comparing the Doppler noise obtained by the multiple VLBI stations involved in the experiment with the noise of the Estrack and DSN stations during the same tracking session. The main contributing noise sources are quantitatively discussed. Section 4 summarizes the results and discusses how the findings can improve the planning and enhance the science return of future radio science experiments with PRIDE.

2. PRIDE Doppler observables

In the nominal MEX gravimetry experiments, the orbit perturbations caused by the gravitational fields of Mars and, in this particular case, of Phobos were determined via precise two-way radio Doppler tracking of MEX with dual-frequency downlink during pericenter passes with the Estrack and DSN stations [15]. However, for the MEX Phobos flyby on December 29, 2013, the PRIDE joined the tracking effort in a three-way mode to assess the performance of the technique; in the three-way mode, the signal received was re-transmitted by the spacecraft with a network of radio telescopes none of which is the initial transmitting ground station, also known as *shadow tracking*.

2.1. Observed values of the Doppler observables

The transmitting/receiving systems at DSN and Estrack stations used for spacecraft radiometric tracking can operate in a closed- or open-loop manner. In these networks, the primary receiver is the closed-loop receiver, which uses a mechanism to phase lock onto the received carrier signal. In this setup, the receiver passband is continuously aligned to the peak of the carrier tone and its bandwidth is gradually narrowed, allowing the retrieval of real-time tracking data and telemetry [22]. The open-loop receivers, on the other hand, do not have such a feedback mechanism [25], hence the bandwidth of the receiver passband is predefined and remains fixed during each observation. For this reason, the carrier signal filtering and tracking is performed at a

later stage using the accurately timed detection of the signal recorded at the ground station. The radio telescopes used in PRIDE only operate in the open-loop mode. At each station, the received signals are amplified, heterodyned to the baseband, digitized, time-tagged, and recorded onto disks via the standard VLBI data acquisition systems with Mark5 A/B or FlexBuff recording systems [27]. For the data processing, the disks can be shipped or the data are transferred directly via high-speed networks to the VLBI data processing center at the Joint Institute for VLBI ERIC (JIVE) in the Netherlands.

The Doppler detections are extracted from the raw open-loop data via the PRIDE spacecraft tracking software, consisting of three packages `SWSpec`, `SCtracker`, and `dPLL`[8][35]. In the nominal PRIDE setup we observe two sources, the spacecraft signal and natural radio sources, which are used as calibrators. A large number of the natural sources observed with radio telescopes emit broadband electromagnetic radiation spanning many gigahertz in the frequency domain, however the signal is typically weak. It is therefore desirable to use as wide a frequency band as possible in order to detect the signal. The open-loop receiver systems of the VLBI stations are typically set up to record 4, 8, 16, or 32 frequency channels with 4, 8, 16, or 32 MHz bandwidth per sub-band. However, the spacecraft signal spectrum takes up only a fraction of the sub-band (see Figure 1a). For this reason, the first processing step is to extract the narrowband containing the spacecraft signal carrier and/or tones present in the spectrum. The `SWSpec` extracts the data from the channel where the spacecraft signal is located, and subsequently performs a window-overlapped add (WOLA) direct Fourier transform (DFT), followed by a time integration over the obtained spectra. The result is an initial estimate of the spacecraft carrier tone along the observation scan (Figure 1b). As shown in Figure 1b, the detected carrier tone has a moving phase throughout the scan, which is caused by the change in relative velocity between the spacecraft and the receiver. The goal is to extract the Doppler shift, first by fitting the changing frequency of the carrier tone by a n-order polynomial, and then using the fit to stop the moving phase of the tone. The latter step is performed with the `SCtracker` software, which subsequently allows the tracking, filtering, and extraction of the tone in a narrowband. Figure 1c shows the narrowband output signal of the `SCtracker`. At this point, the spacecraft signal is in a band of a few kHz bandwidth, in contrast to the initial $4 - 32$ MHz bandwidth sub-band. The final step is conducted by the digital phase-locked-loop (`dPLL`), which performs high-precision reiterations of the previous steps – time-integration of the overlapped spectra, phase polynomial fitting, and phase-stopping correction – on the narrowband signal. After the phase-stopping correction, the power spectrum is accumulated for a selectable averaging interval. Using a frequency window around the tone, the maximum value of the accumulated spectrum is determined. The corresponding frequency of the peak of the spectrum is stored, using as the time tag the middle of the averaging interval. This procedure is conducted throughout the whole range of spectra. The output of the `dPLL` is the filtered down-converted signal (Figure 1d) and the final residual phase in the stopped band with respect to the initial phase polynomial fit. The bandwidth of the output detections is typically about 20 Hz with a frequency spectral resolution of ~ 2 mHz [33].

The PRIDE post-processing pipeline allows us to determine the instantaneous

[8] https://bitbucket.org/spacevlbi/

Doppler shift of the recorded tracking data, which is different from the integrated Doppler observables that are derived from closed-loop tracking data. For the purposes of orbit determination and the estimation of physical parameters of a celestial body using the Doppler data, it is important that this difference is taken into account when defining the observed and computed values of the Doppler observable. In the closed-loop case, the Doppler observables are derived by computing the change in the accumulated Doppler cycle counts from the spacecraft carrier phase measurements over a time interval at the receiver, as explained in detail in Section 13.3 of Moyer [37]. The corresponding modeled values are obtained by taking the difference in range at the beginning and end of the time interval. In the open-loop case, performed by PRIDE as explained in the previous paragraph, the observed values of the instantaneous Doppler observable (for one-way or three-way mode) are derived directly from an estimate of the carrier tone frequency of the spacecraft spectrum. Therefore, the observables are simply retrieved by adding the base frequency f_{base} (which for the experiment analyzed in this paper was 8412 MHz, as shown in Figure 1a) of the channel containing the spacecraft signal and the obtained time averaged tone frequencies f_{tone} at each sampled time t_i,

$$f_R(t_i) = f_{base} + f_{tone}(t_i), \tag{1}$$

where f_R is the received frequency.

The integration time is defined by the number of FFT points used at the `dPLL` on the ~2 kHz bandwidth signal (Figure 1c). For the gravity field determination experiments, the desired integration time is ~10 s, hence 20,000 FFT points are used in `dPLL`. The uncertainty of each tone frequency estimate is derived from the final residual phase of the `dPLL` output.

2.2. Computed values of the Doppler observables

To process the Doppler data obtained with PRIDE, a model is required that provides the instantaneous Doppler shift f_R/f_T, where f_R and f_T denote the observed frequency of the received and transmitted electromagnetic signal, respectively. Fundamentally, this frequency ratio is obtained from

$$\frac{f_R}{f_T} = \frac{d\tau_T}{d\tau_R} = \left(\frac{d\tau}{dt}\right)_T \frac{dt_T}{dt_R} \left(\frac{dt}{d\tau}\right)_R, \tag{2}$$

where τ and t denote proper time of the observer and coordinate time, respectively. The R and T subscripts denote properties of receiver and transmitter. The coordinate times of transmission and reception are related via the light-time equation

$$t_R - t_T = \frac{1}{c} \left|\mathbf{x}_R(t_R) - \mathbf{x}_t(t_T)\right| + \Delta(t_R, t_T), \tag{3}$$

where $\mathbf{x}_R(t)$ and $\mathbf{x}_T(t)$ are the barycentric positions of the receiver and transmitter, $\Delta(t_R, t_T)$ the relativistic correction to the light travel times and c is the speed of light.

The main complication in obtaining an explicit expression from Equation 2 is to compute the terms $d\Delta(t_R, t_T)/dt_R$ and $d\Delta(t_R, t_T)/dt_T$. To expand these equations, we use the formalism of Kopeikin & Schäfer [24], where it is assumed that

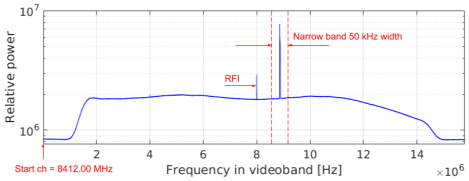

(a)

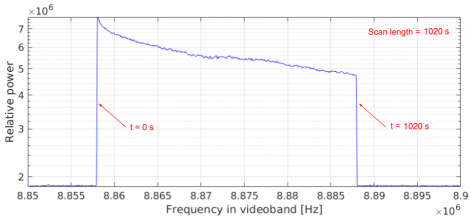

(b)

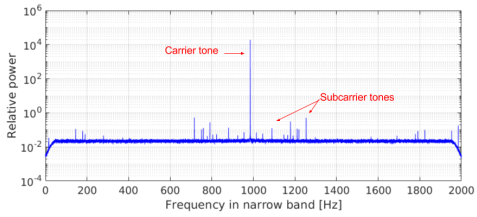

(c)

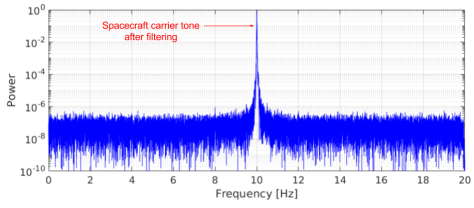

(d)

Figure 1: Example of Doppler data processing pipeline using observations of MEX during Phobos flyby by Hartebeesthoek (see Section 3). Panel (a) is the typical resulting average power spectrum of a scan after running the `SWSpec` software. In the 16 MHz pre-defined sub-band starting at 8412 MHz, the spacecraft signal is found in the spectrum. A narrowband containing the moving phase of the spacecraft carrier/tone is selected (in this case of 50 kHz bandwidth) to model the Doppler shift using an n-order polynomial frequency fit. Panel (b) shows a zoom of the spectrum inside the selected narrowband window to perform the fit. Here the moving phase of the carrier tone is visible along the duration of the scan. After the fit is performed, `SCtracker` applies the polynomial coefficients after converting the sample to the baseband sample to stop the moving phase of the tone. In this way, `SCtracker` extracts an initial fit of the Doppler shift. Panel (c) shows the output of the `SCtracker`, which is a phase-stopped filtered out signal in a 2 kHz narrowband in baseband. Finally, the `dPLL` performs high-precision iterations of the time integration of the overlapped spectra, phase polynomial fitting, conversion to baseband, and phase-stopping corrections, using narrowband windows around the carrier tone. The iterations stop when the window bandwidth reaches 20 Hz, as shown in (d), allowing the extraction of the frequency and phase residuals of the spacecraft carrier tone with a 2 mHz frequency spectral resolution.

- The metric $g_{\alpha\beta}$ can be expanded to post-Minkowskian order, so that $g_{\alpha\beta}(\mathbf{x}, t) = \eta_{\alpha\beta} + h_{\alpha\beta}(\mathbf{x}, t)$, where $\eta_{\alpha\beta}$ is the Minkowski metric and the metric perturbation $h_{\alpha\beta} = O(G)$.
- All bodies with gravity fields that perturb the null geodesic of the electromagnetic signal can be modeled as point masses.
- All bodies with gravity fields that perturb the null geodesic of the electromagnetic signal have a constant barycentric velocity over the relevant time interval of a single measurement.

Under these assumptions, $\Delta(t_R, t_T)$ reduces to (neglecting second order terms in v/c) the static case of which is also known as the Shapiro effect [43]:

$$\Delta(t_R, t_T) = -\frac{2G}{c^3}\sum_{a=1}^{N} m_a \left(\ln \frac{r_a(t_R, s_R) - \mathbf{k}\cdot\mathbf{r}_a(t_R, s_R)}{r_a(t_T, s_T) - \mathbf{k}\cdot\mathbf{r}_a(t_T, s_T)} - \left(\mathbf{k}\cdot\frac{\mathbf{v}_a(t_R, s_R)}{c}\right)\ln\left(r_a(t_R, s_R) - \mathbf{k}\cdot\mathbf{r}_a(t_R, s_R)\right) + \left(\mathbf{k}\cdot\frac{\mathbf{v}_a(t_T, s_T)}{c}\right)\ln\left(r_a(t_T, s_T) - \mathbf{k}\cdot\mathbf{r}_a(t_T, s_T)\right)\right) \quad (4)$$

where G is the universal gravitational constant, m_a is the mass of the ath body, $\mathbf{k}$ is the direction of propagation of the radio wave (defined in Equation 8), $\mathbf{r}_a(t_R, s_R) = \mathbf{x}_R(t_R) - \mathbf{x}_a(s_R)$ where $\mathbf{x}_a(s_R)$ is the barycentric position of the ath body at s_R, $\mathbf{r}_a(t_T, s_T) = \mathbf{x}_T(t_T) - \mathbf{x}_a(s_T)$ where $\mathbf{x}_a(s_T)$ is the barycentric position of the ath body at s_T, $\mathbf{v}_a(t_R, s_R) = \mathbf{v}_R(t_R) - \mathbf{v}_a(s_R)$ where $\mathbf{v}_a(s_R)$ is the barycentric velocity of the ath body at s_R, and $\mathbf{v}_a(t_T, s_T) = \mathbf{v}_T(t_T) - \mathbf{v}_a(s_T)$ where $\mathbf{v}_a(s_T)$ is the barycentric velocity of the ath body at s_T. In the above, the parameter s denotes the retarded time of body a w.r.t. either the signal transmission or signal reception for T and R subscripts, respectively. This time parameter is obtained from the light-time equation of Equation 3, only now by considering the perturbing body a as the transmitting body, so that

$$t_R - s_R = \frac{1}{c}\left|\mathbf{x}_R(t_R) - \mathbf{x}_a(s_R)\right| \quad (5)$$

$$t_T - s_T = \frac{1}{c}\left|\mathbf{x}_T(t_T) - \mathbf{x}_a(s_T)\right|. \quad (6)$$

Physically, these times represent the time at which the gravitational signal from body a must be evaluated for its effect on the transmitter at t_T and the receiver at t_R to be modeled, implicitly assuming c to be the speed of gravity. Although we omit any a sub/superscript of the times s, we stress that these times are *different* for each perturbing body a.

Under these above assumptions, as shown by Kopeikin & Schäfer [24], Equation 2 can be written as

$$f_R = f_T \frac{1 - \mathbf{k}\cdot\mathbf{v}_R/c}{1 - \mathbf{k}\cdot\mathbf{v}_T/c} R(\mathbf{v}_R, \mathbf{v}_T, t_R, t_T), \quad (7)$$

where $\mathbf{v}_R$ and $\mathbf{v}_T$ are the barycentric velocity vectors of the receiving station at reception time t_R and at transmission time t_T, respectively. The term R denotes a set of (special and general) relativistic corrections. The unit vector $\mathbf{k}$ is the direction along which the radio wave propagates at past null infinity (*i.e.,* when following the signal back along the null geodesic to $t \to -\infty$), which can be expressed as

$$\mathbf{k} = -\mathbf{K} - \boldsymbol{\beta}(t_R, s_R) + \boldsymbol{\beta}(t_T, s_T), \tag{8}$$

where $\mathbf{K}$ is the geometric direction of the propagation of the electromagnetic wave in a flat space-time, and $\boldsymbol{\beta}(t_R, s_R)$ and $\boldsymbol{\beta}(t_T, s_T)$ are the relativistic corrections as a function of the states of body a at the retarded times of reception and transmission of the electromagnetic signal, respectively. These vectors are defined as follows,

$$\mathbf{K} = -\frac{\mathbf{x}_R - \mathbf{x}_T}{|\mathbf{x}_R - \mathbf{x}_T|} \tag{9}$$

$$\beta^i(t,s) = -\frac{2G}{|\mathbf{x}_T - \mathbf{x}_R|c^2} \sum_{a=1}^{N} m_a \left[\frac{1 - \mathbf{k}\cdot\mathbf{v}_a(s)/c}{\sqrt{1 - v_a^2(s)/c^2}} \frac{r_a^i(t,s) - k^i(\mathbf{k}\cdot\mathbf{r}_a(t,s))}{r_a(t,s) - \mathbf{k}\cdot\mathbf{r}_a(t,s)} \right]$$
$$- \frac{4G}{|\mathbf{x}_T - \mathbf{x}_R|c^2} \sum_{a=1}^{N} \left[\frac{m_a}{\sqrt{1 - v_a^2(s)/c^2}} \left[v_a^i(s)/c - k^i(\mathbf{k}\cdot\mathbf{v}_a(s)/c) \right] \ln\left(r_a(t,s) - \mathbf{k}\cdot\mathbf{r}_a(t,s)\right) \right] \tag{10}$$

The relativistic term R in Equation 2 can be decomposed as follows:

$$R(v_R, v_T, t_R, t_T) = \left[\frac{1 - (v_T/c)^2}{1 - (v_R/c)^2} \right]^{1/2} \left[\frac{a(t_T)}{a(t_R)} \right]^{1/2} \frac{b(t_R)}{b(t_T)}, \tag{11}$$

where the first term accounts for the special relativistic Doppler shift, the second term accounts for the general relativistic corrections due to the $d\tau/dt$ terms in Equation 2, and the final term is (along with the terms $\boldsymbol{\beta}$ given above) a result of expanding $d\Delta/dt$ when inserting Equation 3 into the middle term on the right-hand side of Equation 2. The terms a and b are given by

$$a(t) = 1 + \frac{2G}{c^2} \sum_{a=1}^{N} \frac{m_a \sqrt{1 - v_a^2(s)/c^2}}{r_a(t,s) - \mathbf{v}_a(s)\cdot\mathbf{r}_a(t,s)/c}$$
$$- \frac{4G}{c^2 - v^2} \sum_{a=1}^{N} \frac{m_a}{\sqrt{1 - v_a(s)^2/c^2}} \frac{(1 - \mathbf{v}(t)\cdot\mathbf{v}_a(s)/c^2)^2}{r_a(t,s) - \mathbf{v}_a(s)\cdot\mathbf{r}_a(t,s)/c} \tag{12}$$

$$b(t) = 1 + \frac{2G}{c^2} \sum_{a=1}^{N} \frac{m_a}{\sqrt{1 - v_a^2(s)/c^2}} \frac{1 - \mathbf{k}\cdot\mathbf{v}_a(s)/c}{r_a(t,s) - \mathbf{v}_a(s)\cdot\mathbf{r}_a(t,s)/c} \cdot$$
$$\left[\frac{(1 - \mathbf{k}\cdot\mathbf{v}_a(s)/c)(\mathbf{k}\times\mathbf{v}(t)/c)\cdot(\mathbf{k}\times\mathbf{r}_a(t,s))}{r_a(t,s) - \mathbf{k}\cdot\mathbf{r}_a(t,s)} \right.$$
$$\left. - \frac{(\mathbf{k}\times\mathbf{v}_a(s)/c)\cdot(\mathbf{k}\times\mathbf{r}_a(t,s))}{r_a(t,s) - \mathbf{k}\cdot\mathbf{r}_a(t,s)} + \mathbf{k}\cdot\mathbf{v}_a(s)/c \right]. \tag{13}$$

Evaluating this algorithm for the one-way Doppler case requires $2N + 1$ solutions of light-time equations, once for Equation 3 and N for both Equations 5 and 6, with N the number of bodies perturbing the path of the signal. These equations are implicit and must be solved iteratively. For Equation 3, we must compute t_T from a given t_R. We initialize $t_{T(1)} = t_R$ and iterate to find $t_{T(n+1)}$ from $t_{T(n)}$ using the Newton-Raphson method as follows:

$$t_{T(n+1)} = t_{T(n)} - \frac{t_R - t_{T(n)} - \frac{|\mathbf{x}_R - \mathbf{x}_T|}{c} - \Delta_{(n)}(t_R, t_{T(n)})}{\frac{\mathbf{x}_R - \mathbf{x}_T}{|\mathbf{x}_R - \mathbf{x}_T|} \frac{\mathbf{v}_T(t_{T(n)})}{c} - 1}. \tag{14}$$

The iterative procedure converges when $|t_{T(n+1)} - t_{T(n)}| \leq \epsilon$ for some predefined small ϵ. For the evaluation of the term Δ_n, the unit vector $\mathbf{k}$ is also updated iteratively using Equations 8, 9, and 10, initially assuming $\mathbf{k}_{(1)} = -\mathbf{K}$.

After the convergence of t_T, the values for $\mathbf{k}$, $\mathbf{r}_a(t_T, s_T)$, $\mathbf{v}_a(t_T)$, $\mathbf{x}(t_T)$, and $\mathbf{v}(t_T)$ are computed and the values for the general relativistic corrections $a(t_T)$, $a(t_R)$, $b(t_T)$, and $b(t_R)$ are determined. Finally, the instantaneous one-way Doppler frequency at reception time t_R can be determined from Equation 2.

The explicit formula for the two- and three-way observables for the propagation of the radio signal emitted from the ground station on Earth, with position $\mathbf{x_T}$ and velocity $\mathbf{v_T}$ at t_T, then received and transponded back to Earth by a spacecraft with position $\mathbf{x_S}$ and velocity $\mathbf{v_S}$ at t_S, where the superscripts '+' and '-' denote received on uplink and transponded on downlink, and finally received at a ground station on Earth, with position $\mathbf{x_R}$ and velocity $\mathbf{v_R}$ at t_R, is written as

$$f_R = f_T M \left(\frac{1 - \mathbf{k}^+ \cdot \mathbf{v}_S^+}{1 - \mathbf{k}^+ \cdot \mathbf{v}_T} R(v_T, v_S^+, t_T, t_S^+) \right) \frac{1 - \mathbf{k}^- \cdot \mathbf{v}_R}{1 - \mathbf{k}^- \cdot \mathbf{v}_S^-} R(v_S^-, v_R, t_S^-, t_R), \tag{15}$$

where again all the positions and velocities are given with respect to the solar system barycenter.

The solution to Equation 15 (the three-way Doppler predictions) is found in a similar manner as for Equation 2 (the one-way predictions) by first solving the expression for the uplink (in parenthesis in Equation 15), this time estimating the signal reception time at the spacecraft t_S^+ and subsequently determining all the uplink parameters corresponding to t_S^+ with the same iteration procedure as explained above. Once the expression in the parenthesis is solved, the downlink part is found as for Equation 15, estimating the signal transmission time at the spacecraft t_S^- and determining the corresponding downlink parameters. In Equation 15, f_T is the frequency transmitted by the ground station at time t_T and M is the corresponding spacecraft turnaround ratio. The terms R^+ and R^- are the relativistic corrections on uplink and downlink, respectively.

In a practical implementation of this algorithm, it is important to explicitly recompute all state vectors at each step, as any expansion quickly becomes inaccurate on typical deep-space craft light travel times.

3. MEX Phobos Flyby: GR035 experiment

The global VLBI experiment was designed to track MEX 14 hours prior to and 11 hours after its closest-ever Phobos fly-by at approximately 7:21 (UTC) on December

29, 2013. At the time of the experiment, Mars was at a distance of ~ 1.4 AU from the Earth with a solar elongation of ~ 87 degrees. During the 25 hours, MEX was tracked by the Estrack New Norcia (NNO; western Australia) station, DSN DSS-63 (Robledo, Spain) and DSS-14 (Goldstone, California, USA) stations, and 31 VLBI radio telescopes around the world. The latter were organized through the global VLBI experiment GR035. The experimental setup of GR035 was presented in Duev et al. [11]. During the first nine hours, NNO was the transmission station, followed by eight hours of tracking with DSS-63, and finally eight hours with DSS-14. The distribution of the telescopes over the duration of the experiment is presented in Figure 2, 3, and 7 in Duev et al. [11]. The spacecraft operated in the two-way mode with an X-band uplink (7.1 GHz) and dual simultaneous S/X-band downlink (2.3/8.4 GHz) transponded by the high gain antenna (HGA) pointing toward the Earth. The Estrack and DSN stations produced two-way S- and X-band Doppler closed-loop data products. From the 31 VLBI stations involved in the experiment, only the detections of 25 stations were used for the analysis presented in this paper, as listed in Table 1, owing to different technical problems with the remaining six stations during the observation.

We formed the Doppler residuals by differencing the Doppler detections, obtained as explained in Section 2.1, with the predicted Doppler, derived as explained in Section 2.2 via the latest MEX navigation post-fit orbit of December 2013 provided by the European Space Operations Centre (ESOC)[9]. In order to correctly determine the Doppler noise of the residuals, we flagged some data out. In particular, the data obtained during occultations and the flyby event were discarded. Additionally, we discarded a number of scans that presented systematic outliers, for instance, when the transmission mode at the ground station changed. We found that the Doppler residuals obtained with the VLBI stations are in agreement with the DSN and Estrack residuals. Figure 2 shows as an example the frequency residuals found with the 25 m antenna of the Very Long Baseline Array (VLBA) at Kitt Peak (designation Kp) and the residuals of the 70 m DSS-63 and DSS-14 antennas. In this case, the median value of the difference between the fit of Kp and the fit of DSS-63 and DSS-14, respectively, remains below 1 mHz for an integration time of 10 s. For other VLBI stations, the median (after flagging) of the Doppler residuals was found to be approximately 2 mHz.

In order to determine the quality of the PRIDE Doppler detections of the different VLBI stations involved in this experiment, first we had to identify the different sources that contribute to the overall noise of the Doppler residuals. The signal received at the ground stations have random errors introduced by the instrumentation on board the spacecraft and at the receiving system, and the random errors introduced by the propagation of the signal through the different media along the line of sight of the ground station. Additionally, systematic errors can also be introduced, for instance, when calibrating the signal or in the models used to generate the predicted Doppler signature. The calibration of the Doppler observables in relation to the signal delays induced by the ionosphere of the Earth are performed using the total vertical electron content (vTEC) maps available from the International GNSS Service (IGS) on a daily basis with a two-hour temporal resolution on a global grid [13]. The calibration of the tropospheric signal delays is applied via the Vienna Mapping Functions VMF1 [7] or ray-tracing through the Numerical Weather Models (NWM) [12], depending on the

[9]ftp://ssols01.esac.esa.int/pub/data/ESOC/MEX/ORMM_FDLMMA_ DA_131201000000_01033.MEX

antenna elevation. The systematic errors due to the model and orbit used to derive the Doppler residuals and the residual systematic noise resulting from the ionospheric and tropospheric delay calibration, are not characterized in this paper.

The random errors introduced by the instrumentation are analyzed in Section 3.1, and the random errors introduced by the propagation of the signal through the interplanetary media are treated in Section 3.2. Finally, in Section 3.3 the summary of the noise budget is given.

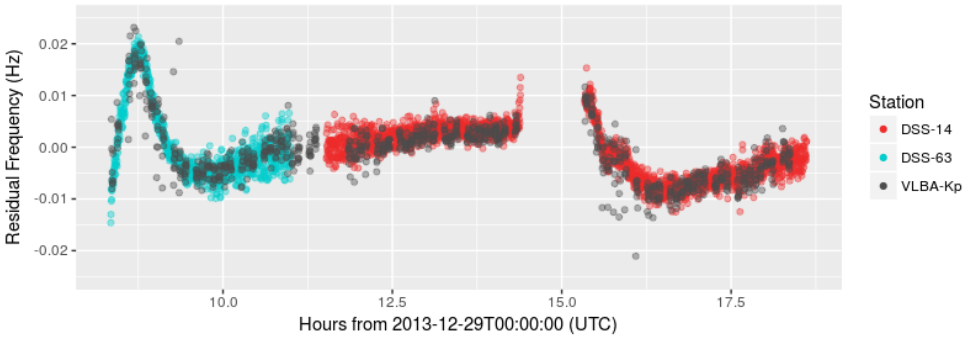

Figure 2: Comparison of the Doppler residuals obtained with VLBA-Kp (in black), DSS-63 (in blue), and DSS-14 (in red). The median value of the difference between the fit of VLBA-Kp and the fit of DSS-63 and DSS-14, respectively, remains below 1 mHz, for an integration time of 10 s.

3.1. Instrumental noise

The noise budget of the two-way Estrack/DSN Doppler detections and the three-way PRIDE Doppler detections include instrumental noises introduced at the transmitting ground station (electronics, frequency standard, and antenna mechanical noise) and at the spacecraft (electronics), which are common to both observables [5, 19]. Hence, regarding instrumental noises, the difference between these noise budgets resides at the receiving stations: the thermal noise, induced by the ground station receiver system and the limited received downlink power, the frequency and timing systems' noise, and the antenna mechanical noise. In this paper, only the first two sources of noise are treated since the antenna mechanical noise of the VLBI stations has not yet been characterized for the time intervals relevant to this study.

The thermal noise of the ground station is characterized by the RMS of the random fluctuations of the total system power at the ground station. The one-sided phase noise spectral density S_ϕ of the received signal gives the relative noise power to the carrier tone, contained in a 1 Hz bandwidth chosen to be centered at a frequency with a large offset Δf from the carrier frequency $f_{carrier}$ [52],

$$S_\phi = \frac{P_{sideband}(f_{carrier} + \Delta f)}{P_{carrier}}, \tag{16}$$

where $P_{carrier}$ is the power of the carrier tone and $P_{sideband}$ is the power of the 1 Hz bandwidth band.

The S/N is then approximated by $1/S_\phi$. As explained in [6, 40], the Allan deviation of white phase noise can be estimated by

$$\sigma_y(\tau) \approx \frac{\sqrt{3\mathrm{B}S_\phi}}{2\pi f_0 \tau} \tag{17}$$

where f_0 is the nominal frequency of the Doppler link.

Using Equations 17 and 16, and since $\mathrm{S/N}(\tau, \mathrm{B}) = \mathrm{S/N}(1\,\mathrm{s}, 1\,\mathrm{Hz})\sqrt{\frac{\tau}{\mathrm{B}}}$, the Allan deviation for the S/N detections of the different telescopes were determined, as shown in Table 1. During the Phobos flyby science operations conducted with MEX, the two-way closed-loop Doppler data was obtained using a carrier loop bandwidth of 30 Hz at the ground stations with 10 s integration time [15]. For the VLBI telescopes, the three-way open-loop Doppler data was initially recorded in a 16 MHz wide band and then processed with the software described in Section 2.1, for a final phase detection of 20 Hz bandwidth, with 10 s integration time. During the MEX orbits, for which NNO and DSS-14 were the transmitting stations, the telemetry was being transmitted except during MEX's nominal observation phase around the pericenter passage. However, during the orbit where DSS-63 was the transmitting station, in which the Phobos flyby occurred, the telemetry was turned off throughout the whole orbit. For the Doppler error budget, only the time slots planned as radio science passes are taken into account, since the average S/N calculated with Equation 16 drops when the telemetry is on. In Table 1 we also give the values of the sensitivity of each telescope, which for single-dish radio telescopes is defined as the system equivalent flux density (SEFD) [10]. This value is useful when comparing the performance between ground stations, since it comprises information about the total noise of the system and the collecting area of the antenna. Also when planning an experiment, it is important to know the nominal SEFD of a station at given frequency, since it can be used to compute the expected S/N of a detection.

The 65 m dish Tianma [11] has the highest S/N detections with a downlink power at reception 15 dB higher than for the smallest stations, i.e., the 12 m Yarragadee, Katherine, Hobart, and Warkworth, as expected because of their smaller collecting area, at elevations higher than 30 degrees. At $\tau = 10\,s$ the corresponding Allan deviation is 4.6×10^{-15}. Table 1 uses the average S/N values over the whole coverage of each telescope. However, because of the large variation of the elevation of the antennas during the several hours-long tracking sessions, there are periods of time for which smaller antennas achieve similar S/N levels as larger antennas. Figure 3 shows such an example in which for 3 hours the 15 m Hartbeesthoek achieves better S/N levels than the 25 m Urumuqi and similar S/N levels than the 25 m Onsala because of a more favorable antenna elevation (at elevations < 20 degrees, several noise contributions at the antenna rapidly increase, such as the atmospheric and spillover noise).

Regarding the noise induced by the frequency and timing systems, the Estrack, DSN, VLBA, and EVN stations are all equipped with hydrogen masers frequency stan-

[10] SEFD is equal to $2kT_{sys}/A_e$, where A_e is the effective collecting area of the antenna, T_{sys} is the total system noise temperature, and k is the Boltzmann constant. The SEFD is a measurement of the performance of the antenna and receiving equipment since it gives the flux density (in Jy) produced by an amount of power equal to the off-source noise in an observation.

[11] With exception of Tianma, the VLBI stations involved in the experiment have much smaller collecting areas than the 70 m DSS-14 and DSS-63. However, there are several VLBI stations whose diameters are close to that of NNO (*e.g.,* Ys, Sv, Zc, Bd, and Km).

dards, which provide a stability better than $4 < 10^{-14}$ at $\tau = 10\,\mathrm{s}$ ($< 10^{-15}$ at $\tau = 1000\,\mathrm{s}$). Hence the noise contributions related to the frequency standard should be on the same order of magnitude for the different networks.

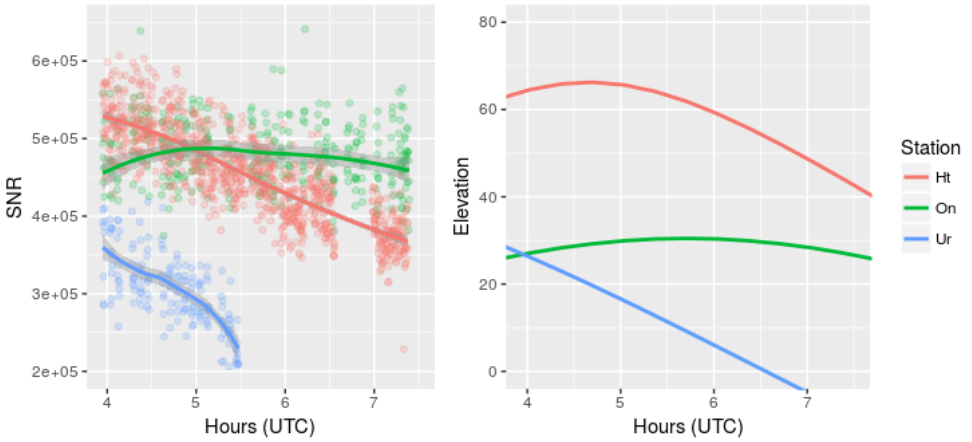

Figure 3: Signal-to-noise ratio and elevation angle comparison between 25 m Ur, 25 m On, and 15 m Ht radio telescopes from 4:00 - 7:30 UTC on December 29, 2013 (TX: DSS-63). The left panel shows that although Ht (in pink) has a lower collecting area, it achieves higher S/N levels than Ur (in blue) and similar S/N levels than On (in green). The right panel shows the elevation angle of each antenna during the same time period from which the correlation with the S/N levels of each station is evident.

3.2. Medium propagation noise

The precision of the Doppler detections is also affected by the noise introduced by the propagation of the radio signal through the interplanetary medium, ionosphere, and troposphere. The effects of ionospheric and interplanetary scintillation can be studied using the differenced phases of the signals received in S band, ϕ_s, and X band, ϕ_x, $\phi_\Delta(t) = \phi_s - \frac{3}{11}\phi_x$ [26]. By subtracting the phases, the contribution of the dispersive plasma scintillations can be isolated. The Allan variance of the differenced phases is related to its two-sided phase power spectrum $S_\phi(f)$ [3, 6] by

$$\sigma_y^2(\tau) = \int_0^\infty S_\phi(f) \frac{f^2}{f_0^2} \frac{\sin^4(\pi\tau f)}{(\pi\tau f)^2} df. \tag{18}$$

As explained in Armstrong et al. [3], when the phase spectrum can be approximated to $S_\phi(f) = Af^{-m}$, Equation 18 can be rewritten as

$$\sigma_y^2(\tau) = \frac{A\tau^m}{\pi^2 f_0^2 \tau^3} \int_0^\infty \frac{\sin^4(\pi z)}{z^m} dz. \tag{19}$$

A first-order approximation of the phase spectrum on a logarithmic scale is performed as explained in [35], from which the slope m and the constant A are determined using only the Doppler-mode[12] observations, where the length of the scan is

[12] In the Doppler mode the telescopes observe in a dual S/X-band (2/8.4 GHz) frequency setup, pointing iteratively at the spacecraft for 20 minutes and then 2 minutes at the calibrator, as explained in Duev et al. [11].

Table 1: Thermal noise of X-band Doppler detections of the VLBI stations during the GR035 experiment.

Observatories	Location	Telescope Code	Telescope Diameter (m)	Average T_{sys} (K)	SEFD Jy	Allan Deviation at 10 s
DSN Goldstone	USA	DSS-14	70	20.6**	20**	6.5×10^{-15}***
DSN Robledo	Spain	DSS-63	70	20.6**	20**	6.5×10^{-15}***
Estrack New Norcia	Australia	NNO	35	60.8**	40**	6.5×10^{-15}***
Yebes	Spain	Ys	40	41	200	5.6×10^{-15}
Onsala	Sweden	On-60	20	62	1240	9.5×10^{-15}
Svetloe	Russia	Sv	32	58*	200*	1.1×10^{-14}
Zelenchukskaya	Russia	Zc	32	30*	200*	5.8×10^{-15}
Badary	Russia	Bd	32	27*	200*	8.2×10^{-15}
Hartebeesthoek	South Africa	Hh Ht	26 15	70 44	875 1260	8.3×10^{-15} 1.0×10^{-14}
Tianma	China	Tm65 (T6)	65	26	48*	4.6×10^{-15}
Urumuqi	China	Ur	25	86	350*	1.2×10^{-14}
Sheshan	China	Sh	25	32	800*	8.6×10^{-15}
Yamaguchi	Japan	Ym	32	50*	106*	8.9×10^{-15}
Hobart	Australia	Ho Hb	26 12	68 87	2500 3500	1.1×10^{-14} 1.5×10^{-14}
Ceduna	Australia	Cd	30	85*	600*	8.1×10^{-15}
Yarragadee	Australia	Yg	12	96	3500	1.6×10^{-14}
Katherine	Australia	Ke	12	112	3500	1.5×10^{-14}
Warkworth	New Zealand	Ww	12	94	3500	1.6×10^{-14}
VLBA Owens Valley	USA	Ov	25	35	300	8.5×10^{-15}
VLBA Kitt Peak	USA	Kp	25	36	310	6.2×10^{-15}
VLBA Hancock	USA	Hn	25	49	419	7.0×10^{-15}
VLBA Brewster	USA	Br	25	41	352	2.5×10^{-14}
VLBA Mauna Kea	USA	Mk	25	43	368	9.9×10^{-15}
VLBA St Croix	USA	Sc	25	39	330	9.4×10^{-15}
VLBA Pie Town	USA	Pt	25	27	313	7.1×10^{-14}
VLBA Fort Davis	USA	Fd	25	36	309	6.2×10^{-15}

*Nominal values taken from the EVN status table II [8].
** Nominal values taken from Stelzried et al. [44] and Martin & Warhaut [30].
*** Assuming a nominal value of the suppressed modulation carrier-to-noise ratio (CNR) of 67 dBHz.

typically > 10 minutes. For instance, considering the Doppler-mode observations of Hartebeesthoek 15 m antenna, the plasma phase scintillation noise can be characterized. Figures 4 and 5 show the spectral power density of the phase fluctuations of MEX signal in S and X band, respectively. The lower and upper limits of the scintillation band are determined by visual inspection, taking into account the cutoff frequency defined to perform the polynomial fit and amount of fluctuation due to the receiver system noise. The phase scintillation indices obtained with the S- and X-band signal, 0.070 rad and 0.073 rad, correspond to the results for Mars-to-Earth total electron content (TEC) along the line of sight found by Molera-Calvés et al. [34], where the dependence of the interplanetary phase scintillation on elongation was studied using various MEX observations. When comparing Figures 4 and 5, it is noticeable that in the spectral power, the noise band in the S band is much higher than in the X band. This is due to the higher thermal noise of the receiver and larger presence of RFI in this band.

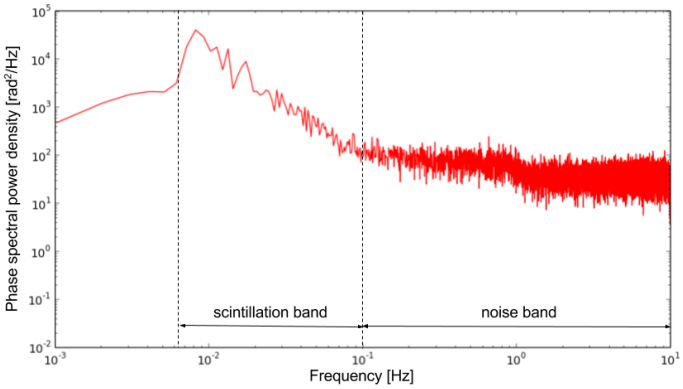

Figure 4: Spectral power density of MEX signal in S band measured by Hartebeesthoek. The scintillation band extends from 8 mHz to 0.1 Hz, obtaining a value for the slope of -2.471, which is coherent with the spectral index values found by [54]. The mean phase scintillation index of the signal received from 3h56m to 09h12m (UTC) on 2013-12-29, is 0.070 rad, at an elongation of $\sim 87^{\circ}$ and distance of ~ 1.4 AU.

Figure 6 shows the spectral power density of ϕ_{Δ} for Ht. The slope found for the scintillation band that extends from 8 mHz to 0.1 Hz is -2.372 with a mean scintillation index of 0.069 rad. These results are in agreement with Molera-Calvés et al. [35]. As the phase power spectrum can be described in the form $S_{\phi}(f) = Af^{-m}$, following Equation 19 the Allan variance of the plasma phase scintillation is 2.46×10^{-15} at τ =1000 s at $\sim 87^{\circ}$ elongation (4.44×10^{-14} at τ =10 s).

More information regarding the origin of the phase fluctuations can be derived by analyzing the spatial statistics of the phase scintillation in multiple stations during the same tracking session. If the ϕ_{Δ} phase data of a few pairs of widely spaced stations are cross-correlated, as suggested in Armstrong [1], it could be determined whether the main contributor to the phase fluctuations is the interplanetary medium or the local impact of the ionosphere at each station. Unfortunately, in the GR035 experiment this analysis could not be performed, since although the three stations operating in Doppler mode are widely spaced (South Africa, Finland, and China), the differential phase ϕ_{Δ} could not be successfully retrieved because of the high RFI on

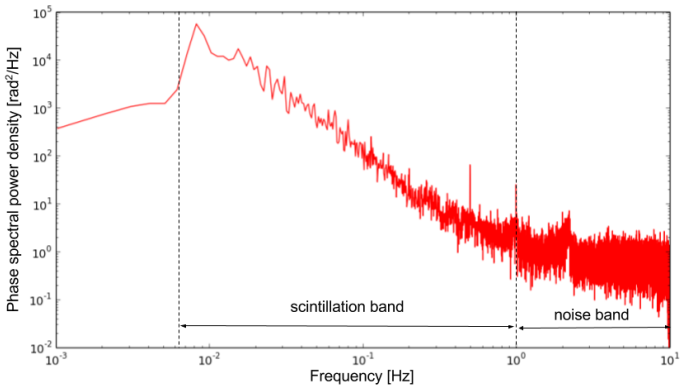

Figure 5: Spectral power density of MEX signal in X band measured by Hartebeesthoek. The scintillation band extends from 8 mHz to 0.45 Hz, obtaining a value for the slope of -2.469. The mean phase scintillation index of the signal received from 3h56m to 09h12m (UTC) on 2013-12-29 is 0.073 rad at an elongation of $\sim 87^\circ$ and distance of ~ 1.4 AU.

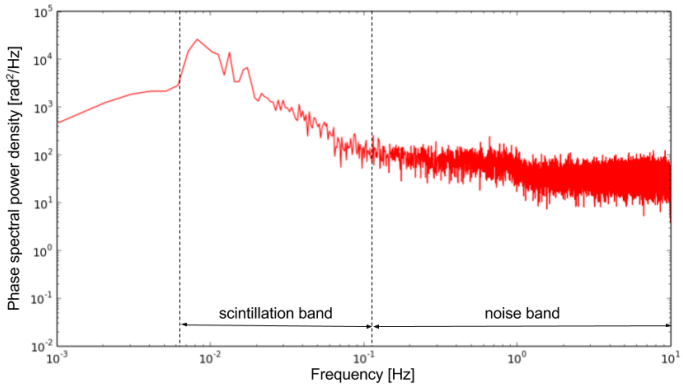

Figure 6: Spectral power density of the differential phases ϕ_Δ measured by Hartebeesthoek. The scintillation band extends from 8 mHz to 0.1 Hz, obtaining a value for the slope of -2.372. The mean phase scintillation index of the signal received from 3h56m to 09h12m (UTC) on 2013-12-29 is 0.069 rad at an elongation of $\sim 87^\circ$ and distance of ~ 1.4 AU.

the S band of Sh and technical problems with the X-band receiver of Mh (for this reason the values for Mh are not shown in Table 1).

3.3. Noise budget for the Doppler detections of GR035

Table 2 summarizes the Allan deviations found for the different noise sources described in Sections 3.1 and 3.2. The Allan deviations from the thermal noise of the ground station for the VLBI stations vary from 0.46×10^{-14} to 1.60×10^{-14} at $\tau = 10$ s. Despite the differences of the thermal noise σ_y between the VLBI stations and the DSN and NNO stations [13], the thermal noise of the stations does not dominate the error budget of the observations in this experiment, as shown in Table 2. Because of the long tracking sessions of the antennas during this experiment, the antenna elevations have a higher impact in the S/N of the detections than the collecting area of the antennas. This issue is usually ignored in shorter tracking sessions, since only stations with elevations $\sim> 20$ deg are selected to participate in an observation.

The plasma scintillation noise was estimated for Ht, which was one of the stations observing both in S and X band. The plasma scintillation noise is more dominant for Ht than its thermal noise ($\sigma_y = 4.44\times10^{-14}$ against $\sigma_y = 1.0\times10^{-14}$ for $\tau = 10$ s). Owing to problems with the receivers, this analysis could not be performed for the other two stations receiving the dual-band link. In future experiments, the contributions of the ionosphere and interplanetary medium could be discerned from one another by correlating the power spectra of the differential phases between every pair of stations.

Table 2: Noise budget for PRIDE GR035 experiment.

Noise source	Allan deviation at τ=10 s	Comments
Ground station thermal noise	$0.5 - 1.5 \times 10^{-14}$	For various sizes of antenna dishes (see Table 1).
Ground frequency reference source	$< 5.0 \times 10^{-14}$	Tjoelker [49]
Plasma phase scintillation	4.44×10^{-14}	For Ht, at a solar elongation of $87°$.
Antenna mechanical noise	–	Has not been determined in this experiment.

Armstrong et al. [2] reported that for the DSN stations, when the propagation noises are properly calibrated, the antenna mechanical noise was the leading noise of their noise budget. Regarding the VLBI stations, Sarti et al. [41, 42] have reported one-way path delay variations caused by antenna mechanical noise, however these were computed for VLBI geodetic and astrometric studies, for which the delay stability is evaluated in annual timescales, which is much larger than the integration times relevant for the study at hand. Nonetheless, owing to their size [4], the expected mechanical noise of the VLBI antennas (except for Tm65) will be considerably less than the 70 m DSN antennas. In fact, simultaneous observations between PRIDE and DSN stations could help improve the sensitivity of the 70 m DSN antennas. Following the approach presented in Armstrong et al. [2] in future experiments, stations of the

[13] The Allan deviations for the DSN and NNO stations were calculated assuming an expected CNR suppressed modulation of 67 dB/Hz, as given in the level 1 data.

global VLBI network close to the deep space tracking complexes could be used to remove the antenna mechanical noise of the larger antennas during simultaneous two- and three-way Doppler passes, for instance, the 2 -m VLBA-Ov close the DSS-14, the 14 m Ys close to the DSS-63, the 12 m Ye telescope close to NNO, and the 12 m Atacama Pathfinder Experiment (APEX) telescope close to Estrack's Malargüe station.

4. Conclusions

With the PRIDE setup, Doppler tracking of the spacecraft carrier signal with several Earth-based radio telescopes is performed, subsequently correlating the signals coming from the different telescopes in a VLBI-style. Although the main output of this technique are VLBI observables, we demonstrated that the residual frequencies obtained from the open-loop Doppler observables–which are inherently derived in the data processing pipeline to retrieve the VLBI observables–are comparable to those obtained with the closed-loop Doppler data from NNO, DSS-63, and DSS-14 stations (see Figure 2). Figure 2 shows the best case found, where the median value of the residuals fit achieved with VLBI station Kp remains within 1 mHz of the residuals fit obtained with DSS-63 and DSS-14. The median of the Doppler residuals for all the detections with the VLBI stations was found to be $\sim$ 2 mHz (which translates into $0.5 \cdot c \cdot (f_{residuals}/f_0) = 36 \mu m/s$ in linear measure for the three-way Doppler in X-band).

The fact that this experiment involved long tracking sessions makes the variability of the elevation angle of the antennas a factor in the characterization of the noise that cannot be ignored. At elevations < 20 degrees, noise contributions due to larger tropospheric path delays and larger spillover noise have a larger impact on the total system temperature compared to those of the receiver temperature. For this reason, there are cases for which antennas with smaller collecting areas reach similar S/N levels as larger antenna dishes, as shown in Figure 3, due to a more favorable antenna elevation. The derived Allan deviations due to thermal noise at the VLBI stations vary between 0.46×10^{-14} to 1.60×10^{-14} at $\tau = 10$ s. For this particular experiment, at the DSN stations the expected $\sigma_y(\tau)$ from thermal noise was 6.5×10^{-15}at τ=10 s. Although only four of the VLBI stations have comparable Allan deviations (Table 1) to those of the DSN stations, the thermal noise is not the most dominant contribution to the overall noise budget of this experiment.

Although they were not included in this particular experiment (other than the 65 m Tianma station), PRIDE has access through the EVN to multiple radio telescopes that are similiar in size or larger than the DSN antennas; these include the 64 m Sardinia, 100 m Effelsberg, and 305 m Arecibo, which can be scheduled for radio science experiments. The use of these large antennas can result in an advantage when conducting experiments with limited S/N, such as radio occultation experiments of planets and moons with thick atmospheres.

Open-loop Doppler data, such as those collected with PRIDE experiments, present advantages for certain radio science applications compared to closed-loop data. However, closed-loop Doppler tracking is routinely performed in the framework of navigation tracking and does not require post-processing to retrieve the Doppler observables. Although the Estrack/DSN complexes have the capability of simultaneously

gathering closed-loop and open-loop Doppler data, this is not an operational mode required for navigation nor telemetry passes, which generally operate in closed-loop mode only. In this sense, PRIDE Doppler data could complement the closed-loop tracking data and enhance the science return of tracking passes that are not initially designed for radio science experiments.

5. Acknowledgements

The EVN is a joint facility of European, Chinese, South African, and other radio astronomy institutes funded by their national research councils. The National Radio Astronomy Observatory is a facility of the National Science Foundation operated under cooperative agreement by Associated Universities, Inc. The Australia Telescope Compact Array is part of the Australia Telescope National Facility, which is funded by the Commonwealth of Australia for operation as a National Facility managed by CSIRO. T. Bocanegra Bahamon acknowledges the NWO–ShAO agreement on collaboration in VLBI. G. Cimó acknowledges the EC FP7 project ESPaCE (grant agreement 263466). P. Rosenblatt is financially supported by the Belgian PRODEX program managed by the European Space Agency in collaboration with the Belgian Federal Science Policy Office.

We express gratitude to M. Pätzold (MEX MaRS PI) and B. Häusler for coordination of MaRS and PRIDE tracking during the MEX/Phobos flyby and a number of valuable comments on the manuscript of the current paper. Mars Express was a mission of the European Space Agency. The MEX a priori orbit, Estrack and DSN tracking stations transmission frequencies, and the cyclogram of events were supplied by the Mars Express project. The authors would like to thank the personnel of the participating stations. R.M. Campbell, A. Keimpema, P. Boven (JIVE), O. Witasse (ESA/ESTEC), and D. Titov (ESA/ESTEC) provided important support to various components of the project.

The authors are grateful to the anonymous referee for useful comments and suggestions.

References

[1] Armstrong, J. 1998, Radio Science, 33, 1727

[2] Armstrong, J., Estabrook, F., Asmar, S., Iess, L., & Tortora, P. 2008, Radio Science, 43

[3] Armstrong, J., Woo, R., & Estabrook, F. 1979, The Astrophysical Journal, 230, 570

[4] Armstrong, J. W. 2016, Living Rev. Relativity, 9, E2

[5] Asmar, S., Armstrong, J., Iess, L., & Tortora, P. 2005, Radio Science, 40

[6] Barnes, J. A., Chi, A. R., Cutler, L. S., et al. 1971, Instrumentation and Measurement, IEEE transactions on, 1001, 105

[7] Boehm, J., Werl, B., & Schuh, H. 2006, J. Geophys. Res., 111, B02406, doi:10.1029/2005JB003629

[8] Campbell, Robert. 2018, http://www.evlbi.org/user_guide/EVNstatus.txt, EVN status table II. Accessed on March 7 2018

[9] Chicarro, A., Martin, P., & Trautner, R. 2004, in Mars Express: The Scientific Payload, Vol. 1240, 3–13

[10] Duev, D. A., Calvés, G. M., Pogrebenko, S. V., et al. 2012, Astronomy & Astrophysics, 541, A43

[11] Duev, D. A., Pogrebenko, S. V., Cimò, G., et al. 2016, Astronomy & Astrophysics, 593, A34

[12] Duev, D. A., Pogrebenko, S. V., & Molera-Calvés, G. 2011, Astronomy Reports, 55, 1008

[13] Feltens, J. & Schaer, S. 1998, in Proceedings of the IGS AC Workshop, Darmstadt, Germany

[14] Gupta, S. C. 1975, Proceedings of the IEEE, 63, 291

[15] Hagermann, A. & Pätzold, M. 2009, Mars Express Orbiter Radio Science MaRS: Flight Operations Manual-Experiment User Manual, Tech. Rep. MEX-MRS-IGM-MA-3008, European Space Agency

[16] Häusler, B., Pätzold, M., Tyler, G., et al. 2006, Planetary and Space Science, 54, 1315

[17] Howard, H., Eshleman, V., Hinson, D., et al. 1992, in The Galileo Mission (Springer), 565–590

[18] Iess, L., Asmar, S., & Tortora, P. 2009, Acta Astronautica, 65, 666

[19] Iess, L., Di Benedetto, M., James, N., et al. 2014, Acta Astronautica, 94, 699

[20] Jenkins, J. M., Steffes, P. G., Hinson, D. P., Twicken, J. D., & Tyler, G. L. 1994, Icarus, 110, 79

[21] Jian, N., Shang, K., Zhang, S., et al. 2009, Science in China Series G: Physics, Mechanics and Astronomy, 52, 1849

[22] Kinman, P. 2003, DSMS Telecommunications Link Design Handbook (810-005, Rev. E), 207A

[23] Kliore, AJ and Anderson, JD and Armstrong, JW and Asmar, SW and Hamilton, CL and Rappaport, NJ and Wahlquist, HD and Ambrosini, R and Flasar, FM and French, RG and others. 2004, in The Cassini-Huygens Mission (Springer), 1–70

[24] Kopeikin, S. M. & Schäfer, G. 1999, Physical Review D, 60, 124002

[25] Kwok, A. 2010, DSMS Telecommunications Link Design Handbook (810-005, Rev. E), 209A

[26] Levy, G. 1977, Mariner Venus Mercury 1973 S/X-band Experiment. JPL Publication 77-17, Tech. rep., Jet Propulsion Laboratory, California Institute of Technology

[27] Lindqvist, M. & Szomoru, A. 2014, in Proceedings of the 12th European VLBI Network Symposium and Users Meeting

[28] Lipa, B. & Tyler, G. L. 1979, Icarus, 39, 192

[29] Marouf, E. A., Tyler, G. L., & Rosen, P. A. 1986, Icarus, 68, 120

[30] Martin, R. & Warhaut, M. 2004, in Aerospace Conference, 2004. Proceedings. 2004 IEEE, Vol. 2, IEEE, 1124–1133

[31] Martin-Mur, T., Antresian, P., Border, J., et al. 2006, Proceedings 25th International Symposium Space Technol. Sci.

[32] Mazarico, E., Rowlands, D., Neumann, G., et al. 2012, Journal of Geodesy, 86, 193

[33] Molera Calvés, G. 2012, PhD thesis, Aalto University, Finland

[34] Molera-Calvés, G., Kallio, E., Cimo, G., et al. 2017, Space Weather, 15, 1523

[35] Molera-Calvés, G., Pogrebenko, S., Cimò, G., et al. 2014, Astronomy & Astrophysics, 564, A4

[36] Morabito, D. & Asmar, S. 1995, The Telecommunications and Data Acquisition Report, 42, 121

[37] Moyer, T. D. 2005, Formulation for observed and computed values of Deep Space Network data types for navigation, Vol. 3 (John Wiley & Sons)

[38] Paik, M. & Asmar, S. W. 2011, Proceedings of the IEEE, 99, 881

[39] Pätzold, M., Neubauer, F., Carone, L., et al. 2004, in Mars Express: The Scientific Payload, Vol. 1240, 141–163

[40] Rutman, J. & Walls, F. 1991, Proceedings of the IEEE, 79, 952

[41] Sarti, P., Abbondanza, C., Petrov, L., & Negusini, M. 2011, Journal of Geodesy, 85, 1

[42] Sarti, P., Abbondanza, C., & Vittuari, L. 2009, Journal of Geodesy, 83, 1115

[43] Shapiro, I. I., Ash, M. E., Ingalls, R. P., et al. 1971, Physical Review Letters, 26, 1132

[44] Stelzried, C. T., Freiley, A. J., & Reid, M. S. 2008, Low-Noise Systems in the Deep Space Network, MS Reid, Ed. Jet Propulsion Laboratory, 13

[45] Tausworthe, R. C. 1966, Theory and practical design of phase-locked receivers. Technical Report NASA-CR-70395, JPL-TR-32-819, Tech. rep., Jet Propulsion Laboratory, California Institute of Technology

[46] Tellmann, S., Paetzold, M., Haeusler, B., Hinson, D., & Tyler, G. L. 2013, Journal of Geophysical Research: Planets, 118, 306

[47] Tellmann, S., Pätzold, M., Häusler, B., Bird, M. K., & Tyler, G. L. 2009, Journal of Geophysical Research: Planets, 114

[48] Thornton, C. L. & Border, J. S. 2003, Radiometric tracking techniques for deep-space navigation (John Wiley & Sons)

[49] Tjoelker, R. 2010, DSN Telecommunications Link Design Handbook (810-005, Rev. A), 304

[50] Tortora, P., Iess, L., & Ekelund, J. 2002, in IAF abstracts, 34th COSPAR Scientific Assembly

[51] Tyler, G., Sweetnam, D., Anderson, J., et al. 1989, Science, 246, 1466

[52] Vig, J. R., Ferre-Pikal, E. S., Camparo, J. C., et al. 1999, IEEE Standard, 1139, 1999

[53] Witasse, O., Lebreton, J.-P., Bird, M. K., et al. 2006, Journal of Geophysical Research (Planets), 111, 7

[54] Woo, R. & Armstrong, J. 1979, Journal of Geophysical Research: Space Physics, 84, 7288

CHAPTER 5

Radio occultation experiments with PRIDE

In Chapter 4 the performance of the Doppler component of the PRIDE technique was evaluated. It was demonstrated that PRIDE can provide open-loop Doppler observables with similar spectral resolutions (~2 mHz at 10 s integration time) as for the closed-loop Doppler observables obtained with the DSN and Estrack tracking stations. In this chapter, we will evaluate the performance of the Doppler component of PRIDE for extreme scenarios of very low SNR and high dynamics of the carrier signal. Such scenario is the one encountered in a radio occultation experiment. In this case, the spacecraft carrier signal will be refracted through the target planet's atmosphere, as the spacecraft gets occulted by the planet with respect to the line-of-sight of the receiving antennas. This technique has been widely used in multiple space missions in order to characterize planetary atmospheres. In this chapter we discuss the implementation of the processing methodology to be able to process radio occultation observations with PRIDE. We will demonstrate that, in its current state, the PRIDE technique can be used to probe thick planetary atmospheres. For this purpose we performed multiple radio occultation observations of ESA's Venus Express (VEX) orbiter. The derived atmospheric profiles and their corresponding error propagation analysis show high level of consistency with the results obtained with ESA's Estrack New Norcia station. This chapter addresses research questions 2, 3 and 4.

Venus Express radio occultation observed by PRIDE

T. M. Bocanegra-Bahamón[1,2,3], *G. Molera Calvés*[1,4], *L.I. Gurvits*[1,2], *G. Cimò*[1,5], *D. Dirkx*[2], *D.A. Duev*[6], *S.V. Pogrebenko*[1], *P. Rosenblatt*[7], *S. Limaye*[8], *L. Cui*[9], *P. Li*[9], *T. Kondo*[10,3], *M. Sekido*[10], *A.G. Mikhailov*[11],*M.A. Kharinov*[11],*A.V. Ipatov*[11], *W. Wang*[3],*W. Zheng*[3], *M. Ma*[3], *J.E.J. Lovell*[12], *J.N. McCallum*[12]

Accepted to *Astronomy & Astrophysics*, 2018

Abstract

Context. Radio occultation is a technique used to study planetary atmospheres by means of the refraction and absorption of a spacecraft carrier signal through the atmosphere of the celestial body of interest, as detected from a ground station on Earth. This technique is usually employed by the deep space tracking and communication facilities (*e.g.,* NASA's Deep Space Network (DSN), ESA's Estrack). *Aims*. We want to characterize the capabilities of the Planetary Radio Interferometry and Doppler Experiment (PRIDE) technique for radio occultation experiments, using radio telescopes equipped with Very Long Baseline Interferometry (VLBI) instrumentation. *Methods*. We conducted a test with ESA's Venus Express (VEX), to evaluate the performance of the PRIDE technique for this particular application. We explain in detail the data processing pipeline of radio occultation experiments with PRIDE, based on the collection of so-called open-loop Doppler data with VLBI stations, and perform an error propagation analysis of the technique. *Results*. With the VEX test case and the corresponding error analysis, we demonstrated that the PRIDE setup and processing pipeline is suited for radio occultation experiments of planetary bodies. The noise budget of the open-loop Doppler data collected with PRIDE indicated that the uncertainties in the derived density and temperature profiles remain within the range of uncertainties reported in previous Venus' studies. Open-loop Doppler data can probe deeper layers of thick atmospheres, such as that of Venus, compared to closed-loop Doppler data. Furthermore, PRIDE through the VLBI networks around the world, provides a wide coverage and range of large antenna dishes, that can be used for this type of experiments.

1: Joint Institute for VLBI ERIC, The Netherlands
2: Delft University of Technology, The Netherlands
3: Shanghai Astronomical Observatory, China
4: Finnish Geospatial Research Institute, Finland
5: Netherlands Institute for Radio Astronomy, The Netherlands
6: California Institute of Technology, USA
7: ACRI-ST, France
8: University of Wisconsin, USA
9: Xinjiang Astronomical Observatory, China
10: NICT Kashima Space Technology Center, Japan
11: Institute of Applied Astronomy of Russian Academy of Sciences, Russia
12: University of Tasmania, Australia

1. Introduction

The Planetary Radio Interferometry and Doppler Experiment (PRIDE) is a technique based on the adaptation of the traditional far-field Very Long Baseline Interferometry (VLBI) astrometric technique applied to near-field targets - spacecraft inside the Solar System - with the main objective of providing precise estimates of the spacecraft state vectors. This is achieved by performing precise Doppler tracking of the spacecraft carrier signal and near-field VLBI observations in phase-referencing mode [6, 13, 14]. PRIDE is suitable for various applications in planetary and space science, such as determination of planetary ephemerides [12], characterization of the interplanetary plasma [46] and detection of Interplanetary Coronal Mass Ejection (ICME) [45]. In this work we present another application: the characterization of planetary atmospheres and/or ionospheres by means of radio occultation observations.

The implementation and application of radio occultation experiments to planetary science has been widely discussed in literature [*e.g.* 16, 17, 30, 47, 50, 55, 60, 62]. A planetary radio occultation experiment involves a 'central' body (a planet or a natural satellite), the atmosphere (or ionosphere) of which is to be studied, and two radio elements: a transmitter onboard a spacecraft orbiting (or performing a flyby about) the central body and, one or multiple ground stations on Earth. At certain geometries, the spacecraft gets occulted by the central body with respect to the line of sight of the receiving ground station. As the spacecraft gets gradually occulted by the central body, the spacecraft carrier signal cuts through successively deeper layers of the planet's atmosphere, experiencing changes in its frequency and amplitude before being completely blocked by the body. This phase is known as ingress. Then the same phenomena is observed as the signal emerges from behind the body. This phase is known as egress. The refraction that the signal undergoes due to the presence of the atmosphere can be determined from the frequency shift observed throughout the occultation event. In addition to this, accurate estimates of the spacecraft state vector are needed to obtain the refractivity as a function of the radius from the occultation geometry. In the case of PRIDE, the receiving element is not a single station but a network of Earth-based radio telescopes. PRIDE provides multiple single-dish Doppler observables that are utilized to derive the residual frequencies of the spacecraft carrier signal, and additionally interferometry observables that are used, along with the Doppler observables, as input to determine the spacecraft state vector. The final product of this experiment is the derivation of vertical density, pressure and temperature profiles of the central body's atmosphere.

The purpose of this paper is to evaluate the performance of the PRIDE setup for radio occultation experiments of planetary atmospheres. We note that the radio occultation technique can be productive for studies of atmosphereless celestial bodies as well (*e.g.*, the Moon, Saturn's rings), enabling the characterization of the shape of the occulting body. However, we do not discuss this application here. As a test case, we analyze several observations of ESA's Venus Express (VEX) spacecraft using multiple radio telescopes from the European VLBI Network (EVN), AuScope VLBI array (Australia) and NICT (Japan), during April 2012, May 2012 and March 2014. The VEX orbiter was launched in 2005.11.09, arriving at Venus in April 2006 and remained in orbit around the planet until end of 2014. The operational orbit of the spacecraft was a highly elliptical ($e = 0.99$), quasi-polar orbit ($i = \sim 90^\circ$) with a ~24-hour orbital period and a pericenter altitude of 250 km. The radio science operations and analy-

sis were led by the Venus Express radio science team (VeRa) [22]. The spacecraft, equipped with an onboard ultra-stable oscillator (USO) as frequency reference, conducted all radio occultation experiments in a one-way mode, transmitting coherent dual-frequency carrier downlinks at X-band (8.4 GHz) and S-band (2.3 GHz) with the main 1.3 m high gain antenna (HGA1). The nominal mission receiving ground station during radio occultation observations was the 35-m Estrack New Norcia (NNO) station located in Western Australia.

Besides VEX, Venus' atmosphere and ionosphere has been studied with ground- and space-based telescopes, and multiple spacecraft using a variety of techniques [9, 18, 42]. Using the planetary radio occultation technique, Venus' atmospheric and ionospheric density profiles have been derived from observations of NASA's Mariner 5 [17, 33, 44], Mariner 10 [28], Venera 9 and 10 [39, 58], Venera 15 and 16 [21, 61], Pioneer Venus Orbiter (PVO) [34–38], Magellan [27, 30, 53], ESA's VEX [20, 47–49, 54, 55] and recently with JAXA's Akatsuki [2, 29]. The composition of Venus' ionosphere is primarily O_2^+ and smaller amounts of CO_2^+, O^+ and other trace species [20]. Although radio occultation experiments cannot be used to determine the specific composition of the ionosphere, the radio waves are sensitive to the electron distribution and therefore density profiles of the ionospheric plasma can be derived down to ∼100 km. Similarly, for Venus' neutral atmosphere density and temperature profiles can be derived assuming the composition of the atmosphere (96.5% CO_2, 3.5% N_2) [35, 52]. In the case of Venus' atmosphere, radio occultation data provide a vertical coverage of ∼40-100 km in altitude. This technique is the only remote sensing method that can probe Venus' atmosphere at altitudes below ∼65 km [42].

In this paper we present the results of VEX occultation observations obtained with radio telescopes equipped with VLBI data acquisition instrumentation. We explain the processing pipeline carried out with the PRIDE setup and present the corresponding error propagation analysis. Sections 2.1 and 2.2 present the theoretical background of the radio occultation method and the approximations taken into account when formulating the observation model. Section 2.3 shows the theoretical derivation of the atmospheric profiles from the carrier signal frequency residuals. Section 3 presents the overall description of the experiment and the results found. Section 3.1 describes the setup of the experiment, describing the observations used and the data processing pipeline. Section 3.2 present the resulting Venus' atmospheric profiles using the PRIDE setup. Section 3.3 presents the error propagation analysis, through the processing pipeline, from the Doppler observables to the derived atmospheric properties. Section 4 presents the conclusions of this technology demonstration.

2. The radio occultation experiment

In a radio occultation experiment, the carrier signal of the spacecraft experiences refraction, absorption and scattering as it passes behind the visible limb of the planetary body due to its propagation through the planet's atmosphere on its way to the receiving ground station on Earth. The physical properties of the planetary atmosphere can be inferred by analyzing the changes in frequency and amplitude of the received carrier signal.

2.1. Theoretical background and approximations

During the occultation event, the spacecraft carrier signal propagates through the atmosphere of the celestial body, experiencing a modulation of phase and a decrease in amplitude. The variation in phase is proportional to the real part of the medium's complex refractive index and the decrease in amplitude is proportional to the imaginary part of the medium's complex refractive index, also known as absorption factor [15]. These refractive and absorptive radio effects are caused by the presence of neutral gases and plasma in the atmosphere and ionosphere. In the study at hand, only the frequency changes in the carrier signal are analyzed. Therefore, the amplitude data from which absorptivity profiles are derived, are not treated in this paper.

As the spacecraft signal gets refracted crossing the different layers of the planet's atmosphere, the variation of the real part of complex refractive index (treated simply as the refractive index in the remainder of this paper) as a function of altitude can be determined, for a particular cross section of the atmosphere. Before establishing the relation between the frequency changes of the received carrier signal and the planet's atmospheric refractive index as a function of altitude, let us consider some approximations that simplify the models used to relate these quantities.

As for most planets, the variations in the electrical properties of Venus' atmosphere occur at scales much larger than the spacecraft signal wavelength [17]. Hence, the radio wave can be treated as a light ray and its trajectory can be determined by geometric optics. As in previous radio occultation experiments of Venus, such as Fjeldbo et al. [17], Jenkins et al. [30], Tellmann et al. [54], we assume the planet's atmosphere can be modeled as a spherically symmetric medium, made of concentric shells, each of them with a constant refractive index. From geometric optics the propagation path of the signal can be described as a ray $\mathbf{r}(s)$ parameterized by an arclength s that satisfies the following differential equation [8],

$$\frac{d}{ds}\left(n\frac{d\mathbf{r}}{ds}\right) = \nabla n \tag{1}$$

where $n(\mathbf{r})$ is the refractive index, which for the case of spherical symmetry is a function of radial distance only. Hence, the ray trajectory, as it bends through the medium, can be traced given the medium refractive index as a function of the radius. This is known as the forward problem. However, we are interested in the inverse problem, where based on the ray path parameters, -the bending angle and the impact parameter-, the refractivity of profile of the atmosphere is retrieved.

2.2. Observation model

In the radio domain the bending that the signal undergoes as it crosses the planet's ionosphere and neutral atmosphere cannot be measured directly. However, it can be retrieved from the frequency shift experienced by the received signal at the ground stations. In this section, we will first introduce the relation between the frequency shift and the ray parameters of the received signal, to then establish the relation between ray parameters and refractive index as a function of radius.

Observation geometry

The geometry of the occultation is determined by the occultation plane (*i.e.*, the plane defined by the center of the target planet, the position of tracking station and

the position of the spacecraft, each with respect to the target planet) as shown in Figure 1. The reference frame used has its origin at the center of mass of the target planet, with the negative z-axis pointing to the position of the tracking station at reception time, the n-axis parallel to the normal of the occultation plane and the r-axis perpendicular to both the z- and n- axis. In this scenario, the target body is assumed to have a spherically symmetric and stationary atmosphere and the ray path refraction occurs on the occultation plane, reducing it to a two-dimensional problem as shown in Figure 2. The bending of the refracted ray path is then parameterized with respect to the free-space ray path by means of the angles δ_r and β_r. The angle δ_r is defined between the position vector of the spacecraft at transmission time with respect to the tracking station at reception time and the ray path asymptote in the direction the radio wave is received at the tracking station at reception time. The angle β_r is defined between the position vector of the tracking station at reception time with respect to the spacecraft at transmission time and the ray path asymptote in the direction the radio wave is transmitted by the spacecraft at transmission time (see Figure 2).

This description of the occultation geometry is based on Fjeldbo et al. [17], where the approach that will be discussed in this section was first introduced. Multiple authors have expanded on this approach [*e.g.,* 30, 43, 60] including the relativistic corrections into the analysis.

Derivation of the ray path parameters from the carrier signal frequency residuals

To isolate the perturbation that the spacecraft signal experiences when propagating through the media along the radio path, we evaluate the difference between the detected carrier frequency and the prediction of the received frequency at the ground station, assuming for the latter that the signal is propagating through free-space (including geometrical effects, such as relative position and motion between the spacecraft and ground station, Earth rotation and relativistic corrections). If perturbations due to the signal propagation through the Earth's atmosphere, ionosphere and interplanetary medium are accounted for, then the remaining observed perturbation is solely due to the atmosphere and ionosphere of the planet of interest.

As shown by Kopeikin & Schäfer [40, Eq. 266], the frequency received at a tracking station on Earth f_R at a reception time t_R is given by,

$$f_R = f_T \frac{1 - \mathbf{k}_R \cdot \mathbf{v}_R/c}{1 - \mathbf{k}_T \cdot \mathbf{v}_T/c} R(\mathbf{v_R}, \mathbf{v_T}, \mathbf{t_R}, \mathbf{t_T}) \tag{2}$$

where c is the free-space velocity of light, f_T is the spacecraft transmission frequency at the transmission time t_T, $\mathbf{v}_R$ and $\mathbf{v}_T$ are the barycentric velocity vectors of the receiving station at t_R and of the spacecraft at t_T, respectively, $\mathbf{k}_R$ and $\mathbf{k}_T$ are the unit tangent vectors in the direction along which the radio wave propagates at t_T and t_R, respectively, and the term R gives the special and general relativistic corrections:

$$R(v_R, v_T, t_R, t_T) = \left[\frac{1 - (v_T/c)^2}{1 - (v_R/c)^2}\right]^{1/2} \left[\frac{a(t_T)}{a(t_R)}\right]^{1/2} \frac{b(t_R)}{b(t_T)} \tag{3}$$

where the terms a and b are derived as explained in Section 4.2.2 (Eqs. 12 and 13

in Chapter 4). All position and velocity vectors are expressed in the solar system barycentric frame.

The frequency residuals are subsequently found by evaluating the difference between detected frequency $f_{R,detected}$ and the predicted frequency in free-space $f_{R,free-space}$ received at the ground station at t_R, as follows:

$$\Delta f = f_{R,detected} - f_{R,free-space} \tag{4}$$

assuming that $f_{R,detected}$ has been corrected for the effects of propagation through interplanetary plasma and the Earth's atmosphere and ionosphere.

In the case of free-space, the direction along which the radio signal propagates is the same at t_R and t_T, hence $\mathbf{k}_R = \mathbf{k}_T$ in Eq 2, and $\delta_r = 0$ and $\beta_r = 0$. When the signal gets refracted by the atmosphere of the target planet, $\mathbf{k}_R$ and $\mathbf{k}_T$ become the two ray path asymptotes shown in blue in Figure 2. Hence, the ray path asymptotes for both cases can be defined as follows:

$$-\mathbf{k}_{R,free-space} = \hat{\mathbf{r}} \sin \delta_s + \hat{\mathbf{z}} \cos \delta_s \tag{5}$$

$$-\mathbf{k}_{T,free-space} = \hat{\mathbf{r}} \cos \beta_e + \hat{\mathbf{z}} \sin \beta_e \tag{6}$$

$$-\mathbf{k}_{R,detected} = \hat{\mathbf{r}} \sin (\delta_s - \delta_r) + \hat{\mathbf{z}} \cos (\delta_s - \delta_r) \tag{7}$$

$$-\mathbf{k}_{T,detected} = \hat{\mathbf{r}} \cos (\beta_e - \beta_r) + \hat{\mathbf{z}} \sin (\beta_e - \beta_r) \tag{8}$$

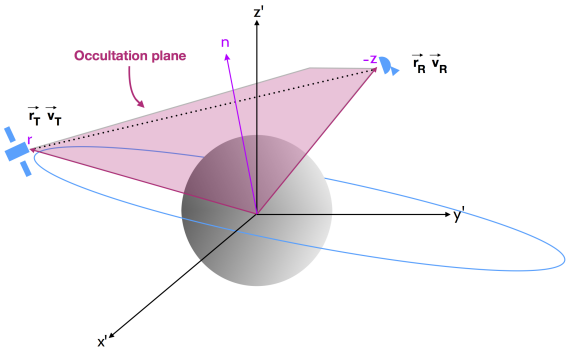

Figure 1: Sketch of the occultation plane. The occultation plane is defined by the center of mass of the target planet, the position of tracking station and the position of the spacecraft, each with respect to the target planet.

Hence, a relation between the frequency residuals and the angles that parameterize the bending of the ray path can be established by replacing Eq. (2) and Eqs. (5) to (8) into Eq. (4),

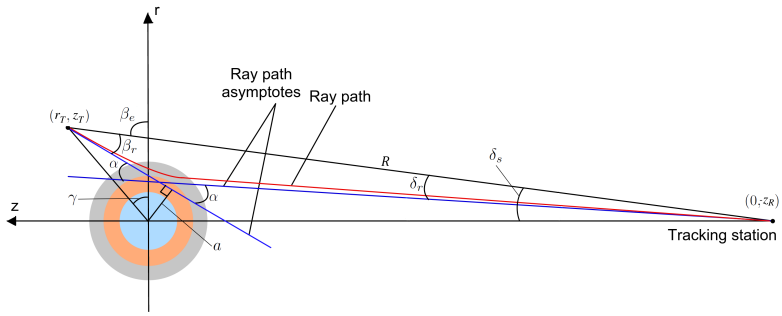

Figure 2: Geometry of the radio occultation depicted on the occultation plane. In this case, the figure shows the ray path as it gets refracted by the planet's ionosphere (in gray), where it gets bent by an angle α from its original path.

$$\Delta f = Rf_T \left(\frac{c + v_{r,R} \sin(\delta_s - \delta_r) + v_{z,R} \cos(\delta_s - \delta_r)}{c + v_{r,T} \cos(\beta_e - \beta_r) + v_{z,T} \sin(\beta_e - \beta_r)} - \frac{c + v_{r,R} \sin \delta_s + v_{z,R} \cos \delta_s}{c + v_{r,T} \cos \beta_e + v_{z,T} \sin \beta_e} \right) \tag{9}$$

where $v_{r,R}$ is the r-component of v_R and $v_{z,R}$ is the z-component of v_R at reception time t_R, $v_{r,T}$ is the r-component of v_T and $v_{z,T}$ is the z-component of v_T at transmission time t_T. The angles β_e and δ_s are defined between the position vector of the spacecraft at t_T with respect to the ground station at t_R, and the r-axis and z-axis, respectively ($\beta_e + \delta_s = \pi/2$).

As a consequence of Eq. (1), the distance a from the planet's center of mass to the tangent at any point along the ray path is a constant a,

$$a = |z_R| \sin(\delta_s - \delta_r) = (r_T^2 + z_T^2)^{1/2} \sin(\beta_e - \gamma - \beta_r) \tag{10}$$

where a is called the ray impact parameter. Eqs. (9) and (10) can be solved simultaneously for the two ray path angles δ_r and β_r - assuming that the state vectors of the spacecraft and tracking station are known - using the numerical technique introduced by Fjeldbo et al. [17]. Once the values of δ_r and β_r are determined, the total bending angle of refraction α of the ray path is obtained by adding them (see Figure 2).

$$\alpha = \delta_r + \beta_r \tag{11}$$

Applying this procedure, for every Δf obtained at each sampled time step (Eq. 4) the corresponding ray path parameters, bending angle α and impact parameter a, are derived. We follow the sign convention adopted by Ahmad & Tyler [1] and Withers [59] where positive bending is considered to be towards the center of the planet.

2.3. Relation to atmospheric properties

In this section we will establish the relations that link the ray path parameters to the physical properties of the layer of the atmosphere the radio signal is sounding.

Following Born & Wolf [8], assuming a radially symmetric atmosphere represented by K concentric spherical layers each with a constant refractive index n, the bending angle α is related to n through an Abel transform:

$$\alpha(a_k) = -2a_k \int_{r=r_k}^{r=\infty} \frac{d\ln(n(r))}{dr} \frac{dr}{\sqrt{(n(r)r)^2 - a_k^2}} \tag{12}$$

where r is the radius from the center of the planet to the ray and the subscripts represent the k-th layer, the deepest layer each ray path reaches, which corresponds to a specific reception time at the receiver.

As explained in Fjeldbo et al. [17], Eq. (12) can be inverted to have an expression for the refractive index n in terms of α and a:

$$\ln n_k(a_k) = \frac{1}{\pi} \int_{a'=a_k}^{a'=\infty} \frac{\alpha(a')da'}{\sqrt{a'^2 - a_k^2}} \tag{13}$$

$$n(r_{0k}) = \exp\left[\frac{1}{\pi}\int_{\alpha'=\alpha(a_k)}^{\alpha'=0} \ln\left[\frac{a(\alpha')}{a_k} + \left[\left(\frac{a(\alpha')}{a_k}\right)^2 - 1\right]^{1/2}\right] d\alpha'\right] \tag{14}$$

Using the total refraction bending angles found as explained in Section 2.2, the refractive index for the k-th layer can be determined by performing the integration over all the layers the ray has crossed:

$$n_k(a_k) = \exp\left\{\frac{1}{\pi}\int_{a_1}^{a_0} \frac{\tilde{\alpha}_1 da'}{\sqrt{a'^2 - a_k^2}} + \ldots + \frac{1}{\pi}\int_{a_k}^{a_{k-1}} \frac{\tilde{\alpha}_k da'}{\sqrt{a'^2 - a_k^2}}\right\} \tag{15}$$

where $\tilde{\alpha}_i$ is the average value of the bending angles α_i in a layer:

$$\tilde{\alpha}_i = \frac{\alpha_i(a_i) + \alpha_{i-1}(a_{i-1})}{2} \text{ with } i = 1\ldots k \tag{16}$$

A ray with impact parameter a will cross the symmetric atmosphere, down to a layer k of radius r_{0k}. This minimum radius is found via the Bouguer's rule, which is the Snell law of refraction for spherical geometries. As explained in Born & Wolf [8] and Kursinski et al. [41], r_{0k} is related to a_k by:

$$r_{0k} = \frac{a_k}{n_k} \tag{17}$$

The refractivity as a function of the radius depends on the local state of the atmosphere. The total refractivity of the atmosphere μ is given by the sum of the components due to the neutral atmosphere and ionosphere. For each layer the total refractivity is given by [15]:

$$\mu_k = (n_k - 1) = \mu_{n,k} + \mu_{e,k} \tag{18}$$

where μ_n is the refractivity of the neutral atmosphere:

$$\mu_n = \kappa N_n \tag{19}$$

where κ is the mean refractive volume and N_n is the neutral number density, and μ_e is the refractivity of the ionosphere:

$$\mu_e = -\frac{N_e e^2}{8\pi^2 m_e \epsilon_0 f^2} \tag{20}$$

where e is the elementary charge, m_e is the electron mass, ϵ_0 is the permittivity of free-space, f is the radio link frequency and N_e is the electron density.

In the ionosphere, the electron density is high and the neutral densities can be several orders of magnitude lower, therefore in the ionosphere μ_e is dominant and μ_n is negligible. On the other hand, at lower altitudes, the situation is the opposite: the neutral densities are high and electron densities are low. Hence in practice, if the value of μ is negative, μ_e is assumed to be equal to μ and if μ is positive, then μ_n is assumed to be equal to μ.

Assuming hydrostatic equilibrium, the vertical structure of the neutral atmosphere can be derived from the neutral density profile $N_n(h)$ and the known constituents of the planetary atmosphere. The pressure in an ideal gas is related to the temperature $T(h)$ and number density of the gas by:

$$p(h) = kN_n(h)T(h) \tag{21}$$

where k is the Boltzmann's constant. Using Eq. (21) and the equation for hydrostatic equilibrium the temperature profile can be found from the following formula [16]:

$$T(h) = T(h_0)\frac{N(h_0)}{N(h)} + \frac{\bar{m}}{kN(h)}\int_h^{h_0} g(h')N(h')dh' \tag{22}$$

where $\bar{m}$ is the mean molecular mass, $g(h)$ is the gravitational acceleration and h_0 is an altitude chosen to be the top of the atmosphere for which the corresponding temperature $T(h_0)$, taken from the planet's reference atmospheric model, is assigned as boundary condition. From Eq.(22) it can be seen that the sensitivity of $T(h)$ to the upper boundary condition $T(h_0)$ rapidly decreases due to the $N(h_0)/N(h)$ factor.

3. PRIDE as an instrument for radio occultation studies: a test case with Venus Express

The PRIDE technique uses precise Doppler tracking of the spacecraft carrier signal at several Earth-based radio telescopes and subsequently performs VLBI-style correlation of these signals in the so-called phase referencing mode [13]. In this way, PRIDE provides open-loop Doppler observables, derived from the detected instantaneous frequency of the spacecraft signal [6], and VLBI observables, derived from the group and phase delay of the spacecraft signal [13], that can be used as input for spacecraft orbit determination and ephemeris generation. During a radio occultation experiment, the Doppler observables are utilized to derive the residual frequencies

of the spacecraft carrier signal. These are subsequently used to derive atmospheric density profiles, as explained in Section 2. Both, the Doppler and VLBI observables, can be used for orbit determination, allowing the accurate estimation of the spacecraft state vectors during the occultation event. In this paper, we will focus on the error propagation in the frequency residuals obtained with the open-loop Doppler observables derived with PRIDE, and will use the VEX navigation post-fit orbits derived by the European Space Operations Center (ESOC)[13], which do not include PRIDE observables, to calculate the spacecraft state vectors in the occultation plane.

3.1. Observations and experimental setup

The current data processing pipeline of the PRIDE radio occultation experiment is represented in Figure 3. The first part of the software comprises three software packages developed to process spacecraft signals (the software spectrometer `SWSpec`, the narrowband signal tracker `SCtracker` and the digital phase-locked loop `PLL`)[46][14] and the software correlator `SFXC` [32] which is able to perform VLBI correlation of radio signals emitted by natural radio sources and spacecraft. These four parts of the processing pipeline are used for every standard PRIDE experiment (yellow blocks in Figure 3). The output at this point are open-loop Doppler and VLBI observables. The methodology behind the derivation of these observables using the aforementioned software packages is explained by Bocanegra-Bahamón et al. [6], Duev et al. [13], Molera-Calvés et al. [46]. The second part of the software was developed for the sole purpose of processing radio occultation experiments. It consists of three main modules: the frequency residuals derivation module, the geometrical optics module and the Abelian integral inversion module. From these three modules the vertical density profiles, and subsequently, temperature and pressure profiles of the target's atmosphere can be derived. The frequency residuals module uses the output of the `PLL` which are the time averaged carrier tone frequencies detected at each telescope. To produce the frequency residuals the predictions of the received carrier signal frequency at each telescope is computed as described in [6], and then the frequency residuals are corrected with a baseline fit to account for the uncertainties in the orbit used to derive the frequency predictions (Section 3.3). In the geometrical optics module the state vectors retrieved from VEX navigation post-fit orbit are transformed into a coordinate system defined by the occultation plane as explained in Section 2, and using the frequency residuals found in the previous step, the bending angle and impact parameter at each sample step is found using Eqs. (9) to (11) using the procedure described in Section 2. The refractivity profile is derived in the Abelian integral inversion module, where the integral transform that relates the bending angle with the refractive index (Eq. 12) is solved by modeling the planet's atmosphere as K concentric spherical layers of constant refractivity and applying Eq. (15), as explained in Section 2. The number of layers and their thickness is defined by the integration time step of the averaged carrier frequency detections. In the atmospheric model, each sample is assumed to correspond to a ray passing tangentially through the middle of the n-th layer, as described in Fjeldbo et al. [17] (Appendix B).

To provide a noise budget of PRIDE for radio occultation experiments we used 5 observation sessions in X-band (8.4 GHz) with Earth-based telescopes between

[13] ftp://ssols01.esac.esa.int/pub/data/ESOC/VEX/
[14] https://bitbucket.org/spacevlbi/

2012.04.27 and 2012.05.01, and one in 2014.03.23, when VEX was occulted by Venus. Table 1 shows a summary of the telescopes involved in the observations and Table 2 shows a summary of the observations and participating telescopes per day. The observations were conducted in three scans[15]: in the first scan the antennas pointing to the spacecraft for 19 minutes up to ingress where there is loss of signal, in the second the antennas pointing to the calibrator source for 4 minutes, and in the third pointing back to the spacecraft starting right before egress for 29 minutes. The exception being the 2014.03.23 session where the ingress and egress were detected in one single scan (no calibrator source was observed in between, because there was no loss of signal throughout the occultation). Figure 4 shows the signal-to-noise ratio (SNR) of the two spacecraft scans, ingress and egress, as recorded by the 32-m Badary telescope on 2012.04.30. Usually, for orbit determination purposes, the part of the scan where the SNR of the detections starts dropping due to the signal refraction in the planet's atmosphere is discarded. However, this is precisely the part of the scan that is of interest for radio occultation experiments. For the case of VEX, during radio occultation sessions the spacecraft was required to perform a slew maneuver to compensate for the severe ray bending due to Venus' thick neutral atmosphere [23].

As explained in Bocanegra-Bahamón et al. [6], when processing the observations a polynomial fit is used to model the moving phase of the spacecraft carrier tone frequencies along the time-integrated spectra per scan. In order to provide an appropriate polynomial fit to the low SNR part of the detection, after running `SWSpec` the scan is split in two parts: right before the signal starts being refracted in the case of the ingress, and right after it stops being refracted in the case of the egress (Figure 4). The initial phase polynomial fit and the subsequent steps with `SCtracker` and `DPLL` are conducted as if they were two separate scans.

Table 1: Summary of the radio telescopes involved in the observations.

Observatory	Country	Telescope	
		Code	Diameter (m)
Sheshan (Shanghai)	China	Sh	25
Nanshan (Urumqi)	China	Ur	25
Tianma	China	T6	65
Badary	Russia	Bd	32
Katherine	Australia	Ke	12
Kashima	Japan	Ks	34

3.2. Derived atmospheric profiles

Figure 5a shows an example of the frequency residuals found for Ur and Sh during ingress for the 2012.04.27 session in comparison with those of NNO, as provided by ESA's Planetary Science Archive (PSA) [16]. From ~19605 s, the signal starts being

[15] A scan is the time slot in which the antenna is pointing to a specific target (*i.e*, a spacecraft or a natural radio source)

[16] `ftp://psa.esac.esa.int/pub/mirror/VENUS-EXPRESS/VRA/`

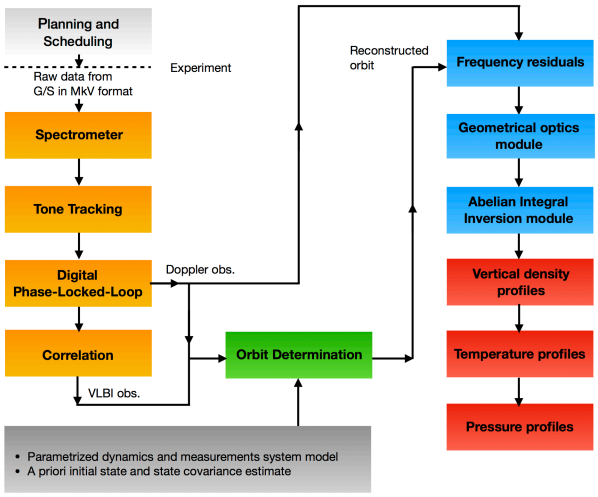

Figure 3: Radio occultation processing pipeline. The first part of the software, which comprises the `SWSpec`, `SCtracker`, `PLL` and `SFXC` correlation software, (in yellow blocks in Figure 3) is used for every standard PRIDE experiment. This part of the processing pipeline gives open-loop Doppler and VLBI observables as output. The second part of the software was developed for the sole purpose of processing radio occultation experiments. It consists of three main modules: the frequency residuals derivation module, the geometrical optics module and the Abelian integral inversion module. The output of this second part are vertical density, temperature and pressure profiles of the target's atmosphere.

Table 2: Summary of observations.

Station time (UTC)	Telescopes Code	Solar elongation (deg)	Distance to S/C (AU)
2012-04-27 05:10 - 06:05	Ur,Sh	41	0.47
2012-04-29 05:10 - 06:05	Bd,Ke	40	0.46
2012-04-30 05:10 - 06:05	Bd	40	0.45
2012-05-01 05:10 - 06:05	Bd,Ks	39	0.44
2014-03-23 02:50 - 03:16	T6	46	0.68

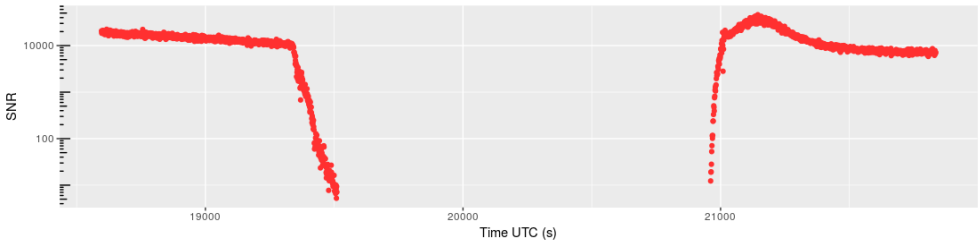

Figure 4: Example of the SNR of a signal detection during a radio occultation. This is the VEX signal detection obtained with Bd in the session of 2012.04.29. At around 19400 s the SNR starts rapidly decreasing marking the beginning of the occultation ingress, which lasts for ~3 minutes before there is Loss-Of-Signal (LOS). At around 20950 s there is Acquisition-Of-Signal (AOS) marking the beginning of the occultation egress which lasts for ~1.5 minutes. The peak of the detected SNR after egress corresponds to the closest approach of VEX to the center of mass of Venus. A higher SNR is typically observed during VEX's radio science observation phase (scheduled around the pericenter passage) because the telemetry is off during this phase. During the tone tracking part of the processing, in order to provide an appropriate polynomial fit to the low SNR part of the detection, the ingress and egress scan are split in two. For this particular example, for the ingress scan at 19400 s and for the egress scan at 21080 s.

refracted by the ionosphere, as shown in Figure 5b, and from ~19615 s, where the frequency residuals start rapidly decreasing, marks the immersion into the neutral atmosphere. The largest frequency residuals (derived as explained in Section 2.2) observed in the depth of Venus' neutral atmosphere at X-band usually reach levels of ~5 kHz before loss of signal, as shown in Figure 5a. Figure 5e shows the electron density profile derived from the frequency residuals shown in Figures 5b and 5d. In Figure 5e the ionospheric base can be identified at 100 km, along with two layers. The main layer has density $\sim 2{\times}10^{10}$ m^{-3} and altitude ~140 km and the secondary layer has density $\sim 1{\times}10^{10}$ m^{-3} and altitude ~125 km. This nightside (SZA = 142 deg) profile is consistent with other observations of the deep nightside ionosphere (*e.g.*, Kliore et al. [34], Pätzold et al. [47]).

Figure 6 shows an example of the resulting ingress profiles of Venus' neutral atmosphere from the Doppler frequency residuals corresponding to the session of 2012.04.29. Figure 6 shows the refractivity, neutral number density, temperature and pressure profiles derived with Eqs. (18), (19), (22) and (21), respectively. Despite the fact that both NNO and Bd have similar antenna dish sizes, with Bd the spacecraft signal is detected down to a lower altitude. During this observation the elevation of Bd was between 50-58 deg while for NNO it was 20-25 deg. Several noise contributions at the antenna rapidly increase, such as the atmospheric and spillover noise, at low elevation angles, which result in lower SNR detections. Besides this, the profiles corresponding to Bd and Ke were derived from the open loop Doppler data obtained with the PRIDE setup, while the profiles of NNO were derived using the frequency residuals obtained from ESA's PSA, corresponding to closed loop Doppler tracking data. The advantage of using open loop Doppler data for radio occultation resides in the ability of locking the signal digitally during the post-processing. This allows the estimation of the frequency of the carrier tone at the deeper layers of the atmosphere. This is not the case with closed-loop data, since once the system goes out of lock the signal is lost. Figure 7 shows the frequency detections obtained by the 65-m Tianma during the session of 2014.03.23, where the carrier signal of the spacecraft

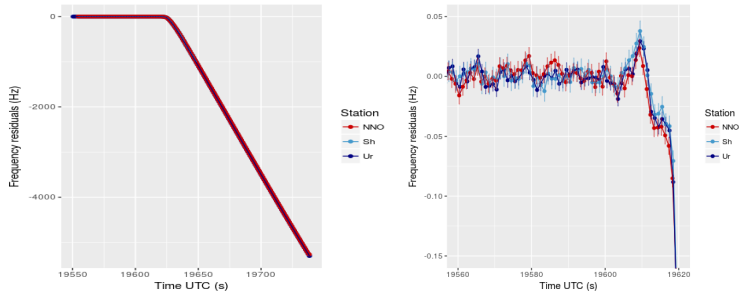

(a) (b)

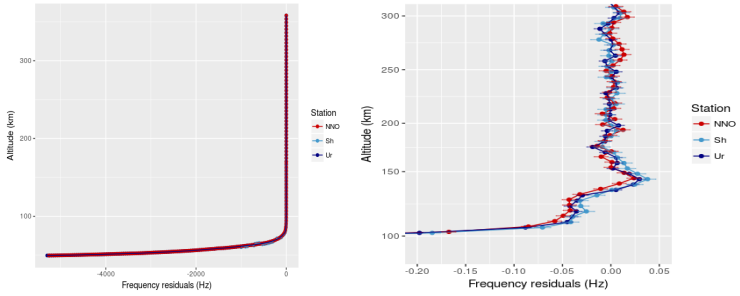

(c) (d)

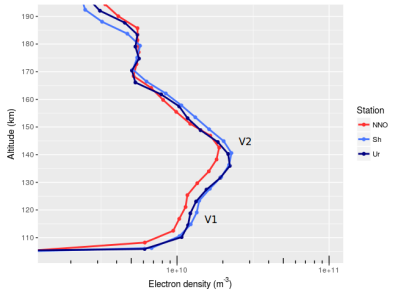

(e)

Figure 5: Frequency residuals retrieved from open-loop data from Ur and Sh compared to the residuals from closed-loop data from NNO, during occultation ingress in the session of 2012.04.27. Panel (a) shows the frequency residuals of the detected signal up to LOS. Panel (b) zooms in the frequency residuals showing when the signal starts getting refracted by Venus' ionosphere at around 19605 s. Panel (c) and (d) show the corresponding altitude probed versus the frequency residuals of the data shown in panel (a) and (b), respectively. Panel (e) shows the corresponding electron density profile, where the secondary V1 layer and main V2 layer of Venus' ionosphere are identified.

is detected throughout a complete occultation, including the time slot where the planetary disk is completely occulting the spacecraft. This is possible because of the extremely strong refraction the signal undergoes while crossing Venus' neutral atmosphere. The fact that there is no loss-of-signal (LOS) in this particular session highlights the advantage of using both large antenna dishes and open loop data processing for radio occultation experiments. On one hand, the large antenna dishes have low thermal noise allowing higher SNR detections throughout the occultation, and on the other hand, the open-loop processing allows the detection of the carrier signal through thick media. It is worth to mention, however, that for the session 2014.03.23 the closed-loop Doppler data of NNO is not currently publicly available, therefore Tianma's results could not be compared with those of NNO.

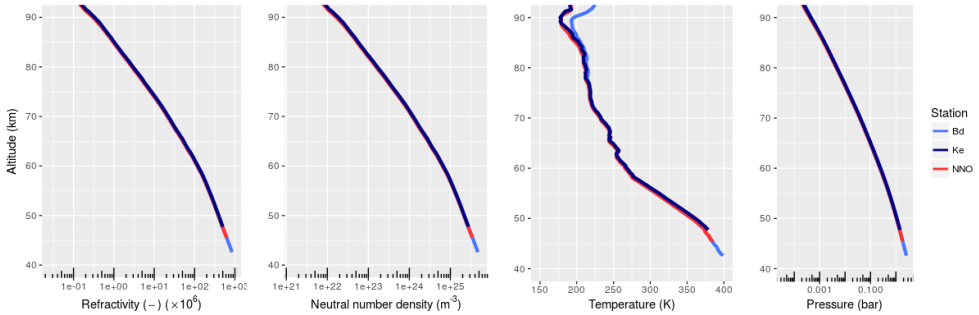

Figure 6: Refractivity, neutral number density, temperature and pressure profiles of the 2012.04.29 session. The profiles corresponding to the 32-m Bd and 12-m Ke were derived from the open loop Doppler data obtained with the PRIDE setup, and the profiles of the 35-m NNO were derived using the frequency residuals obtained from ESA's PSA, corresponding to closed loop Doppler tracking data. Despite the fact that both NNO and Bd have similar antenna dish sizes, with Bd the spacecraft signal is detected down to a lower altitude, due to the fact that the Doppler data obtained with Bd is open loop, while for NNO is closed loop.

Table 3 gives the location and depth of the radio occultation profile obtained during the different sessions. Figure 8 shows the neutral atmosphere temperature profiles obtained using Eq. (22) throughout the different sessions in 2012, displaying the ingress and egress profiles separately. Besides the assumption of a spherically symmetric atmosphere, the radio occultation method as discussed in this paper, also assumes hydrostatic equilibrium and a known composition. The composition is assumed to be constant in a spherically homogeneous well-mixed atmosphere below the altitude of the homopause (<∼125 km). For the analysis in this paper, atmospheric composition of the neutral atmosphere is assumed to be 96.5% CO_2, 3.5% N_2 [35, 52]. In order to derive the temperature profiles, an initial guess for the boundary temperature ($T(h_0)$ in Eq. 22) of 170 K at 100 km altitude was used. In the case of Venus, the boundary temperature is typically chosen to be between 170-220 K at 100 km altitude, with an uncertainty of 35 K. These values are taken from the temperature profiles of the Venus International Reference Atmosphere (VIRA) model [31, 52] and the empirical model of Venus' thermosphere (VTS3) [24].

As shown in Figure 8, the troposphere is probed down to altitudes of ∼41 km. From this altitude to about ∼58 km the temperature decreases as altitude increases. Performing a linear fit from 43 to 58 km, the mean lapse rate found for the egress

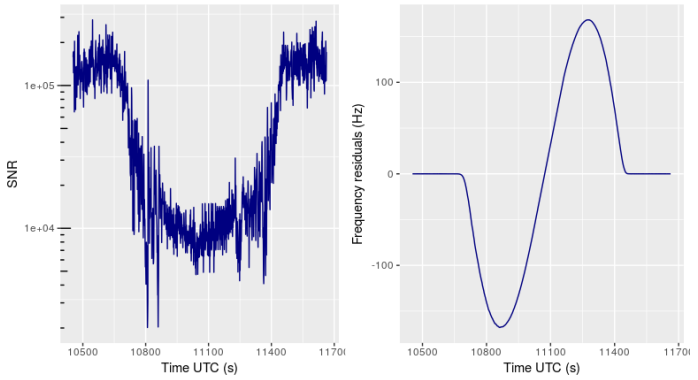

Figure 7: Detection of the carrier signal of the spacecraft throughout a complete occultation, using the open-loop Doppler data retrieved by the 65-m T6 during the session of 2014.03.23. The left panel shows the SNR throughout the detection, showing that there is no LOS during the whole occultation. The right panel shows the frequency residuals, which show from 10650 to 11100 s the ingress followed by the egress from 11100 to 11450 s. This means that T6 was able to detect the signal while the planetary disk was completely occulting VEX.

5

Table 3: Summary of location and depth of the radio occultation profiles obtained during the different sessions.

Date	Station	Mode	Minimum altitude (km)	Latitude (deg)	LST (hh:mm:ss)
2012-04-27	Ur	Ingress	46.2	-20.2	01:48:19
		Egress	43.7	83.4	23:19:29
	Sh	Ingress	45.8	-20.0	01:48:08
		Egress	44.7	83.5	23:08:12
2012-04-29	Bd	Ingress	42.7	-19.7	01:59:55
		Egress	44.0	83.6	23:17:13
	Ke	Ingress	47.8	-23.6	01:57:49
		Egress	44.3	83.6	23:12:25
2012-04-30	Bd	Ingress	41.0	-19.3	02:05:49
		Egress	42.0	83.7	23:12:39
2012-05-01	Bd	Ingress	41.9	-22.0	02:10:27
		Egress	43.1	83.7	23:35:13
	Ks	Ingress	45.1	-26.8	02:07:31
		Egress	47.2	83.8	23:13:37
2014-03-23	T6	Ingress	54.9	33.3	00:02:07
		Egress	54.9	33.3	00:02:07

profiles is 9.5 K/km. For the ingress profiles, a fit was performed from 41 to 50 km that resulted in a mean lapse rate of 6.4 K/km and another fit was made from 50 to 58 km that resulted in a mean lapse rate of 9.3 K/km. From the VIRA model, the mean lapse rate between 41-58 km from the surface is 9.8 K/km [52]. At about ∼58 km the linear trend experiences a sharp change, which is identified as the tropopause, where the upper boundary of the middle clouds is present [52, 54]. From the altitudes 60 to 80 km, where the middle atmosphere extends, there is a clear difference between the ingress and egress profiles. This is due to the difference in latitudes of the occultation profiles, which are ∼20°S and ∼83°N for the ingress and egress, respectively, for the sessions from 2012.04.27 to 2012.05.01. For the egress profiles, the region between ∼65 to ∼70 km is approximately isothermal, and from 70 km to 80 km the temperature decreases at a much lower lapse rate than at the troposphere. For the ingress profile, this isothermal behavior only extends for a couple of kilometers from ∼62 km. The difference in lapse rate between the ingress and egress profiles along the altitude range from 60 to 80 km can be attributed to dynamical variations on local scales, eddy motions or gravity waves [27]. It is desired to start the integration of the temperature profiles (Eq. 22) as high as possible. However, at high altitudes (above ∼100 km) there is not enough neutral gas detected and the noise introduced by the measurements is large with respect to the estimated refractivity values. For this reason, the upper boundary is chosen to be at an altitude of ∼100 km, where the standard deviation of the refractivity is $\sim 1/10$th of the estimated values. As shown by Eq. 22, the sensitivity of the derived temperature profiles to the upper boundary condition $T(h_0)$ rapidly decreases with altitude due to the factor $N(h_0)/N(h)$. Therefore, it was found that when using different upper boundary temperatures (170 K, 200 K and 220 K) at 100 km for the detections of a single station, the temperature profiles of that particular station converge at ∼90 km. When using the same upper boundary for all stations participating in one observation (*e.g.*, the temperature profile shown in Figure 6c for the 2012.04.29 session), the temperature profiles of the different stations converge at ∼80 km. This is due to the effect of the noise fluctuations of the refractivity profile, where the standard deviation in refractivity drops from 10% of the estimated value at 100 km to $\sim 0.1\%$ at ∼80 km.

3.3. Error propagation analysis

In order to quantify the performance of the PRIDE technique for the purpose of radio occultation experiments we carry out an error propagation analysis. To this end, we begin by propagating the frequency residual uncertainties derived from the open-loop Doppler data of the VLBI stations, through the multiple steps of data processing pipeline (Figure 3) to derive the uncertainties in the atmospheric properties of Venus measured during the radio occultation observations.

The frequency residual uncertainty $\sigma_{\Delta f}$ in time is the uncertainty of the difference between the observed frequency (also known as the sky frequency) f_{sky}, and the predicted frequency f_{pred}, the latter derived as explained in Bocanegra-Bahamón et al. [6]. The $\sigma_{\Delta f}$ is evaluated before the signal starts getting refracted by the planet's atmosphere (referred to in this paper as the frequency residuals in "vacuum" for the sake of simplicity), *i.e*, in the first part of the two-part split ingress scan, or the second part of the split egress scan. In practice, the standard deviation is calculated after performing a baseline correction to the frequency residuals in vacuum. While

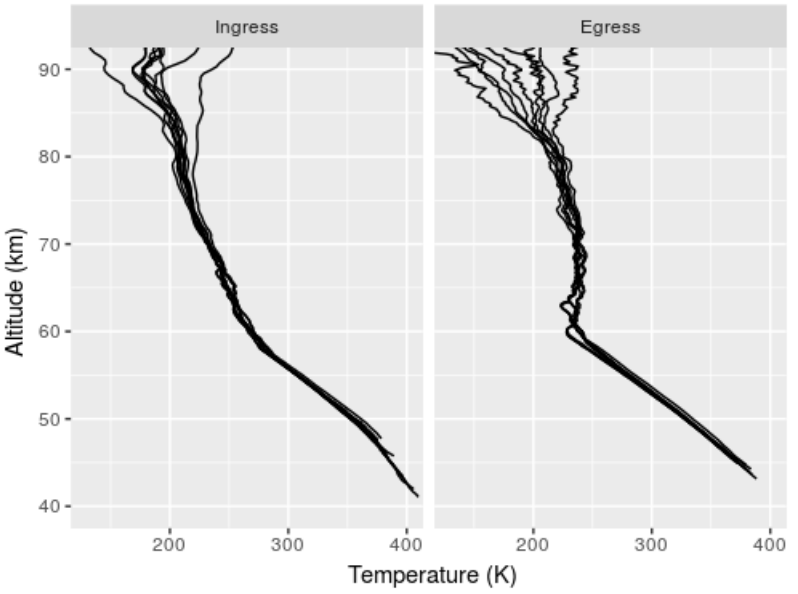

Figure 8: Compilation of the temperature profiles obtained with all participating stations during the session of 2012.04.27 to 2012.05.01. The left panel shows the ingress temperature profile corresponding to latitudes around 20 deg S. The right panel shows the egress temperature profiles corresponding to latitudes around 84 deg N.

the uncertainty of the sky frequency is random, the uncertainty of the predicted frequency is systematic, reflecting the errors of the estimated state vectors of the spacecraft and ground stations, and the errors in the ephemerides of Venus and the Earth, used to generate the Doppler predictions, and the errors in the estimation of the nominal spacecraft transmission frequency at transmission time. In the absence of these systematic errors, the frequency residuals in vacuum would be the remaining Doppler noise of the signal (due to the random uncertainties) with zero mean value, as shown in Figure 5a up to 19600 s. The presence of systematic errors in the frequency residuals in vacuum results in a non-zero mean constant trend. This effect is corrected by applying a baseline correction based in the algorithm described by Gan et al. [19]. For this reason, the $\sigma_{\Delta f}$, after baseline correction, is assumed to be solely due to $\sigma_{f_{sky}}$.

The uncertainty of the f_{sky} derived with the procedure shown in Bocanegra-Bahamón et al. [6] depends on the integration time used, the noise introduced by the instrumentation on the ground stations and onboard the spacecraft, and the noise introduced by the propagation of the signal, σ_{prop}, through the interplanetary medium, and, the Earth's ionosphere and troposphere. In the case of one-way Doppler the instrumental noise is given by the thermal noise, σ_{th}, introduced by the receiver at the ground stations and the limited power received at downlink, the noise introduced by the spacecraft USO, σ_{USO}, the noise introduced by frequency standard used at the ground stations, σ_{FS}, and the antenna mechanical noise, σ_{mech}. The modeled $\sigma_{\Delta f}$ is calculated by,

$$\sigma_{\Delta f}^2 = (\sigma_{th}^2 + \sigma_{USO}^2 + \sigma_{FS}^2 + \sigma_{mech}^2 + \sigma_{prop}^2) f^2 \quad (23)$$

where f is the carrier tone frequency which is ~8.4 GHz at X-band. The Allan deviation related to the thermal noise of the ground station receivers is given by Barnes et al. [4], Rutman & Walls [51] as,

$$\sigma_{th}(\tau) \approx \sqrt{3BS_\phi}/2\pi f_0 \tau \quad (24)$$

where S_ϕ is the one-sided phase noise spectral density of the received signal in a 1 Hz bandwidth, B is the carrier loop bandwidth which is 20 Hz for this experiment, f_0 is the nominal frequency of the Doppler link and τ is the integration time, which in this case has the value of 1 s. The relative noise power of the carrier tone is given by S_ϕ, which is approximated by $1/(\mathrm{SNR})$ where SNR is the signal-to-noise ratio of the signal evaluated in a 1 Hz bandwidth. The thermal noise values estimated with Eq. (24) of the X-band Doppler detections for the different radio telescopes used during the study at hand are summarized in Table 4. The uncertainties found correspond to values ranging from 1.6 mHz for the lowest thermal noise, found at the 65-m T6, to 10.4 mHz for the highest thermal noise, found at the 34-m Ks (higher than the one found for the 12-m Ke). As reported by Häusler et al. [22], the USO that provided the reference frequency for the VEX transponder has an Allan deviation of $\sim 3 \times 10^{-13}$ at integration times 1-100 s, which corresponds to $\sigma_{USO} f < 2.5$ mHz at 1 s integration time. Based on these values the modeled $\sigma_{\Delta f}$ for each station is calculated using Eq. (23) and displayed in Table 4, along with the measured $\sigma_{\Delta f}$ of the signal detections at 1 s integration time (derived by taking the mean standard deviation of the frequency residuals in vacuum). All VLBI stations are equipped with a hydrogen maser frequency standard that provide a stability of $< 1 \times 10^{-13}$ at $\tau = 1$ s, corresponding to a $\sigma_{FS} f < 0.9$ mHz. From the instrumental noises, the antenna mechanical noise has not been taken into account due to the lack of information for these structures in the time intervals relevant for the study at hand.

Regarding the noise due to propagation effects, the noise induced by the Earth's ionosphere is calibrated using the total vertical electron content (vTEC) maps [25] and the noise introduced by the Earth's troposphere is calibrated using the Vienna Mapping Functions VMF1 [7]. These two corrections are applied to the Doppler predictions before deriving the frequency residuals Δf. The noise introduced by the remaining errors after calibration with the vTEC and VMF1 maps are not quantified in the work at hand. Furthermore, the interplanetary plasma noise was not characterized in this study due to the fact that only X-band detections were obtained. However, an estimate of the Allan deviation of the interplanetary phase scintillation noise can be derived using the approach described in Molera-Calvés et al. [46]. Based on the analysis of multiple tracking campaigns of the VEX signal, in S- and X-band, at different solar elongations, a relation (Eq. 6 in Molera-Calvés et al. [46]) was formulated to estimate the expected phase variation of the received signal as a function of TEC,

$$\sigma_{\mathrm{expected}} = \frac{\mathrm{TEC}}{4000} \cdot \left(\frac{8.4\mathrm{GHz}}{f_{\mathrm{obs}}}\right) \cdot \left(\frac{\tau_{\mathrm{nod}}}{300s}\right)^{\frac{m+1}{2}} [\mathrm{rad}], \quad (25)$$

where TEC is Venus-to-Earth total electron content along the line-of-sight, τ_{nod} is the nodding cycle of the observations, f_{obs} is the observing frequency and m is the

spectral index. Since the phase power spectrum S_ϕ is of the form $S_\phi = Af^{-m}$, where m is the spectral index and A is a constant, the scintillation contribution in the spectral power density can be characterized using a first order approximation on the logarithmic scale, as explained in Molera-Calvés et al. [46] (Eq. 5). Using this approximation the expected phase variation can be expressed as follows,

$$\sigma_{\text{expected}} = \left[\frac{Af_c^{-m} \cdot f_c}{m+1}\right]^{\frac{m+1}{2}} \tag{26}$$

where f_c is the cut-off frequency of the spectral power density of the phase fluctuations (usually ~0.2 mHz). Following Armstrong et al. [3], for $2 < m < 4$ the Allan variance of a phase spectrum of the form $S_\phi = Af^{-m}$ is [3],

$$\sigma_y^2(\tau) = \frac{A\tau^m}{\pi^2 f_0^2 \tau^3} \int_0^\infty \frac{\sin^4(\pi z)}{z^m} dz \tag{27}$$

5

Based on the results presented in Molera-Calvés et al. [46], it is assumed a Venus-to-Earth TEC along the line-of-sight of 10^2 tecu at 40 deg elongation (Fig. 6 of Molera-Calvés et al. [46]) and a spectral index of 2.4, which is the average spectral index of more than hundred observing sessions. Using these values and Eqs. 25 to 27 the estimated Allan deviation is of 2.2×10^{-13} at $\tau = 1$ s, which corresponds to $\sigma_{prop} f = 1.8$ mHz.

Figure 9 shows the percentages of the Allan variances of each modeled noise source with respect to the total measured frequency residuals variance for each station. The dark blue portion of the bar represents the difference between the measured and the modeled variances. In the case of T6 the predominant noise comes from the USO. For Bd, both the thermal noise and the USO noise represent each ~30% of the total frequency residuals measured. This indicates that for one-way radio occultation experiments the noise introduced by the USO is larger than the noise introduced by the thermal noise of the ground stations, when using antennas with a diameter larger than ~30 m. This limiting noise source could be avoided by performing two-way tracking during occultations, however this would limit the occultation detections only to ingress passes since the transmitting signal would be out of lock during egress. The thermal noise of Sh is estimated to be higher than the thermal noise of Ur, which coincides with the larger frequency residuals obtained with Sh, despite the fact that both stations have the same antenna diameter. The thermal noise of Ke corresponds to ~70% of the noise budget. This is reasonable when compared to the thermal noise of the other stations, given the fact the Ke has a 12-m diameter. On the other hand, the modeled thermal noise for Ks corresponds to almost 80% of its noise budget, which is extremely high for a 34-m antenna. This was corroborated with the system temperature readings for the session of 2012.05.01 (also the only session where Ks participated), which were much higher than its reported nominal system temperature [11]. For this reason the data retrieved with Ks should be discarded. The modeled noise attributed to interplanetary plasma phase scintillation, estimated for elongation angles of ~40 degrees, can be corrected for when multi-frequency observations are available [5, 57]. For T6 this would correspond to a calibration of ~20% of the Doppler noise. The noise introduced by the ground

stations frequency standard in the overall noise budget is marginal compared to the other sources of noise.

As shown in Table 4 the modeled noise for the different telescopes is consistently lower than the measured noise. This can be attributed to unmodeled noise (*e.g.*, antenna mechanical noise) and errors in the estimates of the propagation noise and the noise introduced by the USO. The estimate of the propagation noise given in Table 4 includes only the plasma scintillation noise, but not the remaining errors after calibration of the Earth's ionospheric and tropospheric propagation effects. As for the USO, the Allan deviation given in Table 4 represents the nominal frequency stability of the USO, hence, not the actual measurements during the observations.

Regarding the choice of integration time to process the radio occultation scans, there is a trade-off to be made between vertical resolution and frequency residual noise. The choice of a small integration time results in a better vertical resolution, but also results in larger frequency residuals noise. Furthermore, the vertical resolution of the profiles derived using geometrical optics are diffraction limited to the Fresnel zone diameter [26], which is $\approx 2\sqrt{\lambda D}$, where λ is the signal wavelength, $D = R\cos(\beta_e - \gamma - \beta_r)$, and R, β_e, γ and β_r are defined as shown in Figure 2. To be consistent with this inherited vertical resolution limit of the model the sample spacing should be kept as close to $\sqrt{\lambda D}$ as possible, which for this experiment should be larger than ~470 m. When processing the signal detections, it was noticed that the minimum integration time for which this condition would be satisfied was 0.1 s down to ~50 km from the surface, since from this altitude on the bending angle of the ray path largely increases. Hence, the integration time was chosen to be 0.1 s down to an altitude of 50 km and then from this point down to lowest altitudes probed an integration time of 1.0 s was used.

Table 4: Noise budget of X-band Doppler detections of the VLBI stations during the radio occultation sessions.

Station	Thermal noise		USO		Frequency standard		Plasma phase scintillation		Modeled $\sigma_{\Delta f}$	Measured $\sigma_{\Delta f}$
	σ_{th}	σ_{thf} (mHz)	σ_{USO}	σ_{USOf} (mHz)	σ_{FS}	σ_{FSf} (mHz)	σ_{prop}	σ_{propf} (mHz)	(mHz)	(mHz)
T6	1.9×10^{-13}	1.6	3.0×10^{-13}	2.5	1.0×10^{-13}	0.9	2.2×10^{-13}	1.8	3.6	3.7
Bd	2.9×10^{-13}	2.4	3.0×10^{-13}	2.5	1.0×10^{-13}	0.9	2.2×10^{-13}	1.8	4.0	4.4
Ur	3.6×10^{-13}	3.0	3.0×10^{-13}	2.5	1.0×10^{-13}	0.9	2.2×10^{-13}	1.8	4.4	5.0
Sh	5.9×10^{-13}	4.9	3.0×10^{-13}	2.5	1.0×10^{-13}	0.9	2.2×10^{-13}	1.8	5.9	6.9
Ke	8.6×10^{-13}	7.2	3.0×10^{-13}	2.5	1.0×10^{-13}	0.9	2.2×10^{-13}	1.8	7.9	8.8
Ks	1.2×10^{-12}	10.4	3.0×10^{-13}	2.5	1.0×10^{-13}	0.9	2.2×10^{-13}	1.8	10.9	11.8

Once the frequency residual uncertainties have been calculated we proceed to propagate them through the processing pipeline. We assume that the sampled f_{sky} are independent and uncorrelated, hence the frequency covariance matrix $C_f = \langle \Delta f \Delta f^T \rangle$ is diagonal. In order to derive the uncertainties of the ray path parameters, the equations that describe the occultation geometry (Eqs. 10 and 11) are linearized with respect to the ray path angles δ_r and β_r as described by Fjeldbo et al. [17], and using the standard propagation of errors [10], the covariance matrix between the bending angle α and the impact parameter a, $C_{\alpha a}$, can be derived as follows,

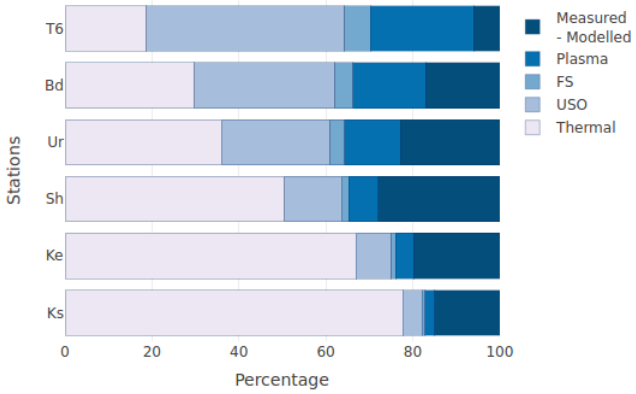

Figure 9: Percentage of the modeled noise sources in the total measured frequency residuals. In the case of T6 the predominant noise comes from the USO. For Bd, both the thermal noise and the USO noise represent each 30% of the total frequency residuals measured. Although Ur and Sh have the same antenna size the thermal noise of Sh is higher than that of Ur. The modeled thermal noise of Ke corresponds to almost 70% of the budget, which in comparison to other stations is reasonable since its antenna diameter is only 12 m and the station has an uncooled receiver. On the other hand, in the case of the 34-m Ks, the thermal noise corresponds to 80% of the budget which given its size indicates an under-performance of the station during the observations it was involved in. In the overall budget, the noise introduced by the frequency standard is considered to be marginal with respect to the other sources of noise.

$$C_{\alpha a} = M_{\alpha f} C_f M_{af}^T \tag{28}$$

where,

$$M_{\alpha f} = \begin{bmatrix} \frac{\partial \alpha_1}{\partial f_1} & \frac{\partial \alpha_1}{\partial f_2} & \cdots & \frac{\partial \alpha_1}{\partial f_n} \\ \frac{\partial \alpha_2}{\partial f_1} & \frac{\partial \alpha_2}{\partial f_2} & \cdots & \frac{\partial \alpha_2}{\partial f_n} \\ \vdots & \vdots & \ddots & \vdots \\ \frac{\partial \alpha_n}{\partial f_1} & \frac{\partial \alpha_n}{\partial f_2} & \cdots & \frac{\partial \alpha_n}{\partial f_n} \end{bmatrix}_{f=\bar{f}}$$

and,

$$M_{af} = \begin{bmatrix} \frac{\partial a_1}{\partial f_1} & \frac{\partial a_1}{\partial f_2} & \cdots & \frac{\partial a_1}{\partial f_n} \\ \frac{\partial a_2}{\partial f_1} & \frac{\partial a_2}{\partial f_2} & \cdots & \frac{\partial a_2}{\partial f_n} \\ \vdots & \vdots & \ddots & \vdots \\ \frac{\partial a_n}{\partial f_1} & \frac{\partial a_n}{\partial f_2} & \cdots & \frac{\partial a_n}{\partial f_n} \end{bmatrix}_{f=\bar{f}}$$

where n is the number of sampled sky frequencies.

The uncertainties associated with the refractive index μ are determined as explained in [43], using the covariance matrix $C_{\alpha a}$. First, Eq. (14) is solved using the trapezoidal approximation and the embedded exponential function is linearized about zero. Then the result is linearized with respect to α and a yielding,

$$\Delta\mu_i = \sum_{k=i}^{K} (M_{\mu\alpha,k}\Delta\alpha + M_{\mu a,k}\Delta a) \tag{29}$$

for the i-th concentric spherical layer, where $M_{\mu\alpha,k} = h_{k-1} - h_k$ and $M_{\mu a,k} = (\partial h_k/\partial a_k)(a_{k+1} - \alpha_k) + (\partial h_{k-1}/\partial a_k)(\alpha_k - \alpha_{k-1})$ are the linear transformations (to the first order) relating μ and α, and, μ and a, respectively, where $h = \ln((a_{k+1} + a_k)/2a_i)$.

The covariance matrix of μ, C_μ, is given by,

$$\begin{aligned} C_\mu &= \langle \Delta\mu_k \Delta\mu_j \rangle \\ &= \sum_{i=1}^{K} [V_{\alpha_i} M_{\mu\alpha,ji} M_{\mu\alpha,ki} + V_a M_{\mu a,ji} M_{\mu a,ki} \\ &\quad + C_{\alpha a,i}(M_{\mu\alpha,ki} M_{\mu a,ji} + M_{\mu\alpha,ji} M_{\mu a,ki})] \end{aligned} \tag{30}$$

where V_α and V_a are the variances of α and a, respectively.

From Eq. (22) two types of uncertainty can be identified for the temperature profile. The first term from the right side of Eq. (22) results in a systematic error due to the uncertainty of the boundary temperature. The uncertainty resulting from the second term is due to the statistical fluctuation of the refractivity. Using the linearized transformations of Eq. (22) and Eq. (21), the covariance matrices for temperature C_T and pressure C_P are derived using Eq. (30) as described by Lipa & Tyler [43] (Appendix C),

$$\begin{aligned} C_T &= \langle \Delta T_k \Delta T_j \rangle \\ &= \sum_{r=k}^{B} \sum_{s=j}^{B} b_r b_s \left(\frac{N_r N_s}{N_k N_j}\right)\left(\frac{C_{\mu,rs}}{N_r N_s} - \frac{C_{\mu,ks}}{N_k N_s} - \frac{C_{\mu,rj}}{N_r N_j} + \frac{C_{\mu,kj}}{N_k N_j}\right) \end{aligned} \tag{31}$$

$$C_P = \langle \Delta P_k \Delta P_j \rangle = k N_B \sum_{r=k}^{B} \sum_{s=j}^{B} b_r b_s C_{\mu,rs} \tag{32}$$

where $b = g(h_{i+1} - h_i)/k$, g is the gravitational acceleration of the central body, which is assumed to be constant, k is Boltzmann's constant and B corresponds to the layer centered at h_0 given by the upper boundary condition in Eq. (22).

Figure 10 shows the resulting uncertainties in the refractivity, neutral number density, temperature and pressure profiles, from the error propagation of the Doppler frequency residuals for the stations Bd and Ke during the session of 2012.04.29. These uncertainties correspond to the profiles shown in Figure 6. The minimum values for σ_μ, σ_{nn} and σ_P are found at an altitude of ~78 km, which corresponds to the altitude where the temperature profiles of the different stations converge in Figure 10 (where the temperature difference between stations drops below 1 K). The refractivity and neutral number density uncertainties increase approximately linearly from 78 km to 67 km. From this altitude to about 63 km sharp changes are observed

at the same altitudes for both stations, which correspond to the altitudes where there are also large changes in the lapse rate as shown in the temperature profile of Figure 6. At ~58 km, where the tropopause is expected, the refractivity and neutral number density uncertainties start increase at a larger rate as the altitudes decreases to 50 km in the case of Bd, and 55 km in the case of Ke. The rate at which the uncertainties increase is higher for Ke than for Bd. The sudden drop at 50 km and 55 km, for Bd and Ke, respectively, are related to the change of integration time from 0.1 s to 1.0 s during the processing. The temperature uncertainties are 15 K and 23 K, for Bd and Ke, respectively, at 90 km and rapidly drop below 1 K at an altitude of ~85 km. The observed temperature uncertainties above 85 km explain the differences observed around ~90 km in the profiles of Bd and Ke, as shown in Figure 6c. Above 85 km the main contribution to the resulting temperature uncertainty is given by the systematic error induced by the choice of the boundary temperature at 100 km. As the refractivity increases, this value gets highly damped below the 85 km.

It is important to take into account that Figure 10 is comparing the residuals obtained with a 32-m antenna with those of a 12-m antenna. Badary at an integration time of 0.1 s has a frequency residual uncertainty of $\sigma_{\Delta f} = 18.4$ mHz and Katherine of $\sigma_{\Delta f} = 36.8$ mHz. The largest uncertainties in the neutral number density found were $\sigma_{nn} = 3.1 \times 10^{20}$ m^{-3} at 51.2 km for Bd and $\sigma_{nn} = 3.5 \times 10^{20}$ m^{-3} at 55.7 km for Ke. While the ratio of the frequency uncertainties between these two stations is 2, the ratio of the largest neutral number density uncertainties is 1.1. Tellmann et al. [55] reported neutral density uncertainties $\sigma_{nn} = 3.0 \times 10^{20}$ m^{-3} at 50 km with NNO.

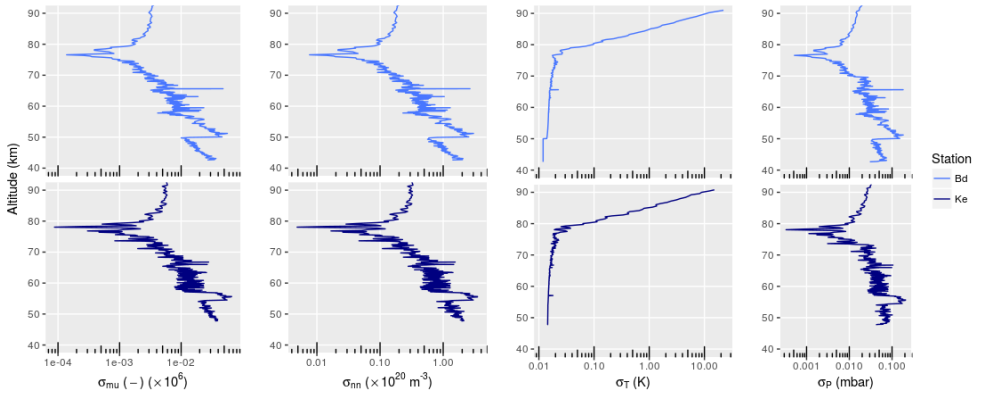

Figure 10: Uncertainties in the refractivity, neutral number density, temperature and pressure profiles, from the error propagation of the Doppler frequency residuals for the stations Bd and Ke during the session of 2012.04.29. These uncertainties correspond to the profiles shown in Figure 6. The sudden drop at 50 km and 55 km, for Bd and Ke, respectively, are related to the change of integration time from 0.1 s to 1.0 s during the processing.

4. Conclusions

With the VEX test case exposed in this work and the corresponding error analysis, we have demonstrated that the PRIDE setup and processing pipeline is suited for radio occultation experiments of planetary bodies. The noise budget indicated that the

uncertainties in the derived neutral density and temperature profiles remain within the range of uncertainties reported in previous Venus radio occultation experiments (*e.g.*, Tellmann et al. [55]). Summing up the results of all the observations with the different telescopes, we found that at 1 bar level the frequency residuals vary between 4800-5000 Hz with uncertainties of 3.7-11.8 mHz, which result in uncertainties in the neutral number densities of 2.7-3.9$\times 10^{20}$ m^{-3} and in temperature of $\sim$0.01 K. When characterizing the different sources of Doppler noise, it was found that for one-way radio occultation experiments the noise introduced by the USO can dominate over the thermal noise of large dish antennas (>35m). In the case of the observations with the 65 m Tianma, this corresponds to 45 % of the noise budget. This could be mitigated by performing two-way radio occultation experiment or by using a USO with higher frequency stability such as the Deep Space Atomic Clock (DSAC) [56].

Radio occultation experiments carried out with PRIDE can exploit the advantage of having access to large radio telescopes from the global VLBI networks, such as the 65-m Tianma, 100-m Effelsberg or the 305-m Arecibo. Additionally, due to the wide coverage of the networks, the setup can be optimized to ensure high SNR signal detections. For instance, by choosing as receiving stations VLBI telescopes that can track the spacecraft at the highest antenna elevations, when the deep space station has limitations in terms of antenna elevation.

As demonstrated with the detection of Bd, open-loop Doppler data as the one produced with PRIDE allows sounding deeper layers of planetary bodies with thick atmospheres when compared to closed-loop Doppler data. The main advantage of open loop data for radio occultation experiments is that during the post-processing the frequency of the carrier signal can be estimated with precision wideband spectral analysis. Even if there are large unexpected changes in the carrier frequency due to, for instance, large refractivity gradients in the deep atmosphere or interference effects such as multipath propagation. This is not the case with closed-loop detections, since in this scheme the signal is received at much narrower bandwidth. Using a feedback loop, the detection bandwidth is gradually shifted around a central frequency, that is the predicted Doppler signal for the experiment. In case of large unexpected changes in frequency, the signal will no longer be detected by the tracking station because of a loss-of-lock in the closed-loop scheme. With the wideband spectral analysis of PRIDE, we showed that even with small antennas, such as the 12-m Ke, the signal can be detected below Venus' clouds layer.

5. Acknowledgements

We thank the referee for her/his constructive comments and corrections of our manuscript, which resulted in an overall improvement of the paper. The European VLBI Network is a joint facility of independent European, African, Asian, and North American radio astronomy institutes. Scientific results from data presented in this publication are derived from the following EVN project codes: v0427, v0429, v0430, v0501 and v0323. This study made use of data collected through the AuScope initiative. AuScope Ltd is funded under the National Collaborative Research Infrastructure Strategy (NCRIS), an Australian Commonwealth Government Programme. Venus Express (VEX) was a mission of the European Space Agency. The VEX a priori orbit, Estrack and DSN tracking stations transmission frequencies, and the events' schedules were supplied by the

ESA's Venus Express project. The authors would like to thank the personnel of all the participating radio observatories. In particular, the authors are grateful to Eiji Kawai and Shingo Hasagawa for their support of observations at the Kashima radio telescope. The authors are grateful to the Venus Express Radio Science team, the VeRa PI Bernd Häusler and Venus Express Project Scientists Dmitri Titov and Håkan Svedhem for their efforts, advice and cooperation in conducting the study presented here. Tatiana Bocanegra-Bahamón acknowledges the NWO–ShAO agreement on collaboration in VLBI (No. 614.011.501). Giuseppe Cimò acknowledges the EC FP7 project ESPaCE (grant agreement 263466). Lang Cui thanks for the grants support by the program of the Light in China's Western Region (No. YBXM-2014-02), the National Natural Science Foundation of China (No. 11503072, 11573057,11703070) and the Youth Innovation Promotion Association of the Chinese Academy of Sciences (CAS).

References

[1] Ahmad, B. & Tyler, G. L. 1998, Radio Science, 33, 129

[2] Ando, H., Imamura, T., Sugimoto, N., et al. 2017, Journal of Geophysical Research: Planets

[3] Armstrong, J., Woo, R., & Estabrook, F. 1979, The Astrophysical Journal, 230, 570

[4] Barnes, J. A., Chi, A. R., Cutler, L. S., et al. 1971, Instrumentation and Measurement, IEEE transactions on, 1001, 105

[5] Bertotti, B., Comoretto, G., & Iess, L. 1993, Astronomy and Astrophysics, 269, 608

[6] Bocanegra-Bahamón, T., Molera-Calvés, G., Gurvits, L., et al. 2018, Astronomy & Astrophysics, 609, A59

[7] Boehm, J., Werl, B., & Schuh, H. 2006, J. Geophys. Res., 111, B02406, doi:10.1029/2005JB003629

[8] Born, M. & Wolf, E. 1999, Principles of Optics: Electromagnetic Theory of Propagation, Interference and Diffaction of Light, 7th edn. (Cambridge University Press)

[9] Brace, L. & Kliore, A. 1991, Space Science Reviews, 55, 81

[10] Brandt, S. 1997, Statistical and computational methods in data analysis. (Springer Verlag, New York)

[11] Campbell, Robert. 2018, `http://www.evlbi.org/user_guide/EVNstatus.txt`, EVN status table II. Accessed on March 7 2018

[12] Dirkx, D., Gurvits, L., Lainey, V., et al. 2017, Planetary and Space Science, 147, 14

[13] Duev, D. A., Calvés, G. M., Pogrebenko, S. V., et al. 2012, Astronomy & Astrophysics, 541, A43

[14] Duev, D. A., Pogrebenko, S. V., Cimò, G., et al. 2016, Astronomy & Astrophysics, 593, A34

[15] Eshleman, V. R. 1973, Planetary And Space Science, 21, 1521

[16] Fjeldbo, G. & Eshleman, V. R. 1968, Planetary and Space Science, 16, 1035

[17] Fjeldbo, G., Kliore, A. J., & Eshleman, V. R. 1971, The Astronomical Journal, 76, 123

[18] Fox, J. L. & Kliore, A. J. 1997, Venus II, 161

[19] Gan, F., Ruan, G., & Mo, J. 2006, Chemometrics and Intelligent Laboratory Systems, 82, 59

[20] Girazian, Z., Withers, P., Häusler, B., et al. 2015, Planetary and Space Science, 117, 146

[21] Gubenko, V. N., Andreev, V. E., & Pavelyev, A. G. 2008, Journal of Geophysical Research: Planets, 113

[22] Häusler, B., Pätzold, M., Tyler, G., et al. 2007, ESA SP, 1295, 1

[23] Häusler, B., Pätzold, M., Tyler, G., et al. 2006, Planetary and Space Science, 54, 1315

[24] Hedin, A., Niemann, H., Kasprzak, W., & Seiff, A. 1983, Journal of Geophysical Research: Space Physics, 88, 73

[25] Hernández-Pajares, M., Juan, J., Sanz, J., et al. 2009, Journal of Geodesy, 83, 263

[26] Hinson, D., Simpson, R., Twicken, J., Tyler, G., & Flasar, F. 1999, Journal of Geophysical Research: Planets, 104, 26997

[27] Hinson, D. P. & Jenkins, J. M. 1995, Icarus, 114, 310

[28] Howard, H., Tyler, G., Fjeldbo, G., et al. 1974, Science, 183, 1297

[29] Imamura, T., Ando, H., Tellmann, S., et al. 2017, Earth, Planets and Space, 69, 137

[30] Jenkins, J. M., Steffes, P. G., Hinson, D. P., Twicken, J. D., & Tyler, G. L. 1994, Icarus, 110, 79

[31] Keating, G., Bertaux, J. L., Bougher, S. W., et al. 1985, Advances in Space Research, 5, 117

[32] Keimpema, A., Kettenis, M., Pogrebenko, S., et al. 2015, Experimental Astronomy, 39, 259

[33] Kliore, A., Levy, G. S., Cain, D. L., Fjeldbo, G., & Rasool, S. 1967, Science, 158, 1683

[34] Kliore, A., Patel, I., Nagy, A., Cravens, T., & Gombosi, T. 1979, Science, 205, 99

[35] Kliore, A. J. 1985, Advances in Space Research, 5, 41

[36] Kliore, A. J. & Luhmann, J. G. 1991, Journal of Geophysical Research: Space Physics, 96, 21281

[37] Kliore, A. J. & Patel, I. R. 1980, Journal of Geophysical Research: Space Physics, 85, 7957

[38] Kliore, A. J. & Patel, I. R. 1982, Icarus, 52, 320

[39] Kolosov, M., Yakovlev, O., Efimov, A., Pavelyev, A., & Matyugov, S. 1979, Radio Science, 14, 163

[40] Kopeikin, S. M. & Schäfer, G. 1999, Physical Review D, 60, 124002

[41] Kursinski, E., Hajj, G., Schofield, J., Linfield, R., & Hardy, K. R. 1997, Journal of Geophysical Research: Atmospheres (1984–2012), 102, 23429

[42] Limaye, S. S., Lebonnois, S., Mahieux, A., et al. 2017, Icarus, 294, 124

[43] Lipa, B. & Tyler, G. L. 1979, Icarus, 39, 192

[44] Mariner, S. G. 1967, Science (New York, NY), 158, 1678

[45] Molera-Calvés, G., Kallio, E., Cimo, G., et al. 2017, Space Weather, 15, 1523

[46] Molera-Calvés, G., Pogrebenko, S., Cimò, G., et al. 2014, Astronomy & Astrophysics, 564, A4

[47] Pätzold, M., Häusler, B., Bird, M., et al. 2007, Nature, 450, 657

[48] Pätzold, M., Neubauer, F., Carone, L., et al. 2004, in Mars Express: The Scientific Payload, Vol. 1240, 141–163

[49] Peter, K., Pätzold, M., Molina-Cuberos, G., et al. 2014, Icarus, 233, 66

[50] Phinney, R. & Anderson, D. 1968, Journal of Geophysical Research, 73, 1819

[51] Rutman, J. & Walls, F. 1991, Proceedings of the IEEE, 79, 952

[52] Seiff, A., Schofield, J., Kliore, A., et al. 1985, Advances in Space Research, 5, 3

[53] Steffes, P. G., Jenkins, J. M., Austin, R. S., et al. 1994, Icarus, 110, 71

[54] Tellmann, S., Häusler, B., Hinson, D., et al. 2012, Icarus, 221, 471

[55] Tellmann, S., Pätzold, M., Häusler, B., Bird, M. K., & Tyler, G. L. 2009, Journal of Geophysical Research: Planets, 114

[56] Tjoelker, R. L., Prestage, J. D., Burt, E. A., et al. 2016, IEEE transactions on ultrasonics, ferroelectrics, and frequency control, 63, 1034

[57] Tortora, P., Iess, L., Bordi, J., Ekelund, J., & Roth, D. 2004, Journal of guidance, control, and dynamics, 27, 251

[58] Vasilyev, M., Vyshlov, A., Kolosov, M., et al. 1980, Acta Astronautica, 7, 335

[59] Withers, P. 2010, Advances in Space Research, 46, 58

[60] Withers, P., Moore, L., Cahoy, K., & Beerer, I. 2014, Planetary and Space Science, 101, 77

[61] Yakovlev, O., Matyugov, S., & Gubenko, V. 1991, Icarus, 94, 493

[62] Yakovlev, O. I. 2002, Space radio science (CRC Press)

CHAPTER 6

Conclusions

Since the efforts carried out to track the descent of Huygens in Titan's atmosphere with VLBI radio telescopes [26], the technique we know today as PRIDE has been tested, improved, validated and consolidated. By providing estimates of the spacecraft state vectors as a function of time, utilizing phase-referenced near-field VLBI and radial Doppler measurements, PRIDE can be used for many radio science applications within the framework of planetary missions.

One of the main purposes of the work carried out for this dissertation was to benchmark the performance of PRIDE against that of the deep space complexes for radio science applications, and to identify if there were advantages of conducting radio science experiments with PRIDE. To this end, simultaneous tracking experiments of ESA's MEX with PRIDE and three DSN and Estrack stations were conducted as described in Chapter 4, addressing research question 1.

In terms of the precision of Doppler components of the PRIDE technique, with the MEX Phobos fly-by experiment it was demonstrated that the residual frequencies in "free-space" obtained from the open-loop Doppler observables are at the same noise levels as those obtained with the closed-loop Doppler data from the deep space stations (in Section 4.3 and shown in Chapter 4 Figure 2). The median of the Doppler residuals for all the detections with the VLBI stations was found to be ~ 2 mHz, which translates into a linear measure for the three-way Doppler of $\sim 35 \mu$m/s at X-band.

The spectral analysis realized on the spacecraft carrier tone with PRIDE has proven to provide very high spectral resolution ($\sim$2 mHz at 10 s integration time) as shown in Chapter 4 (particularly in Section 4.3). Section 3.4 shows step by step how this spectral data processing methodology (refer to as narrowband processing in this work) is carried out with PRIDE. It is important to stress that the quality of the results of the narrowband part of the processing are essential in the overall PRIDE processing pipeline, affecting the precision of both angular position and radial velocity products.

Regarding the precision of the angular position observables, the precision of the

spectral analysis: 1) affects the near-field model used for broadband correlation, and 2) sets the precision of the 2π-ambiguous phase delays extracted from carrier tone. The latter are used as input for the astrometric equation to derive the corrections to the apriori angular position of the spacecraft (Section 3.6.2), and the accumulated Doppler corrections during the tone filtering in the narrowband processing are the resulting Doppler observables (Section 3.4).

As discussed in Section 3.5, there are several considerations that need to be taken into account in order to perform broadband correlation of spacecraft signals with SFXC, due to the distance of the spacecraft to the telescopes and the characteristics of the spectrum of spacecraft signal. As explained in Section 3.2.6, it is necessary to use a near-field VLBI model in order to correctly correlate the received spacecraft signal on the multiple telescopes. When left uncorrected, the Doppler shift in the spacecraft signal will smear the cross-correlation spectrum because of the difference in the Doppler phase of each of the topocentric detections (Section 3.4.5). Therefore, from the narrowband processing the derived Doppler phase corrections are used as input for the near-field VLBI model. Because of the different signal transmission modes the spacecraft has during its orbit around a planet, the received signal spectrum changes in time. During the 'radio science' mode typically only the carrier signal is present, while in the longer 'tracking' mode it is common to find ranging tones in the spectrum around the carrier signal. The data where the ranging tones are present are used for broadband correlation at high spectral resolution, in order to precisely estimate the group delay. In its current state, SFXC has the implementation of the spectrum filtration and compression in order to perform the broadband correlation, as described in [6], integrated into its standard spectral averaging algorithms.

Regarding the precision of the phase delays, the optimal fit of phase delays with respect to the group delays (Section 3.5) is found by minimizing the squared error over time periods when both phase and group delays are available. The fit yields the number of phase cycles thus providing the solution of unambiguous phase data, also for the time intervals for which there is no group delay data available. In its current state, the PRIDE software was able to produce sub-nanoradian precision ($\sim$0.2 nrad, $\sim 40\mu$as) for lateral position measurements using MEX observations [6]. This result corresponds to a precision of $\sim$40 m in lateral position at a distance of 1.4 AU.

With respect to the Doppler observables obtained with PRIDE, there are various characteristics in the spectral analysis, setup of the observations and noise model analysis, that can be advantageous when conducting a radio science experiments with PRIDE, compared to typical single-dish closed-loop operations of the deep space tracking networks (research question 1).

From the perspective of the narrowband processing methodology, since PRIDE observations observe two type of sources - the spacecraft signal and the background natural radio source - the experiment requires for the signals to be initially recorded in as wide bandwidth (8, 16, or 32 MHz bandwidth per sub-band) as possible, in order to be able to detect the background calibrator source (Section 4.2.1). For this reason, it is possible to ensure the detection of the spacecraft signal in the presence of abrupt changes in frequency, amplitude and SNR (which is often the case when the spacecraft signal interacts with planetary atmospheres). During the narrowband processing, the extraction and filtering down of the signal - performed to provide a direct estimation of the frequency and amplitude of the carrier tone at a very high

spectral resolution (Section 4.2.1) -, only happens as a post-processing step on the signal recordings (*e.g.*, open-loop Doppler detection).

As discussed in Section 4.1, the deep space networks of NASA and ESA have open-loop receivers, the Radio Science Receivers (RSR), where such wideband spectral analysis methods are used to retrieve the Doppler data during radio science experiments. The RSR and VLBI receivers (used in PRIDE) have, in terms of technology, the same capabilities [15]. However, the RSR are not the main receivers of these deep space networks, but instead are the closed-loop receivers. These receivers make use of a feedback loop in their circuitry, needed to be able to provide real time acquisition of the spacecraft data, essential for navigation and telemetry, but they cannot cope with highly dynamic signals because they can easily make the system go out of lock. For this reason, for tracking operations closed-loop receivers are used, and for radio science operations the use of open-loop receivers is preferred, but cannot always be guaranteed since it depends on which operational mode has higher priority. One such example, was the MEX Phobos fly-by experiment (`GR035`) treated in Chapter 4, where DSN's DSS-63 (Robledo, Spain) recorded closed-loop Doppler data for purposes of orbit determination since the main science objective was to track the Phobos fly-by. However, this event happened just a few minutes before the MEX signal got occulted by Mars, which would have been preferably recorded by the RSR. On this occasion, we concurrently observed the Phobos fly-by and subsequent Mars occultation with 12 VLBI radio telescopes. These stations provided open-loop Doppler data from which Mars' atmospheric profiles were derived [2]. Because Mars' neutral atmosphere is very tenuous, there are no large differences in terms of the lowest depths probed when comparing the two types of Doppler data. This is however, not the case with highly dense atmospheres such as those of Venus, the giant planets and Titan.

Another advantage of PRIDE experiments is the coverage that the VLBI networks can provide. As discussed in Chapter 2, PRIDE observations can be conducted by ~40 radio telescopes distributed around the world to carry out radio science experiments. This is of particular importance for experiments that require long tracking sessions, since the variability of the antennas' elevation angle has a non-negligible impact on the SNR ratio of the observations. This was demonstrated, as discussed in Chapter 4, during the `GR035` experiment where MEX was tracked for 25 hours with a total of 31 VLBI stations, as shown in Figure 1. During these observations, there were periods of time where antennas with smaller collecting areas reached similar SNR levels as larger antenna dishes because the elevation of the small antennas was more favorable (see Chapter 4 Figure 3). For instance, the thermal noise of the detections obtained with the 25-m Urumuqi (Ur) antenna and the 15-m Hartebeesthoek (Ht) antenna were $\sigma_{th} = 1.2 \times 10^{-14}$ and $\sigma_{th} = 1.0 \times 10^{-14}$, respectively, for $\tau = 10\,\mathrm{s}$. Even though Ht is much smaller than Ur, the better elevation conditions that Ht had during the observation resulted in detections yielding similar thermal noise. At elevations <20 degrees, noise contributions due to larger tropospheric path delays and larger spillover noise have a larger impact on the total system temperature compared to those of the receiver temperature. Having access to stations like the 65-m Tianma, 64-m Sardinia, 100-m Effelsberg, 100-m Green Bank and the 305-m Arecibo, the setup of radio science experiments with PRIDE can be optimized to minimize the instrumental noise, using the best configuration in terms of antenna elevation and

collecting area.

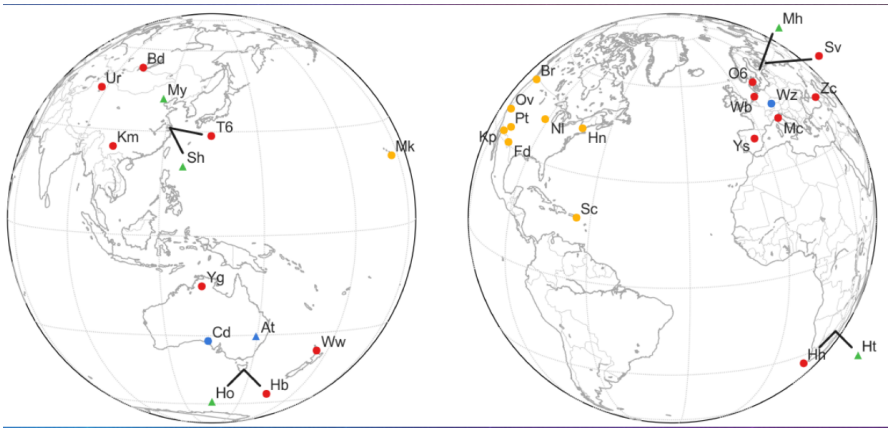

(a) Distribution of radio telescopes involved in GR035 around the world.

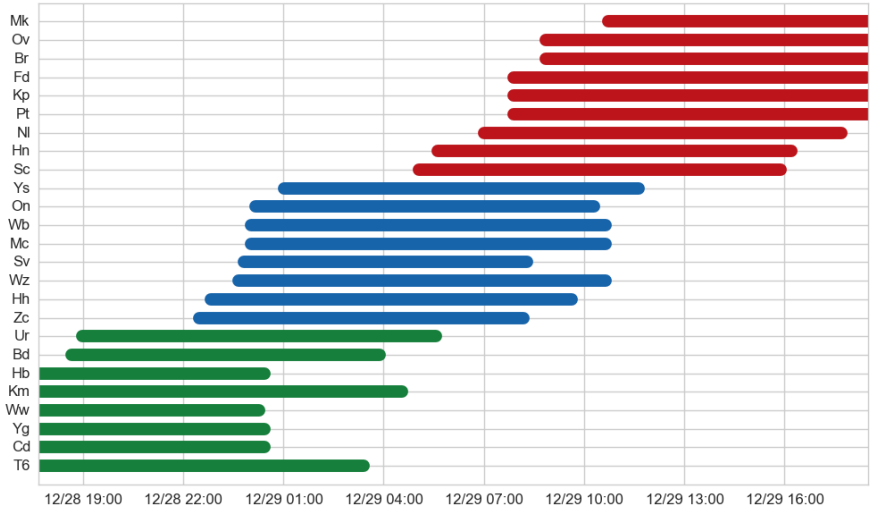

(b) Operational time ranges of the radio telescopes during GR035.

Figure 1: MEX Phobos-flyby experiment (GR035) PRIDE coverage. Credit: [6]. This figures shows the large coverage obtained during this experiment, where 31 antennas across the world from New Zealand to the US participated in the observations.

In its current state, as demonstrated, the PRIDE processing pipeline is able to provide precise VLBI observables and a separate source of precise open-loop Doppler observables. By having access to multiple telescopes around the world, PRIDE can offer a non-negligible operational and coverage addition for radio science activities to the six DSN and Estrack stations. In particular, when the requests to support multiple deep space missions have conflicting schedules for the nominal agencies' tracking assets. For instance, one possibility is providing one-way tracking for a probe with a sufficiently stable USO (Allan deviation of $\sim 10^{-13}$ at τ =1-100 s), without having

to schedule DSN or Estrack stations, for tests or radio science experiments, as it has been conducted in the past using PRIDE to track ESA's VEX.

In order to consolidate its position as a radio science instrument within the scientific community, the PRIDE team has investigated multiple applications of the technique for planetary science applications. Molera-Calvés et al. [13, 14] studied the interplanetary plasma scintillations and coronal mass ejection compiling several years of observations of VEX and MEX radio signal, and Dirkx et al. [3] performed a covariance analysis to determine the influence of PRIDE observables to the determination of the ephemerides of the Jovian system and the associated physical parameters, in the framework of the upcoming ESA's JUICE mission. In the work at hand, the capabilities of PRIDE for radio occultation studies (Chapter 5) have been demonstrated, utilizing VEX tracking data as a test case.

For this purpose, a data processing methodology was developed for radio occultation signal processing, using the Abelian integral inversion, as described in Section 5.2.1, addressing research question 2. In this case, the phase modulation that the signal experiences as it propagates through Venus' atmosphere was analyzed. In order to evaluate the performance of PRIDE for this type of experiment (research question 3), it was necessary to perform an error propagation analysis, to verify the quality of the PRIDE data and validate the processing pipeline. For this purpose, the noise in the frequency estimates was propagated to determine the uncertainties of the atmospheric profiles derived from the PRIDE data (Section 5.3.3). The noise of the frequency residuals was expected to be higher than those obtained with the `GR035` experiment (Chapter 4), since the received signal during occultation has a much lower SNR ratio than when the signal is not being refracted by the planet's atmosphere. For instance, while for `GR035` the average Doppler noise of detections with Sheshan was 1.1 mHz at 10 s integration time (no propagation through Mars' atmosphere) for the occultation experiments at 1 bar level in Venus (~50 km altitude) the Doppler noise found was 6.9 mHz at 1.0 s, which scales to 2.2 mHz at 10 s integration time. However, it was demonstrated that the SWSpec/SCtracker/dPLL software package described in Chapter 3, is able to perform precise wideband spectral analysis with such low SNR ratio signals, since the estimated uncertainties of the derived neutral density and temperature profiles are at the same level of those reported in previous Venus radio occultation experiments (*e.g.*, Tellmann et al. [23]). For instance, at 1 bar level (~50 km altitude) the uncertainties of the frequency residuals found ranged from 3.7 to 11.8 mHz at 1 s integration time, for the telescopes involved in the observations. This resulted in uncertainties in the neutral number densities of 2.7-3.9$\times 10^{20}$ m^{-3} and in temperature of ~ 0.01 K at 1 bar. These results correspond to the uncertainties derived by the Venus Radio science experiment (VeRa) team from radio occultation sessions using Doppler data from Estrack's NNO [23].

In the overall noise budget of the VEX radio occultation experiments with PRIDE, it was observed that the USO noise dominated over the thermal noise for antenna dishes larger than >35 m. For instance, for the 65 m Tianma station 45% of the noise budget corresponded to the USO noise. Therefore, in order to reduce the overall noise for one-way radio occultation observations, besides having antennas with larger collecting areas, it is important to have a USO onboard with higher frequency stability ($\sim 3\times 10^{-13}$ at τ =1-100 s for the case of VEX's USO), such as the Deep Space Atomic Clock (DSAC) [24], or to conduct the experiment in two-way mode at the cost of losing

the egress data due to the signal lock-up time.

Furthermore, when comparing the results obtained during the same occultation sessions with the closed-loop Doppler data obtained from Estrack's NNO (research question 4), it was shown that the open-loop detections of a VLBI station with similar antenna diameter (32-m Badary) led to sounding deeper layers of Venus' troposphere. It was shown, that even with small antennas, such as the 12-m Katherine, the signal can be detected below Venus' clouds layer, and that for one session the 65-m Tianma was able to detect a complete occultation without loss-of-signal as the spacecraft was occulted by the planet. These are all examples of the advantages of processing open-loop Doppler data for radio science applications. In order to exploit the advantage of having access to the largest radio telescopes on Earth and be able to sound down to critical refraction altitudes, the setup of the experiment has to be optimized taking into account the antenna elevations, the predicted SNR detections and the nominal frequency stability of the USO (in the case of one-way mode detections).

Summarizing, the work shown in this thesis proves that the spectral analysis used in PRIDE allows the derivation of Doppler observables with very high spectral resolution, and provides precise Doppler phase corrections to be used as input for the broadband processing of the spacecraft signal. This step allows the correct correlation of the spacecraft signals, enabling the precise derivation of angular position corrections to the a priori spacecraft orbit. By demonstrating the performance of PRIDE and providing a noise budget to its Doppler detections, it is shown that the PRIDE technique qualifies as a fully operational radio science instrument. In particular, with the VEX radio occultation test case, it was demonstrated that the PRIDE methodology is suitable for experiments that require a careful detection of highly dynamic signals, such as radio occultation observations of planetary bodies with thick atmospheres.

1. Recommendations and outlook

PRIDE has been selected by ESA as one of the eleven experiments of the ESA's L-class JUpiter ICy moons Explorer mission (JUICE) mission, planned for launch in 2022. PRIDE will be involved in two key mission goals, the improvement of the Jovian system ephemerides [3, 4], which requires the precise determination of the lateral position of the spacecraft on the celestial sphere, and the investigation of the Jovian atmosphere and the ionosphere of the Jovian moons via radio occultation observations. Additionally, PRIDE is involved in the ESA EnVision M5 design study [25] for an orbiter mission to Venus. The involvement of PRIDE would be primarily related to radio occultation investigations. This section treats a few items that need to be addressed for future radio science experiments with JUICE and eventually with EnVision.

1.1. Calibrator sources in the ecliptic plane survey

As discussed in Duev et al. [5, 6], in order to minimize the uncertainties of the spacecraft orbital parameters derived from PRIDE observables, it is essential to conduct the observations using phase calibrator sources whose absolute position errors does not exceed 0.2 mas and their angular separation to the spacecraft does not exceed 2 deg [1]. However, the existing list of phase calibrators [17] shows that the den-

sity of these sources along the ecliptic plane is not sufficient for high accuracy VLBI spacecraft tracking. Therefore, in order to achieve sub-nanoradian accuracy in the lateral position of the spacecraft, it is necessary to establish a dense grid of calibrator sources around Jupiter's orbit that fulfill those characteristics.

To this end, an ecliptic plane VLBI survey should be conducted, using the candidate selection techniques that have been successfully implemented in large astrometric surveys [18–20]. From several previous tracking campaigns, including MEX and VEX observations, the PRIDE team has demonstrated that a relative position accuracy of 0.1 mas between a 50 mJy background source and the spacecraft can be achieved. Therefore, ideally the candidate sources for the survey should be within 2 deg of Jupiter's orbital plane (to correctly apply the phase-referencing technique), have flux densities >50 mJy at X-band and Ka-band (the closer the calibrator source is to the target the lower the flux density limit for the calibrator), and have absolute position errors $\lesssim$0.2 mas.

1.2. Improvements to the radio occultation software

In its current state, the radio occultation software described in Chapter 5 is capable of processing frequency data, from raw open-loop Doppler data of radio telescopes that use VLBI data acquisition systems, to produce refractivity, density, temperature and density profiles. Additionally, the software should be extended to be able to reduce the amplitude information of the received signal. By analyzing the decrease in amplitude of the carrier signal as it passes behind the limb of the planetary body, atmospheric absorptivity profiles can be derived. The amplitude of the recorded signal is however not only affected by the absorbing constituents in the atmosphere, but also by the spacecraft antenna mispointing and by refractive defocussing. Therefore, the attenuation due to these effects has to be modeled and removed to retrieve the excess attenuation, from which the abundance of the constituents responsible for the absorptivity profiles can be derived.

All radio occultation experiments of Venus to this day, such as Fjeldbo et al. [7], Jenkins et al. [9], Tellmann et al. [22], have assumed the planet's atmosphere can be modeled as a spherically symmetric medium, made of concentric shells, each of them with a constant refractive index. This means that the atmospheric properties are assumed to be the same at a certain altitude irrespective of the latitude or local time. In the case of Venus, it has been proven that this assumption does not hold in the cloud region and at the terminator [12]. This is also the case for the other Solar System bodies with thick atmospheres: the giants planets and Titan. In order to understand what the effect is of using incorrect assumptions when modeling these bodies' atmospheres, it is proposed to implement an axis-symmetric model of the atmosphere [21], where the atmosphere is assumed to be barotropic and is modeled with concentric cylinders centered upon the rotational axis of the planet. This approach takes into account latitudinal changes, assuming the angular speeds due to zonal winds and rotation are constant on each cylinder. In this way, the radio occultation software will provide the option to choose between the spherical symmetric and axis-symmetric atmospheric model, when processing radio occultation signals.

Multi-path interference of the radio signal is a phenomenon often seen in the propagation of radio signal through thick media. In the case of Venus, multi-path effects have been observed in latitudes above 75° at the altitude were the tropopause

is found, as reported by Pätzold et al. [16]. When multipath is detected multiple solutions for a bending angle as a function of impact parameter are found for a single measurement of the instantaneous frequency of the spacecraft signal. Although, when reducing frequency data a wideband spectral analysis can be used to identify the existence of multi-path, it is often difficult to discern the source of the interference. However, there are multiple techniques using the complex radio signal, using both phase and amplitude measurements, that have been proven successful for this purpose. It is proposed to investigate novel radio holographic techniques -making use of the received complex radio signal-, that have been largely used in radio occultation experiments related to the Earth's lower atmosphere to address the multipath interference while providing sub-Fresnel vertical resolution. In terms of resolution and ability to handle multi-path effects, it has been reported that the Fourier operator-based [11], canonical transform [8] and the Full Spectrum Inversion (FSI)[10] methods are the most efficient.

1.3. Preparations for PRIDE-JUICE radio occultation experiments

In radio occultation theory, the inverse problem is known as the procedure where from Doppler frequency residuals the ray path parameters (bending angle and impact parameter) are derived to subsequently retrieve atmospheric refractivity profiles. This is the algorithm that is currently implemented in PRIDE's radio occultation software. However, in order to evaluate the optimum experimental setup for future radio occultation experiments of PRIDE-JUICE, the opposite problem has to be solved. In order to determine the expected frequency shifts and attenuation of the received signal during a specific occultation geometry the so-called forward ray tracing should be implemented. In this scenario, the refractive index of the medium is assumed to be given and the resulting refraction of the rays is calculated step-by-step, parameterizing each modeled layer with a set of ray path parameters.

To address this problem ray tracing simulations have to be implemented. The implementation of the simulations can be broken down in two tasks, one handling the planet's atmospheric model and one the ray tracing calculations. Regarding the atmospheric model, it is known that Jupiter's atmosphere is composed primarily of atomic and molecular hydrogen and helium, and in the homopause level, of several minor gases such as hydrocarbons, NH_3 and PH_3. The neutral lower and upper atmospheres as well as the ionosphere have been observed with several techniques, and as expected, there are no measurements with a full profile covering both the neutral and plasma regions. In order to solve the forward problem, a grid with the available information from previous missions has to be created with gas parameters against height and latitude, which can subsequently be converted into refractive indices per grid point. Regarding the ray tracing calculations - simulating the propagation of the radio signal step-by-step through the atmospheric gases -, they are similar to the calculations used for the inverse problem (Chapter 5), which are already implemented in PRIDE's radio occultation software. In principle, the order of the calculations has to be inverted as explained by Yakovlev [27]. Furthermore, once the simulations for the forward problem are implemented, an error propagation analysis can be carried out to determine the precision required of the signal's frequency and amplitude estimates, in order to reduce the uncertainties of the atmospheric model used as

input.

References

[1] Beasley, A. & Conway, J. 1995, in Very Long Baseline Interferometry and the VLBA, Vol. 82, 327

[2] Bocanegra-Bahamon, T., Molera-Calvès, G., Gurvits, L., et al. In preparation, Mars Express radio occultation observed by PRIDE

[3] Dirkx, D., Gurvits, L., Lainey, V., et al. 2017, Planetary and Space Science, 147, 14

[4] Dirkx, D., Lainey, V., Gurvits, L., & Visser, P. 2016, Planetary and Space Science, 134, 82

[5] Duev, D. A., Calvés, G. M., Pogrebenko, S. V., et al. 2012, Astronomy & Astrophysics, 541, A43

[6] Duev, D. A., Pogrebenko, S. V., Cimò, G., et al. 2016, Astronomy & Astrophysics, 593, A34

[7] Fjeldbo, G., Kliore, A. J., & Eshleman, V. R. 1971, The Astronomical Journal, 76, 123

[8] Gorbunov, M. 2002, Radio Science, 37

[9] Jenkins, J. M., Steffes, P. G., Hinson, D. P., Twicken, J. D., & Tyler, G. L. 1994, Icarus, 110, 79

[10] Jensen, A. S., Lohmann, M. S., Benzon, H.-H., & Nielsen, A. S. 2003, Radio Science, 38

[11] Jensen, A. S., Lohmann, M. S., Nielsen, A. S., & Benzon, H.-H. 2004, Radio science, 39

[12] Limaye, S. S., Lebonnois, S., Mahieux, A., et al. 2017, Icarus, 294, 124

[13] Molera-Calvés, G., Kallio, E., Cimo, G., et al. 2017, Space Weather, 15, 1523

[14] Molera-Calvés, G., Pogrebenko, S., Cimò, G., et al. 2014, Astronomy & Astrophysics, 564, A4

[15] Mudgway, D. J. & Launius, R. 2001, Uplink-Downlink: A History of the Deep Space Network, 1957-1997

[16] Pätzold, M., Häusler, B., Bird, M., et al. 2007, Nature, 450, 657

[17] Petrov, L. 2018, RFC source position catalogue: rfc2018b. Consulted on June 2018

[18] Petrov, L., Kovalev, Y., Fomalont, E., & Gordon, D. 2011, The Astronomical Journal, 142, 35

[19] Petrov, L., Kovalev, Y. Y., Fomalont, E., & Gordon, D. 2008, The Astronomical Journal, 136, 580

[20] Petrov, L., Phillips, C., Bertarini, A., Murphy, T., & Sadler, E. M. 2011, Monthly Notices of the Royal Astronomical Society, 414, 2528

[21] Schinder, P., Flasar, F., Marouf, E., et al. 2015, Radio Science, 50, 712

[22] Tellmann, S., Häusler, B., Hinson, D., et al. 2012, Icarus, 221, 471

[23] Tellmann, S., Pätzold, M., Häusler, B., Bird, M. K., & Tyler, G. L. 2009, Journal of Geophysical Research: Planets, 114

[24] Tjoelker, R. L., Prestage, J. D., Burt, E. A., et al. 2016, IEEE transactions on ultrasonics, ferroelectrics, and frequency control, 63, 1034

[25] Widemann, T., Wilson, C., Ghail, R., et al. 2018, in 42nd COSPAR Scientific Assembly, Vol. 42

[26] Witasse, O., Lebreton, J.-P., Bird, M. K., et al. 2006, Journal of Geophysical Research (Planets), 111, 7

[27] Yakovlev, O. I. 2002, Space radio science (CRC Press)

Acronyms

∆DOR Delta Differential One-way Ranging. 11, 20

AIPS Astronomical Image Processing System. 47–49, 51, 58, 60

AOS Acquisition-Of-Signal. 105

BCRF Barycentric Celestial Reference Frame. 41

BCRS Barycentric Celestial Reference System. 40–42

DAS Data Acquisition System. 34

DFT Direct Fourier Transform. 56

DOR Differential One-way Ranging. 11

DPLL Digital Phase-Locked-Loop. 57

DSAC Deep Space Atomic Clock. 118

DSN Deep Space Network. 11, 21

DWE Doppler Wind Experiment. 2

ECMWF European Centre for Medium-Range Weather Forecasts. 45

ESA European Space Agency. 2

Estrack ESA Tracking Network. xiii, xix

EVN European VLBI Network. 21, 23, 31, 33, 38

FFT Fast Fourier Transform. 38

FWHM Full Width Half Maximum. 13

GCRS Geocentric Celestial Reference System. 41

GGOS Global Geodetic Observing System. 45

GNSS Global Navigation Satellite System. 44

ICME Interplanetary Coronal Mass Ejection. 94

ICRF International Celestial Reference Frame. 30, 40, 60

IERS International Earth Rotation Service. 40

IF Intermediate Frequency. 33, 34, 36, 47

IGS International GNSS Service. 44

IPS Interplanetary Scintillation. 43

ITRS International Terrestrial Reference System. 40

JIVE Joint Institute for VLBI ERIC. 21, 34, 38, 54

JPL Jet Propulsion Laboratory. 31

JUICE JUpiter ICy moons Explorer. 3, 5

LNA Low Noise Amplifier. 13, 34

LO Local Oscillator. 36

LOS Loss-Of-Signal. 105

MER-B Mars Exploration Rover B. 25

MEX Mars Express. 2–4, 124

MRO Metsähovi Radio Observatory. 54

NAIF Navigation and Ancillary Information Facility. 31, 33

NASA National Aeronautics and Space Administration. 11, 31

NMW Numerical Weather Models. 45

NRAO National Radio Astronomy Observatory. 47

PCFS Personal Computer Field System. 34

PPN Parametrized Post-Newtonian. 1, 41

PRIDE Planetary Radio Interferometry and Doppler Experiment. 1, 2, 25, 29, 31, 35, 38, 39, 41, 45, 54

PSA Planetary Science Archive. 103

RF Radio Frequency. 33, 34

RFI Radio Frequency Interference. 47, 56

SEFD System Equivalent Flux Density. 48

SFXC Software FX Correlator. 38, 39, 41, 47, 58

SNR Signal-to-Noise Ratio. xiv, xx, 20, 48, 56

SSB Solar System Barycenter. 40–42, 58

sTEC slant Total Electrical Content. 44

SWSpec Software Spectrometer. 54

TCB Barycentric Coordinate Time. 40

TCG Geocentric Coordinate Time. 41

TDB Barycentric Dynamical Time. 40, 42, 43, 58

TDT Terrestrial Dynamical Time. 33

TT Terrestrial Time. 43

USO Ultra-Stable Oscillator. 1, 10

UTC Coordinated Universal Time. 40, 57

VDIF VLBI Data Interchange Format. 54

VeRa Venus Radio science experiment. 128

VEX VLBI experiment. 31

VEX Venus Express. 2, 3

VLA Very Large Array. 31

VLBA Very Long Baseline Array. 21, 23, 31

VLBI Very Long Baseline Interferometry. 2, 3, 11–13, 15, 18–21, 29, 31, 34, 36, 38–41, 43, 46, 49, 53, 57

VMF1 Vienna Mapping Functions. 45

vTEC vertical Total Electrical Content. 44

WLMS Weighted Least Mean Square. 56

WOLA Window-OverLapped Add. 54, 56

Curriculum Vitæ

Tatiana Bocanegra Bahamón was born in Bogotá, Colombia, on May 17, 1985. She attended secondary school at Aspaen Gimnasio Iragua in Bogotá, Colombia, graduating in 2002. In 2003, she started studying physics and mathematics at Universidad de Los Andes, in Bogotá, Colombia, and then in 2005 transferred to the faculty of Aerospace Engineering at Delft University of Technology, in Delft, the Netherlands. In 2008 was awarded best bachelor graduation project at the TU Delft Aerospace Design Synthesis Symposium, with the thesis entitled 'Space-based interferometer at 22 GHz'. In 2009, she continued her master's studies at the faculty of Aerospace Engineering with major in Astrodynamics and Space Missions. In 2010, she did an intership for 6 months at the Joint Institute for VLBI ERIC (JIVE) in Dwingeloo, the Netherlands, within the Space Science and Innovative Applications Group, and in 2011 graduated with the thesis entitled 'Radio tracking experiments with the Phobos-Grunt spacecraft for gravity field determination of Phobos'.

In 2011, she joined the same group at JIVE as a researcher in training, in collaboration with the Shanghai Astronomical Observatory (ShAO), in Shanghai, China, appointed to perform supporting activities including scheduling and analysis of VLBI spacecraft tracking experiments with radio telescopes around the world, and testing and developing features for the Doppler data processing pipeline. As a Ph.D. candidate at Delft University of Technology, within the Planetary Exploration group at the faculty of Aerospace Engineering, she investigated the scientific applications of these tracking activities. She developed a data processing and analysis methodology to perform radio occultation experiments of planetary missions (*e.g.*, ESA's Mars Express and Venus Express) in order to derive density and temperature profiles of the planet's neutral atmosphere and ionosphere. This work, funded by the Nederlandse Organisatie voor Wetenschappelijk Onderzoek (NWO) and ShAO, under the Dutch-Chinese cooperation in VLBI, led to the content of this dissertation.

List of Publications

Journal Articles

- **T. M. Bocanegra-Bahamón**, G. Molera Calvés, L.I. Gurvits, G. Cimò, D. Dirkx, D.A. Duev, S.V. Pogrebenko, P. Rosenblatt, S. Limaye, L. Cui, P. Li, T. Kondo, M. Sekido, A.G. Mikhailov, M.A. Kharinov, A.V. Ipatov, W. Wang, W. Zheng, M. Ma, J.E.J. Lovell, J.N. McCallum. *Venus Express radio occultation observed with PRIDE*. Accepted to Astronomy & Astrophysics, 2019.
- **T.M. Bocanegra-Bahamón**, G. Molera Calvès, L.I. Gurvits, D.A. Duev, S.V. Pogre-benko, G. Cimò, D. Dirkx and P. Rosenblatt. *Planetary Radio Interferometry and Doppler Experiment (PRIDE) technique: A test case of the Mars Express Phobos fly-by. 2.Doppler tracking: Formulation of observed and computed values, and noise budget*. Astronomy & Astrophysics, Volume 609, p. A59, 2018.
- **T.M. Bocanegra-Bahamón**, C. Bracken, M. Costa Sitjà, D. Dirkx, I. Gerth, K. Konstantinidis, C. Labrianidis, M. Laneuville, A. Luntzer, J.L MacArthur, A. Maier, A. Morschhauser, T.A. Nordheim, R. Sallantin and R. Tlustos. *MUSE – Mission to the Uranian system: Unveiling the evolution and formation of ice giants.* Advances in Space Research, Volume 55, Issue 9, pp. 2190–2216, 2015.
- G. Molera Calvés, E. Kallio, G. Cimò, J. Quick, D.A. Duev, **T.M. Bocanegra-Bahamón**, M. Nickola, M.A. Kharinov and A.G. Mikhailov. *Analysis of an interplanetary coronal mass ejection by a spacecraft radio signal: A case study*. Space Weather, Volume 15, p. 1523, 2017.
- D. Dirkx, L.I. Gurvits, V. Lainey, G. Lari, A. Milani, G. Cimò, **T.M. Bocanegra-Bahamón**, P.N.A.M. Visser. *On the contribution of JUICE-PRIDE to Jovian system ephemerides*. Planetary Space Science, Volume 147, p. 14, 2017.
- D.A. Duev, S.V. Pogrebenko, G. Cimò, G. Molera Calvés, **T.M. Bocanegra-Bahamón**, L.I. Gurvits, M.M. Kettenis, J. Kania, V. Tudose, P. Rosenblatt. *Planetary Radio Interferometry and Doppler Experiment (PRIDE) technique: A test*

case of the Mars Express Phobos fly-by. Astronomy & Astrophysics, Volume 593, p. A34, 2016.

- D.A. Duev, M.K. Zakhvatkin, V.A. Stepanyants, G. Molera Calvés, S.V. Pogrebenko, L.I. Gurvits, G. Cimò, **T.M. Bocanegra-Bahamón**. *RadioAstron as a target and as an instrument: Enhancing the Space VLBI mission's scientific output*. Astronomy & Astrophysics, Volume 573, p. A99, 2015.
- G. Molera Calvés, S.V. Pogrebenko, G. Cimò, D.A. Duev, **T.M. Bocanegra-Bahamón**, J.F. Wagner, J. Kallunki, P. De Vicente, G. Kronschnabl, R. Haas, and others. *Observations and analysis of phase scintillation of spacecraft signal on the interplanetary plasma*. Astronomy & Astrophysics, Volume 564, p. A4, 2014.
- C.S. Arridge, N. Achilleos, J. Agarwal, C.B. Agnor, R. Ambrosi, N. André, S.V. Badman, K. Baines, D. Banfield, M. Barthélémy, M.M. Bisi, J. Blum, **T.M. Bocanegra-Bahamón**, B. Bonfond, C. Bracken, P. Brandt, C. Briand, C. Briois, S. Brooks, J. Castillo-Rogez, T. Cavalié, B. Christophe, A.J. Coates, G. Collinson, J.F. Cooper, M. Costa Sitjà, R. Courtin, I.A. Dagli, I. de Pater and others. *The science case for an orbital mission to Uranus: Exploring the origins and evolution of ice giant planets*. Planetary Space Science, Volume 104, Part A, pp. 122-140, 2014.
- D.A. Duev, G. Molera Calvés, S.V. Pogrebenko, L.I. Gurvits, G. Cimò, Giuseppe and **T.M. Bocanegra-Bahamón**. *Spacecraft VLBI and Doppler tracking: Algorithms and implementation*. Astronomy & Astrophysics, Volume 541, p. A43, 2012.

Popular Science Articles

- **T. M. Bocanegra-Bahamón**, G. Cimò, L.I. Gurvits. *Ruimteonsezoeksmissies onder een (radio-astronomisch) vergrootglas*. Ruimtevaart 1, 2013.